

Variable tree rooting strategies are key to model distribution, productivity and evapotranspiration of tropical evergreen forests

Boris Sakschewski¹, Werner von Bloh¹, Markus Drüke^{1,2}, Anna A. Sörensson² Sörensson^{3,-34}, Romina Ruseica² Ruscica^{3,-34}, Fanny Langerwisch⁴ Langerwisch^{5,-56}, Maik Billing¹, Sarah Bereswill⁶ Bereswill⁷, Marina Hirota⁷ Hirota^{8,-89}, Rafael S. Oliveira⁸ Oliveira⁹, Jens Heinke¹, Kirsten Thonicke¹

¹Potsdam Institute for Climate Impact Research, Potsdam, 14473, Germany

²Humboldt Universität zu Berlin, Unter den Linden 6, 10099 Berlin, Germany

³Universidad³ Universidad de Buenos Aires - Consejo Nacional de Investigaciones Científicas y Técnicas, Centro de Investigaciones del Mar y la Atmósfera (CIMA/UBA-CONICET), Buenos Aires, Argentina.

⁴Institut⁴ Institut Franco-Argentin d'Etudes sur le Climat et ses Impacts, Unité Mixte Internationale (UMI-IFAECI/CNRS-CONICET-UBA), Argentina

⁵Czech⁵ Czech University of Life Sciences Prague, Department of Water Resources and Environmental Modeling, 165 00 Praha 6 – Suchbát, Czech Republic

⁶Palacký⁶ Palacký University Olomouc, Department of Ecology and Environmental Sciences, 78371 Olomouc, Czech Republic

⁷University⁷ University of Potsdam, Potsdam, 14469, Germany

⁸Federal⁸ Federal University of Santa Catarina (UFSC), Campus Universitário Reitor João David Ferreira Lima Trindade – Florianópolis – SC, CEP: 88040-900, Santa Catarina, Brazil

⁹University⁹ University of Campinas (UNICAMP) Cidade Universitária "Zeferino Vaz" CEP 13083-970, Campinas-SP, Sao Paulo, Brazil

Correspondence to: Boris Sakschewski (boris.sakschewski@pik-potsdam.de)

Abstract. A variety of modelling studies have suggested tree rooting depth as a key variable to explain evapotranspiration rates, productivity and the geographical distribution of evergreen forests in tropical South America. However, none of those studies acknowledged resource investment, timing and physical constraints of tree rooting depth within a competitive environment, undermining the ecological realism of their results. Here, we present an approach of implementing variable rooting strategies and dynamic root growth into the LPJmL4.0 DGVM and apply it to tropical and sub-tropical South-America under contemporary climate conditions. We show how competing rooting strategies which underlie the trade-off between above- and below-ground carbon investment lead to more realistically simulation of intra-annual productivity and evapotranspiration, and consequently simulated forest cover and spatial biomass distribution. We find that climate and soil depth determine a spatially heterogeneous pattern of mean rooting depth and belowground biomass across the study region. Our findings support the hypothesis that the ability of evergreen trees to adjust their rooting systems to seasonally dry climates is crucial to explain the current dominance, productivity and evapotranspiration of evergreen forests in tropical South America.

1 Introduction

Tropical evergreen forest is the naturally dominant biome type in South-America over a large climatic range including regions with a marked dry season (Hirota et al., 2011; Xiao et al., 2006). To withstand seasonal shortages of precipitation and sustain productivity, trees with evergreen phenology often have access to deep soil water via deep roots (Brum et al., 2019; Canadell et al., 1996; Johnson et al., 2018; Kim et al., 2012; Markewitz et al., 2010). Consequently, recent studies suggest a heterogeneous spatial pattern of maximum rooting depth across tropical forest biomes in South-America which differs over the order of magnitudes depending on local groundwater, soil and climate conditions (Canadell et al., 1996; Fan et al., 2017). ~~In this study we revisit the hypothesis that tree rooting depth is a crucial variable to explain the geographical distribution of main phenology strategies such as evergreen and deciduous, as well as the observed local to continental pattern of productivity, biomass storage, evapotranspiration (ET) and consequently moisture recycling (Fan et al., 2017; Jobbágy and Jackson, 2000; Kleidon and Heimann, 2000; Langan et al., 2017; Nepstad et al., 1994; Stahl et al., 2013). To test this hypothesis, dynamic global vegetation models (DGVMs) seem to be promising tools, as those models are suitable to~~

47 ~~project the development of vegetation formation and ecosystem functioning systematically and on large spatial scales~~
48 ~~(Huntingford et al., 2013; Liu et al., 2018; Weber et al., 2009). However, most DGVMs do not represent the diversity of~~
49 ~~rooting depth or tree rooting strategies (Warren et al., 2015a). In general these models condense the diversity of such~~
50 ~~functional tree traits into so called plant functional types (PFTs), which represent average tree growing strategies on scales as~~
51 ~~large as biomes. Here, often a shallow rooting depth for tree PFTs is assumed, i.e. most roots are distributed downwards to a~~
52 ~~few meters of depths at maximum (Arora and Boer, 2003; Best et al., 2011; Guimberteau et al., 2017; Lawrence et al., 2011;~~
53 ~~Östle et al., 2009; Schaphoff et al., 2018; Smith et al., 2014).~~
54 ~~In favour of the rooting depth hypothesis, most DGVMs in the past had problems reproducing the extent of South America's~~
55 ~~tropical evergreen forests, as well as its seasonal productivity and ET especially in regions with seasonal rainfall (Baudena et~~
56 ~~al., 2014; Liu et al., 2018, 2017; Restrepo-Coupe et al., 2017). So far different modelling approaches were presented which~~
57 ~~highlighted the crucial role of rooting depth for the productivity and therefore the distribution of evergreen trees in South-~~
58 ~~America. So far different approaches were presented trying to solve this problem in DGVMs and similar models by allowing~~
59 ~~for variable rooting strategies.~~ In a pioneering study more than 20 years ago, Kleidon and Heimann (1998) systematically
60 searched for rooting strategies which yield highest net primary productivity over South America ~~in a~~ with a dynamic global
61 vegetation model (DGVM) to explain intra-annual rates of ET and vegetation cover. Follow up studies further underlined the
62 importance of deep roots for the ~~climate system~~ water cycle of South America (Kleidon and Heimann, 2000). Accordingly,
63 Lee *et al.* (2005) found that allowing for deep roots and hydraulic redistribution of water in the soil column in a general
64 circulation model (GCM) enhances improved simulated Amazon forest productivity and evapotranspiration (ET) in the dry
65 season. Baker *et al.* (2008) came to similar results when introducing deep roots in a land surface model. Ichii *et al.*, (2007)
66 found that constraining rooting depth across the Amazon based on satellite ~~data yields~~ derived data of forest productivity
67 yields similar results in a terrestrial ecosystem model. More recently, Langan, Higgins and Scheiter (2017) showed for the
68 same study area how diverse rooting strategies in a tree individual and trait-based DGVM can improve simulated intra-
69 annual productivity and ET as well as ~~and~~ better explain patterns of different tropical biome types and biomass in ~~connection~~
70 with fire-prone ecosystems.
71 While these studies are important steps to acknowledge the diversity of tree rooting ~~strategies~~ depth and its effects on ET and
72 forest productivity, some assumptions of the underlying models might decrease the liability of their results ~~and therefore~~
73 ~~pose arguments against the rooting depth hypothesis~~. These assumptions are related to 1) resource investment, 2) temporal
74 growth and 3) physical constraints of rooting depth:
75 -1) Most global scale vegetation models so far do not account for coarse roots (Warren et al., 2015a) even though they can
76 make up the majority of total root biomass (Xiao et al., 2003). This approach may be sufficient when employing shallow tree
77 rooting strategies only, but with increasing rooting depth, costs for coarse roots increases substantially. Since the amount of
78 resources trees can allocate to their processes and structures is finite, a local adaptation of tree rooting depth must follow a
79 trade-off between above- and below-ground resource investment (Nikolova et al., 2011). Generally, above-ground
80 investments into leaf and stem growth can increase light absorption and CO₂ uptake, while below-ground investments can
81 increase the uptake of water and nutrients. Depending on local environmental and competitive conditions one or the other
82 allocation strategy might be more advantageous, eventually leading to substantial regional variation in the mean ratios
83 between below-ground to above-ground biomass ~~ratios~~ (Leuschner et al., 2007; Mokany et al., 2006). Therefore, the
84 simulated spectrum of tree rooting strategies which can survive and co-exist should be in accordance with this crucial trade-
85 off. 2) In contrast to above-ground stem growth, most ~~global scale vegetation models~~ DGVMs so far do not simulate gradual
86 root growth (Warren et al., 2015a). Instead ~~PFTs are~~ simulated vegetation types are assigned a constant relative distribution
87 of fine roots throughout the soil column at any point in space and time (Best et al., 2011; Lawrence et al., 2011; Schaphoff et
88 al., 2018; Smith et al., 2014). As under the above-mentioned simplification under 1), this approach may be sufficient when
89 accounting for shallow rooting strategies only, but when the maximum tree rooting depth ~~of PFTs strongly diverges~~

90 strongly increased, it is questionable that the time needed to reach this depth is negligible, especially when accounting for
91 PFT-competition of different vegetation types. Rooting depth increases rather gradually and non-linearly over a tree's
92 lifetime with a velocity driven by a mix of plastic optimization and allometric determination (Brum et al., 2019; Brunner et
93 al., 2015; Nikolova et al., 2011; Poorter et al., 2012; Warren et al., 2015b). Even though non-DGVM-related smaller-scale
94 models have implemented root optimization schemes in the past (Schymanski et al., 2008), the knowledge base for a
95 mechanistic bottom-up modelling approach of plastic root optimization is very sparse (Jenik, 2010; Poorter et al., 2012;
96 Warren et al., 2015b) and knowledge on certain allometric rules (Brum et al., 2019; Eshel and Grünzweig, 2013; Mokany et
97 al., 2006) seems enough to be applied in DGVMs global vegetation models. 3) Most DGVMs global vegetation models so far
98 do not account for a location-dependent soil depth, but apply a constant soil depth across the globe (Best et al., 2011;
99 Guimberteau et al., 2017; Lawrence et al., 2011; Ostle et al., 2009; Schaphoff et al., 2018; Smith et al., 2014). Again, this
100 approach may be sufficient when accounting for shallow rooting strategies only, but allowing for deep tree rooting strategies
101 should go in parallel with their potential physical barriers. Recent data products on global soil depth now enable to better
102 constrain rooting depth in DGVMs-vegetation models across scales (Pelletier et al., 2016).

103 Here we overcome the above mentioned limitations and present a new approach of diversifying tree rooting strategies of
104 tropical plant functional types (PFTs) in the DGVM LPJmL4.0 (Lund-Potsdam-Jena managed Lands; Schaphoff *et al.*, 2018)
105 which increases the ecological liability with the following aspects: 1) A global product of soil depth restricts the mMaximum
106 tree rooting depth-is restricted to a recent global product of soil depth, 2) simulated-PFTs are sub-divided according to a
107 broad spectrum of different possible tree rooting strategies-were chosen to represent a wide-with a range of maximum
108 rooting depths between 0.5 and 18 m, 3) all tree-rooting-strategies-of-this-spectrum-sub-PFTs grow in competition and PFT
109 performancetheir individual performance-determines dominance, 4) dominance is supported by best performing rooting
110 strategiessub-PFTs increasing their establishment rate, 5) PFTs have to investsub-PFTs have to invest carbon-into coarse
111 roots-as well, i.e. acknowledging the trade-off between growing deeper roots and allocating available carbon to other
112 compartments (stem and leaf growth), and 6) tree-PFT-roots-sub-PFT roots are growing deeper over time depending on tree
113 height.

114 Given these new model developments we here re-evaluate the hypotheses that

115 I) —climate and soil depth determine dominant tree rooting strategies.

116 II) —tree rooting depth influences the distribution and dominance -and

117 III) —diverse tree rooting strategies are key to explain rates of evapotranspiration and productivity

118 of tropical evergreen forests in South America. Given these new model developments we here re-evaluate the hypothesis that
119 varying tree rooting depth is key to explain major patterns of evapotranspiration, productivity and the geographical
120 distribution of tropical evergreen forests in South America, as we acknowledge a diversity of different competing tree
121 rooting strategies as well as resource investment, temporal growth and physical constraints of rooting depth. Therefore, we
122 compare several model versions of LPJmL4.0 differing in the above-mentioned model developments and evaluate simulated
123 evapotranspiration, productivity, biomass and spatial distribution of evergreen and deciduous tree PFTs using different
124 sources of validation data.

125 **2 Materials and Methods**

126 **2.1 The LPJmL4.0 model**

127 LPJmL4.0 is a process-based Dynamic Global Vegetation Model (DGVM) which simulates the surface energy balance,
128 water fluxes, fire disturbance, carbon fluxes and stocks of the global land (Schaphoff et al., 2018). Plant productivity is
129 modelled on the basis of leaf-level photosynthesis responding to climatic and environmental conditions, atmospheric CO₂
130 concentration, canopy conductance, autotrophic respiration, phenology and management intensity. Fire disturbance is

131 modelled using the simple fire module Glob-FIRM (Thonicke et al., 2001) which relates the length of the fire season to
132 fractional annual area burnt. The model simulates 11 plant functional types (PFTs), 3 bioenergy functional types (BFTs) and
133 12 crop functional types (CFTs), to represent average plants of natural vegetation, bioenergy plantations and agriculture,
134 respectively. Three PFTs represent the natural vegetation of the tropics and sub-tropics namely the “tropical broadleaved
135 evergreen tree” mainly representing tropical evergreen forest, the “tropical broadleaved deciduous tree” representing tropical
136 dry forest and the woody component of savanna and “tropical herbs” representing the herbaceous layer in grasslands,
137 savanna and forests.

138 The standard spatial model resolution is a $0.5^\circ \times 0.5^\circ$ longitude-latitude grid. For each grid cell the fractional coverage of
139 bioenergy and agricultural BFTs and CFTs follows a prescribed land-use data set, whereas in the remaining grid-cell area
140 natural PFTs grow in competition.

141 **2.2 A new tree rooting scheme for LPJmL4.0**

142 All changes made to LPJmL4.0 in order to simulate variable tree rooting strategies resulted in a new sub-version of
143 LPJmL4.0 which we call LPJmL4.0-VR hereafter (where “VR” stands for “variable roots”). A detailed description of our
144 modelling approach can be found in Appendix A.

145 For our purposes we extended the general maximum soil depth of 3 m in LPJmL4.0 to 20 m in LPJmL4.0-VR, (but restrict
146 it to local soil depth information at the spatial model resolution of $0.5^\circ \times 0.5^\circ$; Sect. 2.3.2). We applied the same basic
147 scheme for vertical soil layer partitioning from LPJmL4.0 (Schaphoff et al., 2018), in order to keep model differences small
148 (Appendix A Sect. 1.1 & Table A1). We increased the amount of rooting strategies for each of the 2 tropical tree PFTs
149 (broadleaved evergreen and broadleaved deciduous), by splitting each PFT into 10 sub-PFTs. Each of those 10 sub-PFTs
150 was assigned a different maximum vertical distribution of fine roots throughout the soil column following classical
151 allometric rules applied in LPJmL4.0 (Appendix A Sect. 1.3 & Figure A1). Those distributions were chosen in order to
152 allow the sub-PFTs to reach different maximum rooting depths in discrete steps between 0.5 and 18 m (Table A2). We here
153 refer to the depth at which the cumulated fine root biomass from the soil surface downwards amounts to 95% (D_{95_max} ; Eq.
154 A3).

155 To account for additional carbon investments needed to grow deeper rooting systems we introduced two new carbon pools,
156 namely root sapwood and root heartwood (Appendix A Sect. 1.4). Like stem sapwood in LPJmL4.0, also root sapwood in
157 LPJmL4.0-VR needs to satisfy the assumptions of the pipe model (Shinozaki et al., 1964; Waring et al., 1982). This
158 implementation creates a trade-off between below-ground and above-ground carbon investment. To allow for dynamic root
159 growth we implemented a logistic root growth function, which calculates a general maximum conceivable tree rooting depth
160 depending on tree height (Appendix A Sect. 1.5), in approximation to the findings of Brum *et al.* (2019). Consequently, each
161 sub-PFT shows a logistic growth of rooting depth which is dependent on the sub-PFT height and which saturates towards its
162 specific D_{95_max} (Fig. A2). Therefore, limitations of aboveground sub-PFT growth due to below-ground carbon investment of
163 different tree rooting strategies (Sect. 2.2.4) are equal in the sapling phase of all sub-PFTs (starting from bare ground) but
164 diverge with increasing sub-PFT height. In the case temporal root depths exceeds the grid-cell specific local soil depth (as
165 prescribed by local soil depth information, see Sect. 2.3.2) all the respective fine root biomass exceeding this soil depth is
166 transferred to the last soil layer matching this soil depth (see also Fig. 1 and Supplementary Video 1 for a visualization of
167 new below-ground carbon pools and root growth in LPJmL4.0-VR under [http://www.pik-](http://www.pik-potsdam.de/~borissa/LPJmL4_VR/Supplementary_Video_1.pptx)
168 [potsdam.de/~borissa/LPJmL4_VR/Supplementary_Video_1.pptx](http://www.pik-potsdam.de/~borissa/LPJmL4_VR/Supplementary_Video_1.pptx).

169 To fully investigate the effects of 20 tropical sub-PFTs growing in competition we adjusted the original PFT establishment
170 routine of LPJmL4.0 (Appendix A Sect. 1.6). The adjustments lead to a higher establishment rate for productive sub-PFTs
171 relative to their spatial dominance and vice versa, without changing the overall establishment rate as originally set by
172 Prentice et al. (1993). The adjusted establishment routine has the effect that non-viable sub-PFTs are outcompeted over time.

173 Furthermore, we increased the universal and constant maximum background mortality rate of tree PFTs in LPJmL4.0-VR to
174 7% in order to counter-balance increased survival rates and therefore biomass accumulation under enhanced water access
175 (Appendix A Sect. 1.7).

176 **2.2 A new tree rooting scheme for LPJmL4.0**

177 In this section we describe the new basic scheme for soil layer partitioning, the new tree rooting scheme, the simulation of
178 belowground carbon investment, and how different tree rooting strategies (implemented in the new scheme) compete. All
179 changes made to LPJmL4.0 described in this section result in a new sub-version of LPJmL4.0 which we call LPJmL4.0-VR
180 hereafter (where “VR” stands for variable roots).

181 **2.2.1 Scheme for soil layer partitioning**

182 LPJmL4.0 employs a globally universal soil depth of 3 m. For LPJmL4.0-VR we extended the general maximum soil depth
183 to 20 m (but restrict it to local soil depth information at spatial model resolution; Sect. 2.3.2). We applied the same basic
184 scheme for soil layer partitioning from LPJmL4.0 (Schaphoff et al., 2018), in order to keep model differences small (Table
185 A1). We chose a maximum of 20 m soil depth to considerably increase the maximum soil depth compared to constant 3 m in
186 LPJmL4.0, while keeping the increment of computational demand connected to adding more soil layers within an acceptable
187 range. Equal to LPJmL4.0 (Schaphoff et al., 2018), we use a grid-cell specific soil texture information which is applied to the
188 whole soil column.

189 **2.2.2 Water balance, infiltration and percolation**

190 We here provide a very brief description of LPJmL’s water balance and soil hydrology. A detailed description can be found
191 in Schaphoff et al. (2018).

192 Hydraulic conductivity and water holding capacity (water content at permanent wilting point, at field capacity, and at
193 saturation) for each grid cell are derived from information on soil texture from the Harmonized World Soil Database
194 (HWSD) version 1 (Nachtergaele et al., 2009) and relationships between texture and hydraulic properties from Cosby et al.
195 (1984). Each soil layer’s (Sect. 2.2.1) water content can be altered by infiltrating rainfall and percolation. The soil water
196 content of the first soil layer determines the infiltration rate of rain and irrigation water. The excess water that does not
197 infiltrate generates surface water runoff. Water percolation through the soil layers is calculated by the storage routine
198 technique (Arnold et al., 1990) as used in regional hydrological models such as SWIM (Krysanova et al., 1998). Water
199 percolation thus depends on the hydraulic conductivity of each soil layer and the soil water content between field capacity
200 and saturation at the beginning and the end of the day for all soil layers. Similar to water infiltration into the first soil layer,
201 percolation in each soil layer is limited by the soil moisture of the following lower layer. Excess water over the saturation
202 levels forms lateral runoff in each layer and contributes to subsurface runoff. Surface and subsurface runoff accumulate to
203 river discharge. The routines for water balance, infiltration and percolation were not changed for LPJmL4.0-VR. Thus the
204 routines now apply for soil columns of up to 20 m depth (Sect. 2.2.1).

205 **2.2.3 Diversifying general tree rooting strategies**

206 In LPJmL4.0 the tree rooting strategy of a PFT is reflected by a certain prescribed vertical distribution of fine roots
207 throughout the soil column. Each soil layer l is assigned a PFT specific relative amount of fine roots $rootdist_l$:

$$208 \quad rootdist_l = \frac{rootdist(z_l)}{rootdist(z_0)} \quad \text{Eq. (1)}$$

209 where z_l is the soil layer boundary depth in cm of each soil layer l and $rootdist(z_l)$ is the relative amount of fine roots between
210 the forest floor and the boundary of soil layer l . The function $rootdist(z)$ is defined following Jackson *et al.* (1996):

$$211 \quad rootdist = \frac{1}{1 + \exp(-\frac{z - z_0}{\sigma})} \quad \text{Eq. (2)}$$

212 where β is a constant parameter shaping the vertical distribution of fine roots and therefore determining the tree rooting
213 strategy $\text{an_d_}z_{\text{bottom}}$ is the maximum soil depth in cm. In LPJmL4.0 each PFT is assigned a different β value reflecting the
214 average tree rooting strategy on this broad PFT scale (Schaphoff et al., 2018).

215 To quantify the maximum rooting depth of PFTs that actually results from this approach (Eq. 1&2) we here calculate the
216 depth at which the cumulated fine root biomass from the soil surface downwards is 95% (D_{95_max}) as follows:

$$= \frac{1}{\beta} \ln \left(\frac{1}{0.05} \right) \quad \text{Eq. (3)}$$

218 In LPJmL4.0 the β values of tropical tree PFTs are set to 0.962 for the tropical broadleaved evergreen tree and to 0.961 for
219 the tropical broadleaved deciduous tree following Jackson et al. (1996). According to Eq. 3 both PFTs have a D_{95_max} smaller
220 than 1 m. For LPJmL4.0 VR we extended this representation of tree rooting strategies by splitting both tropical tree PFTs
221 into 10 sub PFTs and assigned each with a different β value. These values were chosen to cover a range of different D_{95_max}
222 values between 0.5 and 18m (Table 1). We chose 18 m as the largest D_{95_max} value in order to avoid that roots of the
223 respective sub PFT significantly exceed the maximum soil depth of 20 m (see also 2.2.5). Fig. 1 shows the new maximum
224 distribution of fine roots throughout the soil column for the different β values chosen (Table 1).

225 2.2.4 Belowground carbon investment

226 Tropical trees can avoid water stress under seasonally dry climate by growing relatively deep roots (Brum et al., 2019; Fan et
227 al., 2017) which goes along with increased below ground carbon investment. Thus, the need for deep water access creates a
228 trade off between below ground and above ground carbon investment. Therefore, a new carbon allocation scheme for
229 LPJmL4.0 VR was necessary to account for this trade off in order to reproduce observed local to regional patterns and
230 distributions of tree rooting strategies instead of prescribing them. In LPJmL4.0 VR we introduced two new carbon pools,
231 namely root sapwood and root heartwood. Like stem sapwood in LPJmL4.0, also root sapwood in LPJmL4.0 VR needs to
232 satisfy the assumptions of the pipe model (Shinozaki et al., 1964; Waring et al., 1982). The pipe model describes, that for a
233 certain amount of leaf area a certain amount of water conducting tissue must be available. In LPJmL4.0 the cross sectional
234 area of stem sapwood needs to be proportional to the leaf area LA_{ind} as follows:

$$= k_{la-sa} LA_{ind} \quad \text{Eq. (4)}$$

236 where k_{la-sa} is a constant describing the ratio of leaf area and stem sapwood cross sectional area (SA_{ind}). In LPJmL4.0 VR we
237 also apply the pipe model to root sapwood. Root sapwood cross sectional area in the first soil layer is equal to stem sapwood
238 cross sectional area, as all water must be transported through the root sapwood within this soil layer. In the following soil
239 layers downwards, root sapwood cross sectional area decreases by the relative amount of fine roots in all soil layers above
240 (Fig. 2). Root sapwood is turned into root heartwood at an equal rate as stem sapwood is turned into stem heartwood, i.e. 5%
241 per year as implemented in LPJmL4.0 (see Schaphoff et al., 2018).

242 2.2.5 Root growth

243 In LPJmL4.0 (Schaphoff et al., 2018) no vertical root growth is simulated, thus the relative distribution of fine roots over the
244 soil column is constant over space and time. It means that PFTs starting from bare ground in a sapling stage display the same
245 relative distribution of fine roots throughout the soil column as a full grown forest which contradicts the principles of
246 dynamic root growth over a tree's lifetime. Applied to LPJmL4.0 VR, the belowground biomass of an initialized deep
247 rooting strategy sub PFT would exceed its aboveground biomass (AGB) by order of magnitudes when considering coarse
248 roots. Consequently, deep rooting strategies would always be disadvantageous, calling for modelling gradual root growth in
249 LPJmL4.0 VR. Unfortunately, little is known about how roots of tropical trees grow over time, given the fact that this
250 research field is strongly time and resource demanding, and at the same time the variety of tree species, rooting strategies
251 and environmental conditions are large (Jenik, 2010). A recent promising study by Brum et al. (2019) was able to capture the
252 effective functional rooting depth (EFRD) of different size classes of 12 dominant tree species in a seasonal Amazon forest

where tree roots grow considerably deep with maximum values reaching below 30 m. To our knowledge this is the only study capturing the relation between the size of tropical trees and their maximum rooting depth in a high spatial resolution covering sufficient tree height classes in order to derive a functional relation between tree height and rooting depth. Following the findings of Brum *et al.* (2019), we here implemented a logistic root growth function, which calculates a general maximum conceivable tree rooting depth D depending on tree height:

$$D = \frac{S}{1 + \exp(-k(h - D_0))} \quad \text{Eq. (5)}$$

where S is the maximum soil depth in the model (20 m), k is the growth rate (set to 0.02), h is the average tree height of a PFT in m and D_0 is the initial rooting depth of tree PFT saplings (set to 0.1 m; tree saplings in LPJmL4.0-VR are initialized with a height of 0.45 m as in LPJmL4.0). The distribution of fine root biomass of each sub-PFT in the soil column is then adjusted according to D at each time step, by restricting z_{bottom} in Eq. 2. Every time D crosses a specific soil layer boundary (Sect. 2.2.1) z_{bottom} is assigned the value of the next soil layer boundary. Thus, z_{bottom} increases in discrete steps. Consequently, each tree rooting strategy allowed for in this study (Sect. 2.2.3) shows a logistic growth of rooting depth which is dependent on the sub-PFT height and which saturates towards its specific maximum rooting depth (Fig. 3). Therefore, limitations of aboveground sub-PFT growth due to below-ground carbon investment of different tree rooting strategies (Sect. 2.2.4) are equal in the sapling phase of all sub-PFTs (starting from bare ground) and start to diverge with increasing sub-PFT height. In the case D exceeds the grid-cell specific local soil depth (as prescribed by the soil thickness input, see Sect. 2.3.2) all the respective fine root biomass exceeding this soil depth is transferred to the last soil layer matching this soil depth (see also Fig. 2 right panel and Supplementary Video 1 for a visualization of root growth under http://www.pik-potsdam.de/~borissa/LPJmL4_VR/Supplementary_Video_1.pptx).

The parameter k in Eq. 5 was chosen to preserve the slope of the 75%ile function describing the relation between tree height and EFRD as found in Brum *et al.* (2019). We could not implement any of the original functions as suggested in Brum *et al.* (2019) since they deliver unrealistic low values of rooting depth (between 0 and 10cm) for trees ≤ 10 m, which results in a strong competitive disadvantage against herbaceous PFTs in LPJmL4.0-VR. We decided for the slope of the 75%ile function to allow for root growth rates close to the maximum which also allows for the largest $D_{95\text{-max}}$ values in this study (Sect. 2.2.3) to be reached. Note that Brum *et al.* (2019) originally propose a relation between tree diameter at breast height (DBH) and EFRD. For our purposes we related rooting depth to tree height (h), which is calculated from DBH in LPJmL4.0 according to Huang *et al.* (1992):

$$h = \frac{k_{allom2} DBH}{k_{allom3}} \quad \text{Eq. (6)}$$

where k_{allom2} and k_{allom3} are constants set to 40 and 0.67, respectively (Schaphoff *et al.*, 2018).

2.2.6 Competition of rooting strategies

In each grid-cell all sub-PFTs of the evergreen and deciduous tree PFTs compete for light and water following LPJmL4.0's approach to simulate plant competition. In LPJmL4.0, the number of new PFT saplings per unit area (est_{PFT} in $\text{ind m}^{-2} \text{a}^{-1}$) which are established each year is proportional to a maximum establishment rate k_{est} and to the sum of foliage projected cover (FPC; a relative number between 0 and 1) of all tree PFTs present in a grid-cell (FPC_{TREE}). It declines in proportion to canopy light attenuation when the sum of woody FPCs exceeds 0.95, thus simulating a decline in establishment success with canopy closure (Prentice *et al.*, 1993):

$$est_{PFT} = k_{est} (1 - FPC_{TREE}) \quad \text{Eq. (7)}$$

where est_{PFT} is the number of established tree individuals ($\text{ind m}^{-2} \text{a}^{-1}$). It is important to note that LPJmL4.0 does not simulate individual trees. As a common method of DGVM's, tree saplings enter the average individual of a PFT as described in Schaphoff *et al.* (2018).

To allow for environmental filtering of tree rooting strategies which are best adapted to local environmental conditions, we changed the standard tree establishment scheme in LPJmL4.0 VR. Now, the establishment rates of sub-PFTs (est_{sub_PFT}) are additionally weighted by the local dominance of each sub-PFT as follows:

$$\text{Eq. (8)}$$

where FPC_{sub_PFT} is the FPC of each sub-PFT. The new term leads to a higher establishment rate for productive sub-PFTs relative to their spatial dominance and vice versa, without changing the overall establishment rate as set by Prentice et al. (1993). This function has the effect that non-viable sub-PFTs are outcompeted over time.

2.2.7 Background mortality

In LPJmL4.0 background mortality is modelled by a fractional reduction of PFT biomass, which depends on growth efficiency (Schaphoff et al., 2018). This annual rate of mortality is limited by a constant maximum mortality rate of 3% of tree individuals per year which is applied to all tree PFTs. In other words, the fastest total biomass loss of a tree PFT due to low growth efficiency can happen within about 33 simulation years. In general, this maximum mortality rate can be regarded as a global tuning parameter of biomass accumulation as it caps the maximum biomass loss. Since many mechanisms influencing tree mortality in the real world, e.g. hydraulic failure (Johnson et al., 2018), are not yet implemented in most DGVMs including LPJmL4.0 (Allen et al., 2015), the parameterization of a background tree mortality remains a challenging topic. Under the current model status of LPJmL4.0 maximum mortality rates are a necessary feature, while future model development must overcome the concept of applying a maximum mortality rate by refining and implementing most important mechanisms that influence tree mortality.

In LPJmL4.0 VR tree PFTs can access water in soil depths which were formerly inaccessible. This enhances the general growth efficiencies of tree PFTs and consequently decreases their overall background mortality. Since global biomass pattern simulated with LPJmL4.0 were already in acceptable range, the maximum background mortality in LPJmL4.0 VR was calibrated and is now increased to 7% in order to counter balance increased survival rates and therefore biomass accumulation.

2.3 Model input data

2.3.1 Climate input data

All versions of LPJmL used in this study (Sect. 2.4) were forced with 4 different climate inputs each delivering the climate variables air temperature, precipitation, long-wave and shortwave downward radiation at daily or monthly resolution:

1) WATCH Forcing Data (WFD) + WATCH Forcing Data methodology applied to ERAInterim data. A combination of the WATCH data set (Weedon et al., 2011) and the WFDEI data set (Weedon et al., 2014) as used in the ISIMIP project (<https://www.isimip.org/gettingstarted/input-data-bias-correction/details/5/>). This input data set is called WATCH+WFDEI hereafter.

2) Global Soil Wetness Project Phase 3 (GSWP3) (Kim et al., no date; <http://hydro.iis.u-tokyo.ac.jp/GSWP3/index.html>).

3) NOAA Global Land Assimilation System version 2.0 (GLDAS, Rodell et al., 2004).

4) Climate forcing as in Schaphoff et al. (2018) with monthly precipitation provided by the Global Precipitation Climatology Centre (GPCP Full Data Reanalysis version 7.0; (Becker et al., 2013), daily mean temperature from the Climate Research Unit (CRU TS version 3.23, University of East Anglia Climatic Research Unit, 2015; Harris et al., 2014), shortwave downward radiation and net downward radiation reanalysis data from ERA-Interim (Dee et al., 2011), and number of wet days from (New et al., 2000) used to allocate monthly precipitation to individual days.

This input data set is called CRU hereafter.

332 2.3.2 Soil and sediment thickness

333 For this study, we regridded a global 1 x 1 km soil and sediment thickness product (Pelletier et al., 2016) to the 0.5° x 0.5°
334 spatial resolution of LPJmL4.0-VR, set the global maximum value to 20 m according to the maximum soil depth chosen for
335 LPJmL4.0-VR (Sect. 2.2.1 & Appendix A Sect. 1.1), and used the resulting map as grid cell specific model input (Fig.
336 A4A3). Regridding was done using the software R (R Core Team, 2019) with the package “raster” (Hijmans and van Etten,
337 2016). We used the aggregate function to calculate the average value of all Pelletier et al. (2016) data entries falling into the
338 coarser 0.5° grid of LPJmL.

339 2.4 Model versions and simulation protocol

340 In order to investigate the impact of simulating variable rooting strategies and root growth, we employ 3 model versions of
341 LPJmL in this study: 1) LPJmL4.0, 2) LPJmL4.0-VR, and 3) LPJmL4.0-VR-base. LPJmL4.0-VR-base has the same settings
342 as LPJmL4.0-VR except variable rooting strategies, i.e. using ~~the 2 β values~~ the 2 rooting strategy parameterizations of
343 LPJmL4.0 (Appendix A Sect. 1.3) for the respective 10 sub-PFTs of the tropical broadleaved evergreen PFT ($\beta=0.962$) and
344 the tropical broadleaved deciduous PFT (~~$\beta=0.961$~~). We regard LPJmL4.0-VR-base as the baseline model of this study,
345 because comparisons to LPJmL4.0-VR enable to investigate differences caused by the presence or absence of variable tree
346 rooting strategies.

347 Each simulation was initialized with 5000 simulation years of spin up from bare ground without land-use by periodically
348 cycling the first 30 years of the respective climate data set (1901-1930 for WATCH+WFDEI, GSWP3, CRU and 1948-1977
349 for GLDAS) and using a pre-industrial atmospheric CO₂ level of 278 ppm. The first spin-up ensures that carbon pools and
350 local distributions of PFTs and sub-PFTs are in equilibrium with climate (Schaphoff et al., 2018). In a second spin-up phase
351 cycling the same 30 years of climate data, historical land-use and changing levels of atmospheric CO₂ concentration are
352 introduced. The second spin-up starts in the year 1700 and ends with the first year available in each climate data set. Land-
353 use is updated annually as described in Schaphoff et al. (2018). Before the year 1840 a constant pre-industrial atmospheric
354 CO₂ concentration of 278 ppm is prescribed. After this year atmospheric CO₂ increases annually based on data of Tans and
355 Keeling (2015) as described in Schaphoff et al. (2018). After the second spin up, transient simulations start with the first year
356 available in each climate data set and end in 2100. Land-use and atmospheric CO₂ are consistently updated annually
357 continuing to follow the same data sets as used in the second spin-up.

358 At the beginning of the first spin-up, all sub-PFTs in LPJmL4.0-VR and LPJmL4.0-VR-base have the same chance to
359 establish, i.e. tree rooting strategies are uniformly distributed. During the spin-up simulations, local environmental filtering
360 and competition in connection with PFT-dominance dependent establishment rates (Sect. 2.2 & Appendix A Sect. 2.2.1.6)
361 determine which tree rooting strategies are best adapted-suited and which are outcompeted. Therefore, the transient
362 simulations already start with distinct distributions of tree rooting strategies.

363 2.5 Model validation

364 2.5.1 Validation data

365 *Regional biomass pattern*

366 For evaluation of simulated regional pattern of AGB we compare the results of the 3 LPJmL model versions used in this
367 study to two remote sensing based biomass maps (Avitabile et al., 2016; Saatchi et al., 2011) which were regridded to the
368 spatial resolution of the LPJmL models. Data of Avitabile et al. (2016) was regridded using the software R (R Core Team,
369 2019) with the package raster (Hijmans and van Etten, 2016). We used the aggregate function to calculate the average value
370 of all Avitabile et al. (2016) data entries falling into the coarser 0.5° grid of LPJmL. Regridded data of Saatchi et al. (2011)
371 was taken from Carvalhais et al. (2014).

372 *Local scale evapotranspiration and productivity*

373 To evaluate simulated local ET and net ecosystem exchange (NEE) of the 3 LPJmL versions used in this study, we compare
374 Fluxnet eddy covariance measurements of ET at 7 sites and NEE at 3 sites across the study region (Bonal *et al.*, 2008;
375 Saleska *et al.*, 2013, Table A2A3) to respective simulated rates of local ET and NEE. We used only 3 sites for NEE
376 comparisons, because only those sites provided continuous data covering more than 2 years. Fluxnet data was downloaded
377 from <https://fluxnet.fluxdata.org> (under DOI: [10.18140/FLX/1440032](https://doi.org/10.18140/FLX/1440032) and DOI: [10.18140/FLX/1440165](https://doi.org/10.18140/FLX/1440165)) in October 2017
378 and from https://daac.ornl.gov/LBA/guides/CD32_Brazil_Flux_Network.html in November 2019.

379 *Continental scale gridded evapotranspiration products and selection of regions*

380 To evaluate the simulated ET over large regions and during a long period (1981-2010), we use three global gridded datasets:
381 Global Land Data Assimilation System Version 2 (Rodell *et al.*, 2004), ERA-Interim/Land (ERA-L, Balsamo *et al.*, 2015)
382 and Global Land Evaporation Amsterdam Model v3.2 (GLEAM, Miralles *et al.*, 2011; Martens *et al.*, 2017).

383 GLDAS and ERA-L are reanalysis products, meaning that they are land surface models forced with meteorological data that
384 has been corrected with observations to give better estimates of land surface variables. The selection of these two products is
385 based on the study of Sörensson and Ruscica (2018), who found that they have a better performance over South America
386 than other reanalysis and satellite-based ET products. GLDAS uses the land surface model Noah (Ek *et al.*, 2003) forced by
387 Princeton meteorological dataset version 2.2 (Sheffield *et al.*, 2006). The soil depth of Noah is 2 m and the model uses four
388 soil layers and vegetation data from University of Maryland (<http://glcf.umd.edu/data/landcover/>). ERA-L uses the land
389 surface model HTESSEL (Hydrology-Tiled ECMWF Scheme for Surface Exchanges over Land, Balsamo *et al.*, 2009)
390 forced by ERA-Interim atmospheric data with a GPCP based correction of monthly precipitation. The soil depth of ERA-L
391 is 2.89 m, the model uses four soil layers and vegetation data from ECOCLIMAP (Masson *et al.*, 2003).

392 GLEAM uses the Priestley-Taylor equation to estimate the potential ET and a set of algorithms with meteorological and
393 vegetation satellite data as input to calculate the actual ET. The version used here, GLEAMv3.2a (Martens *et al.*, 2017,
394 downloaded from <https://www.gleam.eu/#downloads>) uses precipitation input from MSWEP v1.0 (Beck *et al.*, 2017),
395 vegetation cover from the MODIS product MOD44B, remotely sensed Vegetation Optical Index from CCI-LPRM (Liu *et al.*
396 *et al.*, 2013) and assimilates soil moisture from both remote sensing (ESA CCI SM v2.3, Liu *et al.*, 2012) and land-reanalysis
397 (GLDAS Noah, Rodell *et al.*, 2004). The original spatio-temporal resolution of GLDAS and GLEAM is 0.25° x 0.25° while
398 for ERA-L it is 0.75° x 0.75°. Monthly time series were calculated from daily values for the three datasets. Hereafter, we use
399 the short names GLDAS, ERA-L and GLEAM for the described reference datasets.

400 For the temporal analysis of ET we used five climatological regions across the study area: Northern South America (NSA),
401 Equatorial Amazon West (EQ W), Equatorial Amazon East (EQ E), Southern Amazon (SAMz), and South American
402 Monsoon System region (SAMS) (see Fig. 9f). These regions result from a K-means clustering analysis of the annual
403 cycles of the main drivers of ET: precipitation and surface net radiation (for details see Sörensson and Ruscica, 2018).
404 Additionally we divided the large EQ region used by Sörensson and Ruscica (2018) in two smaller (EQ W and EQ E) at
405 60°W, since this is the approximate division between regimes that have a maximum climatological water deficit (MCWD;
406 Sect. 2.5.3) of around -200 mm per year (EQ W), and of around -500 mm per year (EQ E).

407 *Spatial distribution of vegetation types*

408 To evaluate the simulated regional distribution of simulated biome types of the 3 LPJmL versions we compare our results to
409 satellite-derived vegetation composition maps from ESA Land cover CCI V2.0.7 (Li *et al.*, 2018) which were reclassified to
410 the PFTs of LPJmL from Forkel *et al.* (2014). In this dataset PFT dominance is indicated by foliage projected cover (FPC)
411 which is also a standard output variable of the 3 LPJmL model versions allowing a direct comparison to model results.

412 *Spatial pattern of rooting depth*

413 We compare regional patterns of mean rooting depth simulated with LPJmL4.0-VR to a maximum depth of root water
414 uptake map (Fan *et al.*, 2017) which was regridded to the 0.5° x 0.5° spatial resolution of LPJmL4.0-VR. This product was

415 inversely modelled by taking the dynamically interacting variables soil water supply and plant water demand into account. In
416 Fan et al. (2017) supply was based on climate, soil properties and topography and demand of plant transpiration deduced
417 from remotely sensed reanalysis of atmospheric water fluxes and leaf area index (LAI) data.

418 2.5.2 Validation metrics

419 ~~Except for inventory biomass a~~All statistical evaluations of model results were based on 1) Pearson Correlation and 2)
420 normalized mean squared error (NME; Kelley *et al.*, 2013). NME is calculated as:

$$421 \quad NME = \frac{\sum_{i=1}^N |y_i - x_i|}{\sum_{i=1}^N |x_i - \bar{x}|} \quad \text{Eq.}$$

422 (91)

423 where y_i is the simulated and x_i the reference value in the grid cell or time step i . \bar{x} is the mean reference value. NME takes
424 the value 0 at perfect agreement, 1 when the model performs as well as the reference mean and values > 2 indicate complete
425 disagreement.

426 2.5.3 Maximum cumulative water deficit as indicator of seasonal water stress

427 To analyse and explain the geographical pattern of rooting depth, ET and productivity we use the maximum cumulative
428 water deficit (MCWD) as an independent indicator of potential seasonal water demand of vegetation. MCWD is a widely
429 used indicator for seasonal water stress of tropical and sub-tropical forests in South America (Aragão *et al.*, 2007; Lewis *et*
430 *al.*, 2011; Malhi *et al.*, 2009). MCWD captures the seasonal difference of ET and precipitation in a cumulative way and
431 therefore comprises dry season strength and duration. Here we calculate MCWD on a monthly basis. Therefore, we first
432 calculate the cumulative water deficit CWD_n of each month n as:

$$433 \quad CWD_n = CWD_{n-1} - PET_n + P_n \quad \text{Eq.}$$

434 (102)

435 where PET is the potential monthly ET and P the monthly sum of precipitation. CWD is constrained to values ≤ 0 and is set
436 to 0 at the end of each hydrological year, here the last day of September, as in Lewis *et al.* (2011). We use P from climate
437 input used for model forcing (Sect. 2.3.1) and PET as it is simulated by LPJmL4.0 (Schaphoff *et al.*, 2018) which is only
438 dependent on net surface radiation and air temperature, therefore remaining an explanatory variable independent of
439 vegetation dynamics. We chose this PET instead of using the commonly used constant ET of 100 mm/month to calculate
440 CWD (Aragão *et al.*, 2007; Lewis *et al.*, 2011; Malhi *et al.*, 2009), because in this way, the CWD better corresponds to the
441 actual climatological conditions in the different LPJmL model versions used in this study (Sect. 2.4). MCWD is then
442 calculated as:

$$443 \quad MCWD_y = \min(CWD_{October,y-1}, \dots, CWD_{September,y}) \quad \text{Eq. (113)}$$

444

445 where y indicates the calendrical year.

446 3 Results

447 3.1 ~~Local and r~~Regional pattern of tree rooting strategies

448 In LPJmL4.0-VR the contribution of each tree rooting strategy to the overall net primary productivity (NPP) appears highly
449 dependent on local environmental conditions. ~~Comparisons at the local scale show that While shallow rooted (deep rooted)~~
450 ~~sub-PFTs contribute more to the overall NPP under generally wetter (drier) and less (more) seasonal climate conditions at~~
451 ~~the local scale, deep rooted sub-PFTs do so under drier and more seasonal climate (Fig. 4). At the Fluxnet site MAN-K34,~~
452 ~~which exhibits a mean annual precipitation (MAP) of 2609 mm and a mean MCWD of 222 mm under CRU climate input~~

453 (~~2001-2010~~), the sub-PFT with a maximum rooting depth (D_{95_max}) of 0.5 m contributes most to overall NPP and the whole
454 distribution of NPP weighted D_{95_max} classes shows a mean of 1.52 m (Fig. 5a). At the Fluxnet site STM K67, which exhibits
455 a lower MAP of 2144 mm and a stronger dry season reflected in a mean MCWD of -465 mm, the NPP weighted distribution
456 of D_{95_max} shows a peak at 10 m and a corresponding mean of 10.26 m (Fig. 4b). Since both sites have a soil depth of 20 m
457 (according to the soil depth input; Sect. 2.3.2, Fig. A1) differences in rooting strategy compositions must emerge from the
458 climatic differences of those sites. It is important to note that D_{95_max} values in Fig. 4 (i.e. the bins on the x axes) do not
459 necessarily reflect the true achieved rooting depth of each sub-PFT, but their maximum value. For reasons of visual clarity
460 for this figure we kept the bins of the x axes as chosen in Table 1.

461 Based on the information of how much NPP each sub-PFT contributes in each grid cell, we derived maps of mean rooting
462 depth over the whole study region for the time span 2001-2010 for each climate input used in this study (Fig. 52). ~~In contrast~~
463 ~~to Fig. 4, we computed~~ Fig. 2 shows the mean of the actually achieved D_{95} of each sub-PFT (evergreen and deciduous
464 combined) weighted by the respective relative NPP contribution of each sub-PFT to total forest NPP (we call $\overline{D_{95}}$,
465 hereafter). Apparently Therefore, the regional pattern of $\overline{D_{95}}$ reflects the effects of climate and soil depth. A general East to
466 West gradient of $\overline{D_{95}}$ over the Amazon region follows climatic gradients of precipitation and MCWD (Fig. A2-A3B1-B2),
467 while soil depth (Fig. A1A3) constrains $\overline{D_{95}}$ especially in the South-Eastern Amazon. In general, areas with higher mean
468 annual rainfall and weaker dry season show lower $\overline{D_{95}}$ and vice versa (please also see Fig. B3 for a detailed exemplary
469 comparison of sub-PFT NPP for 2 grid cells with contrasting climate conditions). This pattern holds true under all climate
470 inputs, with some minor local differences and is in line with an inversely modelled global gridded product of maximum
471 depth of root water uptake (MDRU in Fan et al. 2017). Nevertheless, we find considerable absolute differences between
472 MDRU and $\overline{D_{95}}$ (Fig. A4B4), which can easily emerge from different model settings and assumptions, e.g. related to
473 differences in spatial model resolution, simulated water percolation and underlying vegetation features.

474 Focussing on the climatological clusters (Sect. 2.5.1 and Fig. 93f) under CRU climate input, the western Amazon (EQ W),
475 with a MAP of 2708 mm and mean MCWD of -163 mm, displays an overall mean $\overline{D_{95}}$ of 1.14 m and a maximum of 5.47 m,
476 despite considerably deeper soils present. In this cluster Fan et al. (2017) find a respective mean and maximum MDRU of
477 1.26 and 17.95 m. In the Northern, Western and Southern Amazon clusters (NSA, EQ E, SAMz) with lower MAP of 2299,
478 2190 and 2035 mm and considerably lower MCWD of -488, -438 and -497 mm, respectively, mean $\overline{D_{95}}$ increases to 2.32,
479 3.20 and 2.68 m, respectively (mean MDRU of 1.85, 2.84 and 3.28 m). Here, maximum $\overline{D_{95}}$ values respectively reach 11.97,
480 11.27 and 9.04 m (maximum MDRU of 14.28, 13.47 m and 16.57 m). In the monsoon dominated region (SAMS) displaying
481 the lowest MAP of 1449 mm and MCWD of -649 mm, mean $\overline{D_{95}}$ decreases to 1.37 m (mean MDRU 2.61 m). The maximum
482 $\overline{D_{95}}$ of this region reaches 11.17 m located at the border to SAMz (maximum MDRU 49.37 m).

483 The regional simulation of $\overline{D_{95}}$ now also allows us to generalize which tree rooting strategies occupy which climate space.
484 Using MCWD and MAP to define a climate space we find a clear adjustment of $\overline{D_{95}}$ (Fig. 6B5). A core region with deep-
485 rooted forests (mean $\overline{D_{95}} > 4$ m) is found where MCWD ranges between -1300 and -400 and where MAP is at least 1500 mm
486 (see also maps of MCWD and MAP in Fig. A2B1-3B2). This core region is surrounded by a small band of medium rooting
487 depth forests (mean $\overline{D_{95}} \sim 2-4$ m) forming a crescent shape. Rather shallow-rooted forests (mean $\overline{D_{95}} < 2$ m) are found in
488 increasingly drier climates where MAP is less than 1000 mm and in more seasonal climates where MCWD is below -500
489 mm. Shallow-rooted forests are also simulated in very wet conditions where MCWD is greater than -300 mm and MAP is
490 1200 mm or higher.

491 3.2 Evapotranspiration ~~rates~~ and productivity

492 3.2.1 Local evapotranspiration

493 ~~Differences of intra-annual ET rates between the 3 LPJmL model versions are most pronounced at Fluxnet sites with high~~
494 ~~seasonality of rainfall (Fig. 7b, e, g and Fig. 8b, e, g). Here, variable tree rooting strategies (LPJmL4.0-VR) lead to a major~~
495 ~~improvement in reproducing measured Fluxnet NEE and ET, also expressed in reduced NME and increased r^2 values (Table~~
496 ~~A3-A4). Whereas, constant tree rooting strategies (LPJmL4.0-VR base and LPJmL4.0) simulate decreasing ET and~~
497 ~~increasing NEE during dry seasons at these sites, which is anticorrelated to Fluxnet measurements, variable tree rooting~~
498 ~~strategies (LPJmL4.0-VR) follow the intra-annual Fluxnet signals. Most pronounced improvements are found at STM K67~~
499 ~~and STM K83, where the NME of ET and NEE drop below or close to 1, and where r^2 values considerably increase~~
500 ~~compared to the other 2 model versions (Table A3-A4). For STM K67, the r^2 of NEE is higher under LPJmL4.0 and~~
501 ~~LPJmL4.0-VR base, but this refers to a significant negative correlation.~~

502 ~~At STM K77 (Fig. 7f) local circumstances show the influence of variable rooting strategies on ET in a different way. This~~
503 ~~former rainforest site was converted to pasture before Eddy covariance measurements began. This local land use at STM~~
504 ~~K77 is not representative for the respective 0.5° grid cell, and thus all 3 LPJmL model versions simulate mainly natural~~
505 ~~vegetation instead of pasture. Therefore, the shallow rooting systems of LPJmL4.0 and LPJmL4.0-VR base show a better~~
506 ~~match to ET measurements at STM K77. The site STM K83 (Fig. 7g) is a selectively logged primary forest site which shares~~
507 ~~the same model grid cell as STM K77 due to their geographical proximity. Again, here only simulations with variable tree~~
508 ~~rooting strategies (LPJmL4.0-VR) reproduce increased ET and decreased NEE during the dry season. At sites with weaker to~~
509 ~~no dry season (Fig. 7c, d, h) differences between model versions become less pronounced, as water availability is more~~
510 ~~stable throughout the year leading to less variable ET.~~

511 3.2.2 Continental Evapotranspiration

512 ~~Results of regional ET are in line with results of site-specific ET.~~ The climatological clusters within the Amazon region
513 which undergo the strongest dry season (EQ E and SAMz) show the largest differences between simulations with variable
514 (LPJmL4.0-VR) and constant tree rooting strategies (LPJmL4.0-VR-base and LPJmL4.0). In those clusters LPJmL4.0-VR
515 shows highest a significant higher agreement with validation data (Fig. 9e3c, d and Table A5B3). Agreement is largest for
516 EQ E where NME and r^2 show values of 0.62 and 0.91, respectively, whereas constant rooting systems in the other two
517 models lead to values of NME \gg 1.92 and $r^2 \leq$ 0.21 (Table A5B3). In NSA and EQ W model differences are less
518 pronounced as annual precipitation deficits are lower and deep rooting systems play a lesser role. Still, variable rooting
519 systems lead to noticeably higher agreement in NSA between January and April (Fig. 9a3a), where monthly precipitation is
520 lower compared to the rest of the year. In the monsoon dominated cluster SAMS outside the Amazon region (Fig. 9e3e),
521 model differences are least pronounced, since shallow rooting forests dominate this area in LPJmL4.0-VR (Fig. 52) which
522 are very similar to the forests with constant tree rooting strategies in the other 2 model versions.

523 Results of regional ET are in line with results of site-specific ET. On the local level, variable tree rooting strategies of
524 LPJmL4.0-VR lead to a major improvement in reproducing measured Fluxnet NEE and ET (Appendix B Sect. 1.1 & Fig B6-
525 B7), increasing the confidence of regional modelling results.

526 3.3 Distribution of plant functional types

527 The simulated relative dominance of tropical tree PFTs across the study area differs substantially between model versions
528 (Fig. 104). In simulations with LPJmL4.0, more than half of the grid cells show the evergreen and deciduous PFTs equally
529 dominant (Fig. 10g4g-h). Only in areas outside tropical moist climate regions the model tends towards a dominance of the
530 deciduous PFT, whereas e.g. in the Amazon region, the evergreen and deciduous PFTs co-exist in almost equal abundance.

531 These patterns strongly differ from satellite-derived geographical PFT distributions (Fig. 10a4a-b) and therefore yield in
532 respective comparisons the highest NME values among all models (Table A6B4). In contrast LPJmL4.0-VR and LPJmL4.0-
533 VR-base show clear dominance patterns of both tropical tree PFTs across the study area (Fig. 10e4c-f). Nevertheless,
534 differences between LPJmL4.0-VR and LPJmL4.0-VR-base are quite substantial. In LPJmL4.0-VR-base the tropical
535 evergreen PFT dominates the North-Western Amazon region only, negligibly extending further than the borders of
536 climatological clusters NSA and EQ W combined. Beyond these borders the tropical deciduous PFT dominates (Fig. 10e4e-
537 f). In contrast, in LPJmL4.0-VR (Fig. 10e4c-f) the evergreen tree PFT dominates the entire Amazon region including EQ E
538 and SAMz, and the deciduous PFT is pushed towards drier and more seasonal climate (including parts of SAMS). Therefore,
539 LPJmL4.0-VR yields the lowest NME values in comparison to satellite-derived PFT distributions (Table A6B4).

540 4 Discussion

541 4.1 Climate and soil depth determine dominant tree rooting strategies

542 The geographical patterns of simulated \overline{D}_{95} are very similar under 4 different climate input data sets (Fig. 52). This gives
543 confidence to the general robustness of our results and modelling approach as differences in climate data do not lead to
544 substantially different model behaviour. This is further supported by similar regional rates of ET simulated under the
545 different climate data inputs (Fig. 93).

546 Simulated \overline{D}_{95} (Fig. 52) clearly follows climate gradients and soil depth found in the study region (Fig. A1-A3A3, B2-B3).
547 Here, MAP and MCWD can serve as explanatory variables of simulated \overline{D}_{95} (Fig. 6B5). These findings are in line with the
548 general ecological expectation and former studies that seasonal water depletion of upper soil layers, as a combination of
549 annual precipitation and dry season length and strength, is positively correlated with the rooting depth of tropical evergreen
550 trees (Baker et al., 2009; Ichii et al., 2007; Kleidon and Heimann, 1998, 1999). We also find lower thresholds for MAP and
551 MCWD where \overline{D}_{95} strongly decreases again (Fig. 6B5) which can be explained by different mechanisms leading to a regime
552 shift from the evergreen to the deciduous tree PFT as discussed below (see Sect. 4.2).

553 To evaluate our model results against empirical data, we checked the data availability on maximum rooting depth across
554 South America in the TRY database (Kattge et al., 2020; data downloaded September 2019). As it is also shown in Fan et al.
555 (2017; Fig. 2) we found the number of sites within the TRY data base where maximum rooting depth has been measured in
556 South America to be very low. Moreover, the number of data entries per site appeared very small, where 33 TRY sites
557 falling within our study area showed a mean of ~9 and a median of 6 data entries, while 15 sites showed <=5 data entries.
558 Therefore, we decided to not include site specific comparisons of rooting depth as it is not clear how representative these
559 measurements are for the local forest communities. More research is necessary to increase the number of observation sites
560 and improve the empirical basis of field-based rooting depth to allow for site-specific model evaluation. Nevertheless, as
561 shown in Fan et al. (2017; Fig. 2) measured site-specific maximum rooting depth across the Amazon region expectedly
562 follows the known climatic gradient (Fig. A2B1-A3B2). The same holds true for the inversely modelled MDRU of Fan et al.
563 (2017; we show in Fig. A4B4), which gives confidence to our results.

564 4.2 Rooting depth influences the distribution, dominance and biomass of tropical plant functional types

565 In all 3 model versions used in this study the same land-use is applied (Sect. 2.4), which shapes the geographical extent and
566 maximum dominance of natural vegetation in our results. This is why FPC maps of all model versions show the shape of the
567 Amazon region as a distinct pattern (Fig. 104), even though it is less visible for LPJmL4.0-VR-base and one has to consider
568 both tropical tree PFTs at the same time (Fig. 10e4e-f). Within the Amazon region, LPJmL4.0 simulates a similar dominance
569 of the evergreen and deciduous PFT (Fig. 10g4g-h); which contradicts evaluation data (Fig. 10a4a-b) and indicates a similar
570 performance of the 2 PFTs or missing mechanisms rewarding a better performance over time. We here find that introducing

571 | a performance dependent tree establishment rate (Sect. 2.2 and Appendix A Sect. 2-2-61.6) clearly resolves this issue. This
572 | feature produces clear dominance pattern of either PFT in LPJmL4.0-VR and LPJmL4.0-VR-base. Apparently, by rewarding
573 | better performance, variable tree rooting strategies (LPJmL4.0-VR) become necessary to reproduce the dominance of the
574 | evergreen PFT throughout the Amazon region (Fig. 4e4e-f). To remain superior in drier and more seasonal environments in
575 | the South to South-Eastern Amazon region the evergreen PFT needs to access deep water by adjusting its rooting depth (Fig.
576 | 5-62). Clearly, this adjustment of rooting depth is only possible within a certain climatic envelope. Below certain thresholds
577 | of MAP (around 1000 mm) and MCWD (around -500 mm) mean $\overline{D_{95}}$ decreases again (Fig. 6B5), which coincides with a
578 | transition from the evergreen to the deciduous PFT. Those thresholds are similar to thresholds between evergreen forests and
579 | savanna found by e.g. Malhi *et al.* (2009) at an annual precipitation of 1500 mm and at an MCWD of -300 mm. The
580 | substantially lower MCWD value found in ~~this-our~~ study can be explained by the differences in calculating CWD. While
581 | Malhi *et al.* (2009) assume a constant rate of ET per month of 100 mm, we use the monthly variable PET (Sect. 2.5.3). Since
582 | PET often is significantly higher than 100 mm our monthly CWD and therefore MCWD values are respectively lower.
583 | Similarly to Malhi *et al.* (2009), Staver, Archibald and Levin (2011) find that the climatic thresholds for evergreen forest are
584 | not very distinct and savanna can simultaneously be found in a climatic range around the mean threshold. The authors
585 | ascribe this forest-savanna bi-stability to climate-fire-vegetation feedbacks. Many recent studies investigating potential
586 | forest-savanna bi-stability and tipping points of forests in and around the Amazon region rely solely on such climatic ranges
587 | of tropical biomes (Hirota *et al.*, 2011; Wuyts, Champneys and House, 2017; Zemp *et al.*, 2017; Staal *et al.*, 2018; Ciemer *et*
588 | *al.*, 2019). The results of LPJmL4.0-VR show that knowledge on local tree root adaptations is another important explanatory
589 | variable of vegetation cover reducing the uncertainty and width of anticipated climatic ranges where vegetation cover could
590 | be bi-stable. These findings are supported by a recent study that finds rooting depth more crucial than fire dynamics for
591 | explaining PFT dominance in South America (Langan *et al.*, 2017).

592 | Whether the transition between the evergreen and deciduous tree PFT for the thresholds of MAP and MCWD we find with
593 | LPJmL4.0-VR is mainly caused by (a) environmental filtering (including vegetation-fire feedbacks) of deep tree rooting
594 | strategies, (b) their competitive exclusion by shallow rooted deciduous sub-PFTs together with the tropical herbaceous PFT
595 | (Fig. A6B8), or most probably a combination of both is yet to be determined. Given that we used the most simplistic fire
596 | module of LPJmL (GlobFirm; Thonicke *et al.*, 2001) and current land-use input to allow model evaluation against remotely
597 | sensed data in this study, investigating the natural mechanisms of tropical PFT shifts should be in the focus of further
598 | studies.

599 | Regardless of the mechanisms that eventually lead to a PFT shift, we can state that neither costs for deep root investment nor
600 | a heterogeneous pattern of soil depth across the study region disproves that locally adapted tree rooting depth is key to
601 | explain the current geographical distribution of tropical evergreen forests in South-America. Given the large differences
602 | between LPJmL4.0-VR and LPJmL4.0-VR-base (Fig. 4a) it is clear that in roughly half of the Amazon region the carbon
603 | balance of the evergreen PFT is superior to the deciduous PFT only when investing substantial amounts of carbon into
604 | deeper roots, i.e. belowground biomass (BGB; Fig. A8B9). On the one hand this investment has a direct negative effect on
605 | productivity, because during growth the allocation of assimilated carbon shifts towards respiring belowground biomass
606 | (BGB), while investments into productive AGB (Fig. A7B10) need to be reduced. On the other hand, drier and more
607 | seasonal environments show less cloud cover during the dry season (Nemani *et al.*, 2003), enhancing photosynthesis in this
608 | time of the year which increases productivity as long as water access is assured (Costa *et al.*, 2010; Wu *et al.*, 2016). The
609 | trade-off between AGB and BGB investment most probably leads to a more homogenous AGB pattern across the Amazon
610 | region with similar values over a wide climatic range (compare EQ E and SAMz in Fig. A7eB10c-e).

611 4.3 Diverse tree rooting strategies improve simulated evapotranspiration and productivity

612 LPJmL4.0-VR simulates rates of local ET and NEE which reasonably match respective measurements at different Fluxnet
613 sites throughout the Amazon region (Fig. [7B6-8B7](#)), even though we run the model with regionally gridded instead of locally
614 measured climate data. While potentially lacking information on local short-term weather events, gridded climate input still
615 seems to be sufficient to capture broad seasonal signals for our comparisons on a monthly basis. This increases the
616 confidence in our results also on a regional scale.

617 Across large parts of the Amazon region variable tree rooting strategies decrease the intra-annual variability of ET and
618 maintain high rates of NEE and ET during the dry season in accordance with the intra-annual trends suggested by evaluation
619 data (Fig. [7-93, B6-B7](#)). More than that simulated rates of ET and productivity can peak during the dry season, e.g. in EQ E
620 which has been explained by increased solar radiation during this time of the year (Nemani et al., 2003; da Rocha et al.,
621 2004). Especially, in EQ E and SAMz at least parts of the forest area must have access to sufficient water in the model and in
622 reality (Costa et al., 2010; Wu et al., 2016). Given that LPJmL4.0-VR and LPJmL4.0-VR-base are essentially identical
623 models with the same soil depth input and subsequent hydrology over the whole soil column, their differences in simulated
624 ET and NEE must emerge from their only difference which is the amount of simulated tree rooting strategies. Therefore,
625 local root adaptations in LPJm4.0-VR can be regarded as a buffer against seasonal precipitation deficits by usage of deep
626 water (exemplary shown [in largehigh detail](#) for [the Fluxnet Site](#) STM K67 in Fig. [A9B11](#)).

627 We can here quantify this water access for the first time on the basis of carbon investment and return, and limited by spatial
628 heterogeneous soil depth. ~~Without biophysical limits to rooting depth in the form of local soil depth (e.g. by applying a~~
629 ~~universal soil depth of 20 m) and below-ground carbon investment, seasonally dry climatological clusters would potentially~~
630 ~~shift towards deeper rooted sub-PFT dominance, consequently leading to an overestimation of ET rates. If soil depth was no~~
631 ~~limit to rooting depth throughout the study region, ET rates of seasonally dry climatological clusters would have most likely~~
632 ~~been overestimated. The same holds true if deeper roots would not require additional below ground carbon investment.~~
633 Therefore, we argue that both factors are of great importance to explain regional rates of ET. This also means that forests in
634 the same climatological cluster contribute very differently to the overall ET and therefore to ~~the moisture transport~~ [moisture](#)
635 [recycling](#) across South America. We can here mechanistically explain this coherence as we show for the first time on the
636 regional scale how PFTs with variable tree rooting strategies adjust to local environmental conditions and in return lead to
637 simulated rates of ET very close to validation data (Fig. [7-93, B6](#)). The heterogeneous picture of $\overline{D_{95}}$ we find (Fig. [52](#)) might
638 provide a direct guideline where to put emphasis on forest conservation to maintain continental scale moisture recycling, as
639 $\overline{D_{95}}$ directly scales with rates of ET.

640 Being able to mechanistically reproduce and explain the broad-scale stabilization of water fluxes into the atmosphere has
641 wide implications for DGVM modelling frameworks and simulation of ET as moisture input to the atmosphere in Earth
642 System Models (ESMs). Our approach can help to better quantify the role of forests for local-to-continental scale moisture
643 recycling and to project the fate of forests under future climate and land-use change. The approach presented here is easily
644 applicable for a wide range of DGVMs and ESMs which simulate fine root distribution in a similar way as the LPJmL model
645 family (based on Jackson *et al.*, 1996). A first and easy to implement step for other models could be to prescribe the relative
646 fine root distribution in a spatial explicit way in accordance to $\overline{D_{95}}$ presented in this study.

647 5 Conclusions

648 [In this paper we reconfirm the hypotheses that climate and soil depth determine dominant tree rooting strategies \(hypothesis](#)
649 [I\), tree rooting depth is key to explain the distribution and dominance \(hypothesis II\) as well as, evapotranspiration and](#)
650 [productivity rates of tropical evergreen forests in South America \(hypothesis III\), even when the competition of tree rooting](#)
651 [strategies and carbon investment into gradually growing roots are considered. We here show for the first time that mean tree](#)

652 ~~rooting depth across South America can indeed explain the spatial distribution of tropical evergreen forests and their spatio-~~
653 ~~temporal pattern of ecosystem fluxes (ET and NEE) even when the competition of tree rooting strategies, carbon investment~~
654 ~~into gradually growing roots, and a spatially explicit soil depth are considered.~~ In fact our findings suggest that roughly half
655 of the evergreen forests in the Amazon region depend on investments into rooting systems which go deeper than the standard
656 average PFT parameterization based on literature allows for. Those deep root systems can be regarded as a buffer against
657 seasonal precipitation deficits by usage of deep water and keep rates of ET and productivity at high levels throughout the
658 year.

659 A major advance of the new sub-model version LPJmL4.0-VR is that simulations start with uniform input distributions of
660 tree rooting strategies in each location which shape into a distribution of abundance driven by local environmental filtering
661 and competition. Therefore, these distributions are not a pre-selected input, but an emergent simulation output.

662 The new model features enable to introduce local tree rooting depth as a key explanatory variable in future studies dealing
663 with ~~potential forest cover~~ bi-stability of potential forest cover in tropical regions. Generally, we are convinced that our
664 approach is of high importance to all modelling frameworks of DGVMs and Earth System Models (ESMs) aiming at
665 quantifying continental scale moisture recycling, forest tipping points and resilience. So far, the importance of local-scale
666 tree root adaptations for regional-scale ecosystem functions ~~shows that this~~ underlines the need to protect this potential
667 ~~treasure~~ below-ground functional diversity must be protected not only in the scope of future global change.

668 **6 Code availability**

669 In case of manuscript acceptance all model code and post-processing scripts will be made available. The first author of this
670 manuscript is also willing to share all information with all reviewers upon request.

671 **7 Data availability**

672 In case of manuscript acceptance all simulation data will be made available. The first author of this manuscript is also willing
673 to share all information with all reviewers upon request.

674 **8 Author contribution**

675 All authors helped in conceptualizing the model. BS and WvB developed the model code. BS, WvB, MD, AS, RR, FL, MB,
676 SB, MH, RO, KT conceived the simulation experiments and BS carried them out. BS, MD, AS, RR and JH analysed model
677 output data. BS prepared the manuscript with contributions from all co-authors.

678 **9 Competing interests**

679 The authors declare that they have no conflict of interest.

680 **10 Acknowledgements**

681 BS and KT acknowledge funding from the BMBF- and Belmont Forum-funded project “CLIMAX: Climate services through
682 knowledge co-production: A Euro-South American initiative for strengthening societal adaptation response to extreme
683 events”, FKZ 01LP1610A. MD is funded by the DFG/FAPESP within the IRTG 1740/TRP 2015/50122-0. MH is supported
684 by a grant from Instituto Serrapilheira/Serra 1709-18983. A. Sörensson and R. Ruscica acknowledge support from PICT-
685 2018-02511 (ANPCyT, Argentina). This work used eddy covariance data acquired and shared by the FLUXNET

686 community, including these networks: AmeriFlux, AfriFlux, AsiaFlux, CarboAfrica, CarboEuropeIP, CarboItaly,
687 CarboMont, ChinaFlux, Fluxnet-Canada, GreenGrass, ICOS, KoFlux, LBA, NECC, OzFlux-TERN, TCOS-Siberia, and
688 USCCC. The ERA-Interim reanalysis data are provided by ECMWF and processed by LSCE. The FLUXNET eddy
689 covariance data processing and harmonization was carried out by the European Fluxes Database Cluster, AmeriFlux
690 Management Project, and Fluxdata project of FLUXNET, with the support of CDIAC and ICOS Ecosystem Thematic
691 Center, and the OzFlux, ChinaFlux and AsiaFlux offices.

692 **11 References**

- 693 Allen, C. D., Breshears, D. D. and McDowell, N. G.: On underestimation of global vulnerability to tree mortality and forest
694 die-off from hotter drought in the Anthropocene, *Ecosphere*, 6(8), 1–55, doi:10.1890/ES15-00203.1, 2015.
- 695 Aragão, L. E. O. C., Malhi, Y., Roman-Cuesta, R. M., Saatchi, S., Anderson, L. O. and Shimabukuro, Y. E.: Spatial patterns
696 and fire response of recent Amazonian droughts, *Geophys. Res. Lett.*, 34(7), 1–5, doi:10.1029/2006GL028946, 2007.
- 697 Arnold, J. G., Williams, J. R., Nicks, A. D. and Sammons, N. B.: SWRRB; a basin scale simulation model for soil and water
698 resources management., SWRRB; a basin scale Simul. Model soil water Resour. Manag., 1990.
- 699 Arora, V. K. and Boer, G. J.: A Representation of Variable Root Distribution in Dynamic Vegetation Models, *Earth Interact.*,
700 7(6), 1–19, doi:10.1175/1087-3562(2003)007<0001:arovrd>2.0.co;2, 2003.
- 701 Avitabile, V., Herold, M., Heuvelink, G. B. M., Lewis, S. L., Phillips, O. L., Asner, G. P., Armston, J., Ashton, P. S., Banin,
702 L., Bayol, N., Berry, N. J., Boeckx, P., de Jong, B. H. J., Devries, B., Girardin, C. A. J., Kearsley, E., Lindsell, J. A., Lopez-
703 Gonzalez, G., Lucas, R., Malhi, Y., Morel, A., Mitchard, E. T. A., Nagy, L., Qie, L., Quinones, M. J., Ryan, C. M., Ferry, S.
704 J. W., Sunderland, T., Laurin, G. V., Gatti, R. C., Valentini, R., Verbeek, H., Wijaya, A. and Willcock, S.: An integrated
705 pan-tropical biomass map using multiple reference datasets, *Glob. Chang. Biol.*, 22(4), 1406–1420, doi:10.1111/gcb.13139,
706 2016.
- 707 Baker, I. T., Prihodko, L., Denning, A. S., Goulden, M., Miller, S. and Da Rocha, H. R.: Seasonal drought stress in the
708 amazon: Reconciling models and observations, *J. Geophys. Res. Biogeosciences*, 114(1), 1–10, doi:10.1029/2007JG000644,
709 2008.
- 710 Baker, I. T., Prihodko, L., Denning, A. S., Goulden, M., Miller, S. and Da Rocha, H. R.: Seasonal drought stress in the
711 amazon: Reconciling models and observations, *J. Geophys. Res. Biogeosciences*, 114(1), 1–10, doi:10.1029/2007JG000644,
712 2009.
- 713 Balsamo, G., Viterbo, P., Beijaars, A., van den Hurk, B., Hirschi, M., Betts, A. K. and Scipal, K.: A revised hydrology for
714 the ECMWF model: Verification from field site to terrestrial water storage and impact in the integrated forecast system, *J.*
715 *Hydrometeorol.*, 10(3), 623–643, doi:10.1175/2008JHM1068.1, 2009.
- 716 Balsamo, G., Albergel, C., Beijaars, A., Bousssetta, S., Brun, E., Cloke, H., Dee, D., Dutra, E., Munõz-Sabater, J.,
717 Pappenberger, F., De Rosnay, P., Stockdale, T. and Vitart, F.: ERA-Interim/Land: A global land surface reanalysis data set,
718 *Hydrol. Earth Syst. Sci.*, 19(1), 389–407, doi:10.5194/hess-19-389-2015, 2015.
- 719 Baudena, M., Dekker, S. C., van Bodegom, P. M., Cuesta, B., Higgins, S. I., Lehsten, V., Reick, C. H., Rietkerk, M.,
720 Scheiter, S., Yin, Z., Zavala, M. A. and Brovkin, V.: Forests, savannas and grasslands: bridging the knowledge gap between
721 ecology and Dynamic Global Vegetation Models, *Biogeosciences Discuss.*, 11(6), 9471–9510, doi:10.5194/bgd-11-9471-
722 2014, 2014.
- 723 Beck, H. E., Van Dijk, A. I. J. M., Levizzani, V., Schellekens, J., Miralles, D. G., Martens, B. and De Roo, A.: MSWEP: 3-
724 hourly 0.25° global gridded precipitation (1979-2015) by merging gauge, satellite, and reanalysis data, *Hydrol. Earth Syst.*
725 *Sci.*, 21(1), 589–615, doi:10.5194/hess-21-589-2017, 2017.
- 726 Becker, A., Finger, P., Meyer-Christoffer, A., Rudolf, B., Schamm, K., Schneider, U. and Ziese, M.: A description of the

727 global land-surface precipitation data products of the Global Precipitation Climatology Centre with sample applications
728 including centennial (trend) analysis from 1901-present, *Earth Syst. Sci. Data*, 5(1), 71–99, doi:10.5194/essd-5-71-2013,
729 2013.

730 Best, M. J., Pryor, M., Clark, D. B., Rooney, G. G., Essery, R. . L. H., Ménard, C. B., Edwards, J. M., Hendry, M. A.,
731 Porson, A., Gedney, N., Mercado, L. M., Sitch, S., Blyth, E., Boucher, O., Cox, P. M., Grimmond, C. S. B. and Harding, R.
732 J.: The Joint UK Land Environment Simulator (JULES), model description – Part 1: Energy and water fluxes, *Geosci. Model*
733 *Dev.*, 4(3), 677–699, doi:10.5194/gmd-4-677-2011, 2011.

734 Bonal, D., Bosc, A., Ponton, S., Goret, J., Burban, B., Gross, P., Bonnefonds, J. M., Elbers, J. A., Longdoz, B., Epron, D.,
735 Guehl, J. and Granier, A.: Impact of severe dry season on net ecosystem exchange in the Neotropical rainforest of French
736 Guiana, , 14(8), 1917–1933 [online] Available from: <https://edepot.wur.nl/1900>, 2008.

737 Brum, M., Vadeboncoeur, M. A., Ivanov, V., Asbjornsen, H., Saleska, S., Alves, L. F., Penha, D., Dias, J. D., Aragão, L. E.
738 O. C., Barros, F., Bittencourt, P., Pereira, L. and Oliveira, R. S.: Hydrological niche segregation defines forest structure and
739 drought tolerance strategies in a seasonal Amazon forest, *J. Ecol.*, 107(1), 318–333, doi:10.1111/1365-2745.13022, 2019.

740 Brunner, I., Herzog, C., Dawes, M. A., Arend, M. and Sperisen, C.: How tree roots respond to drought, *Front. Plant Sci.*,
741 6(JULY), 1–16, doi:10.3389/fpls.2015.00547, 2015.

742 Canadell, J., Jackson, R. B., Ehleringer, J. R., Mooney, H. A., Sala, O. E. and Schulze, E.-D.: Max rooting depth of
743 vegetation types at the global scale, *Oecologia*, 108, 583–595, doi:10.1007/s10705-016-9812-z, 1996.

744 Carvalhais, N., Forkel, M., Khomik, M., Bellarby, J., Jung, M., Migliavacca, M., Saatchi, S., Santoro, M., Thurner, M. and
745 Weber, U.: Global covariation of carbon turnover times with climate in terrestrial ecosystems, *Nature*, 514(7521), 213–217,
746 2014.

747 Ciemer, C., Boers, N., Hirota, M., Kurths, J., Müller-Hansen, F., Oliveira, R. S. and Winkelmann, R.: Higher resilience to
748 climatic disturbances in tropical vegetation exposed to more variable rainfall, *Nat. Geosci.*, 12(March), doi:10.1038/s41561-
749 019-0312-z, 2019.

750 Cosby, B. J., Hornberger, G. M., Clapp, R. B. and Ginn, T.: A statistical exploration of the relationships of soil moisture
751 characteristics to the physical properties of soils, *Water Resour. Res.*, 20(6), 682–690, 1984.

752 Costa, M. H., Biajoli, M. C., Sanches, L., Malhado, A. C. M., Hutyrá, L. R., Da Rocha, H. R., Aguiar, R. G. and De Araújo,
753 A. C.: Atmospheric versus vegetation controls of Amazonian tropical rain forest evapotranspiration: Are the wet and
754 seasonally dry rain forests any different?, *J. Geophys. Res. Biogeosciences*, 115(4), 1–9, doi:10.1029/2009JG001179, 2010.

755 Dee, D. P., Uppala, S. M., Simmons, A. J., Berrisford, P., Poli, P., Kobayashi, S., Andrae, U., Balmaseda, M. A., Balsamo,
756 G., Bauer, P., Bechtold, P., Beljaars, A. C. M., van de Berg, L., Bidlot, J., Bormann, N., Delsol, C., Dragani, R., Fuentes, M.,
757 Geer, A. J., Haimberger, L., Healy, S. B., Hersbach, H., Hólm, E. V., Isaksen, L., Kållberg, P., Köhler, M., Matricardi, M.,
758 McNally, A. P., Monge-Sanz, B. M., Morcrette, J. J., Park, B. K., Peubey, C., de Rosnay, P., Tavolato, C., Thépaut, J. N. and
759 Vitart, F.: The ERA-Interim reanalysis: Configuration and performance of the data assimilation system, *Q. J. R. Meteorol.*
760 *Soc.*, 137(656), 553–597, doi:10.1002/qj.828, 2011.

761 Ek, M. B., Mitchell, K. E., Lin, Y., Rogers, E., Grunmann, P., Koren, V., Gayno, G. and Tarpley, J. D.: Implementation of
762 Noah land surface model advances in the National Centers for Environmental Prediction operational mesoscale Eta model, *J.*
763 *Geophys. Res. D Atmos.*, 108(22), 1–16, doi:10.1029/2002jd003296, 2003.

764 Eshel, A. and Grünzweig, J. M.: Root-shoot allometry of tropical forest trees determined in a large-scale aeroponic system,
765 *Ann. Bot.*, 112(2), 291–296, doi:10.1093/aob/mcs275, 2013.

766 Fan, Y., Miguez-Macho, G., Jobbágy, E. G., Jackson, R. B. and Otero-Casal, C.: Hydrologic regulation of plant rooting
767 depth., *Proc. Natl. Acad. Sci. U. S. A.*, 114(40), 10572–10577, doi:10.1073/pnas.1712381114, 2017.

768 Fearnside, P. M.: Brazil’s Amazonian forest carbon: the key to Southern Amazonia’s significance for global climate, *Reg.*
769 *Environ. Chang.*, 18(1), 47–61, doi:10.1007/s10113-016-1007-2, 2016.

770 Forkel, M., Carvalhais, N., Schaphoff, S., Bloh, W. V., Migliavacca, M., Thurner, M. and Thonicke, K.: Identifying
771 environmental controls on vegetation greenness phenology through model-data integration, *Biogeosciences*, 11(23), 7025–
772 7050, doi:10.5194/bg-11-7025-2014, 2014.

773 Guimberteau, M., Zhu, D., Maignan, F., Huang, Y., Yue, C., Dantec-Nédélec, S., Ottlé, C., Jornet-Puig, A., Bastos, A.,
774 Laurent, P., Goll, D., Bowering, S., Chang, J., Guenet, B., Tifafi, M., Peng, S., Krinner, G., Ducharne, A., Wang, F., Wang,
775 T., Wang, X., Wang, Y., Yin, Z., Lauerwald, R., Joetzer, E., Qiu, C., Kim, H. and Ciais, P.: ORCHIDEE-MICT (revision
776 4126), a land surface model for the high-latitudes: model description and validation, *Geosci. Model Dev. Discuss.*, (June), 1–
777 65, doi:10.5194/gmd-2017-122, 2017.

778 Harris, I., Jones, P. D., Osborn, T. J. and Lister, D. H.: Updated high-resolution grids of monthly climatic observations - the
779 CRU TS3.10 Dataset, *Int. J. Climatol.*, 34(3), 623–642, doi:10.1002/joc.3711, 2014.

780 Hijmans, R. J. and van Etten, J.: raster: Geographic data analysis and modeling, R Packag. version, 2(8), 2016.

781 Hirota, M., Holmgren, M., Van New, E. H. and Scheffer, M.: Global Resilience of Tropical Forest, *Science* (80-.),
782 334(October), 232–235, doi:10.1126/science.1210657, 2011.

783 Huang, S., Titus, S. J. and Wiens, D. P.: Comparison of nonlinear height–diameter functions for major Alberta tree species,
784 *Can. J. For. Res.*, 22(9), 1297–1304, 1992.

785 Huntingford, C., Zelazowski, P., Galbraith, D., Mercado, L. M., Sitch, S., Fisher, R., Lomas, M., Walker, A. P., Jones, C. D.,
786 Booth, B. B. B., Malhi, Y., Hemming, D., Kay, G., Good, P., Lewis, S. L., Phillips, O. L., Atkin, O. K., Lloyd, J., Gloor, E.,
787 Zaragoza-Castells, J., Meir, P., Betts, R., Harris, P. P., Nobre, C., Marengo, J. and Cox, P. M.: Simulated resilience of
788 tropical rainforests to CO₂-induced climate change, *Nat. Geosci.*, 6(4), 268–273, doi:10.1038/ngeo1741, 2013.

789 Ichii, K., Hashimoto, H., White, M. A., Potter, C., Hutrya, L. R., Huete, A. R., Myneni, R. B. and Nemani, R. R.:
790 Constraining rooting depths in tropical rainforests using satellite data and ecosystem modeling for accurate simulation of
791 gross primary production seasonality, *Glob. Chang. Biol.*, 13(1), 67–77, doi:10.1111/j.1365-2486.2006.01277.x, 2007.

792 Jackson, R. B., Canadell, J., Ehleringer, J., Mooney, H., Sala, O. and Schulze, E.: A global analysis of root distributions for
793 terrestrial biomes, *Oecologia*, 108, 389–411, 1996.

794 Jenik, J.: Roots and root systems in tropical trees, *Trop. trees as living Syst.*, 323, 2010.

795 Jobbágy, E. G. and Jackson, R. B.: the Vertical Distribution of Soil Organic Carbon and Its Relation To Climate and
796 Vegetation, *Ecol. Appl.*, 10(2), 423–436, doi:10.1890/1051-0761(2000)010[0423:TVDOSO]2.0.CO;2, 2000.

797 Johnson, D. M., Domec, J. C., Carter Berry, Z., Schwantes, A. M., McCulloh, K. A., Woodruff, D. R., Wayne Polley, H.,
798 Wortemann, R., Swenson, J. J., Scott Mackay, D., McDowell, N. G. and Jackson, R. B.: Co-occurring woody species have
799 diverse hydraulic strategies and mortality rates during an extreme drought, *Plant Cell Environ.*, 41(3), 576–588,
800 doi:10.1111/pce.13121, 2018.

801 Kattge, J., Bönsch, G., Díaz, S., Lavorel, S., Prentice, I. C., Leadley, P., Tautenhahn, S., Werner, G. D. A., Aakala, T. and
802 Abedi, M.: TRY plant trait database–enhanced coverage and open access, *Glob. Chang. Biol.*, 2020.

803 Kelley, D. I., Prentice, I. C., Harrison, S. P., Wang, H., Simard, M., Fisher, J. B. and Willis, K. O.: A comprehensive
804 benchmarking system for evaluating global vegetation models, *Biogeosciences*, 10(5), 3313–3340, doi:10.5194/bg-10-3313-
805 2013, 2013.

806 Kim, H., Watanabe, E.-C., Chang, K., Yoshimura, Y., Hirabayashi, J., Famiglietti, T. and Oki, T.: Century long observation
807 constrained global dynamic downscaling and hydrologic implication, n.d.

808 Kim, Y., Knox, R. G., Longo, M., Medvigy, D., Hutrya, L. R., Pyle, E. H., Wofsy, S. C., Bras, R. L. and Moorcroft, P. R.:
809 Seasonal carbon dynamics and water fluxes in an Amazon rainforest, *Glob. Chang. Biol.*, 18(4), 1322–1334,
810 doi:10.1111/j.1365-2486.2011.02629.x, 2012.

811 Kleidon, A. and Heimann, M.: A method of determining rooting depth from a terrestrial biosphere model and its impacts on
812 the global water and carbon cycle, *Glob. Chang. Biol.*, 4(3), 275–286, doi:10.1046/j.1365-2486.1998.00152.x, 1998.

813 Kleidon, A. and Heimann, M.: Deep-rooted vegetation, Amazonian deforestation, and climate: Results from a modelling
814 study, *Glob. Ecol. Biogeogr.*, 8(5), 397–405, doi:10.1046/j.1365-2699.1999.00150.x, 1999.

815 Kleidon, A. and Heimann, M.: Assessing the role of deep rooted vegetation in the climate system with model simulations:
816 Mechanism, comparison to observations and implications for Amazonian deforestation, *Clim. Dyn.*, 16(2–3), 183–199,
817 doi:10.1007/s003820050012, 2000.

818 Krysanova, V., Müller-Wohlfeil, D.-I. and Becker, A.: Development and test of a spatially distributed hydrological/water
819 quality model for mesoscale watersheds, *Ecol. Modell.*, 106(2–3), 261–289, 1998.

820 Langan, L., Higgins, S. I. and Scheiter, S.: Climate-biomes, pedo-biomes or pyro-biomes: which world view explains the
821 tropical forest–savanna boundary in South America?, *J. Biogeogr.*, 44(10), 2319–2330, doi:10.1111/jbi.13018, 2017.

822 Lawrence, D. M., Oleson, K. W., Flanner, M. G., Thornton, P. E., Swenson, S. C., Lawrence, P. J., Zeng, X., Yang, Z.-L.,
823 Levis, S., Sakaguchi, K., Bonan, G. B. and Slater, A. G.: Parameterization improvements and functional and structural
824 advances in Version 4 of the Community Land Model, *J. Adv. Model. Earth Syst.*, 3(3), 1–27, doi:10.1029/2011ms000045,
825 2011.

826 Lee, J. E., Oliveira, R. S., Dawson, T. E. and Fung, I.: Root functioning modifies seasonal climate, *Proc. Natl. Acad. Sci. U.*
827 *S. A.*, 102(49), 17576–17581, doi:10.1073/pnas.0508785102, 2005.

828 Leuschner, C., Moser, G., Bertsch, C., Röderstein, M. and Hertel, D.: Large altitudinal increase in tree root/shoot ratio in
829 tropical mountain forests of Ecuador, *Basic Appl. Ecol.*, 8(3), 219–230, 2007.

830 Lewis, S. L., Brando, P. M., Phillips, O. L., Van Der Heijden, G. M. F. and Nepstad, D.: The 2010 Amazon drought, *Science*
831 (80-.), 331(6017), 554, doi:10.1126/science.1200807, 2011.

832 Li, W., Houghton, R. A., Bontemps, S., MacBean, N., Lamarche, C., Ciais, P., Peng, S. and Defourny, P.: Gross and net land
833 cover changes in the main plant functional types derived from the annual ESA CCI land cover maps (1992–2015), *Earth*
834 *Syst. Sci. Data*, 10(1), 219–234, doi:10.5194/essd-10-219-2018, 2018.

835 Liu, L., Peng, S., AghaKouchak, A., Huang, Y., Li, Y., Qin, D., Xie, A. and Li, S.: Broad Consistency Between Satellite and
836 Vegetation Model Estimates of Net Primary Productivity Across Global and Regional Scales, *J. Geophys. Res.*
837 *Biogeosciences*, 123(12), 3603–3616, doi:10.1029/2018JG004760, 2018.

838 Liu, Y., Piao, S., Lian, X., Ciais, P. and Smith, W. K.: Seasonal responses of terrestrial carbon cycle to climate variations in
839 CMIP5 models: Evaluation and projection, *J. Clim.*, 30(16), 6481–6503, doi:10.1175/JCLI-D-16-0555.1, 2017.

840 Liu, Y. Y., Dorigo, W. A., Parinussa, R. M., De Jeu, R. A. M., Wagner, W., McCabe, M. F., Evans, J. P. and Van Dijk, A. I.
841 J. M.: Trend-preserving blending of passive and active microwave soil moisture retrievals, *Remote Sens. Environ.*,
842 123(October 2006), 280–297, doi:10.1016/j.rse.2012.03.014, 2012.

843 Liu, Y. Y., van Dijk, A. I. J. M., McCabe, M. F., Evans, J. P. and de Jeu, R. A. M.: Global vegetation biomass change (1988-
844 2008) and attribution to environmental and human drivers, *Glob. Ecol. Biogeogr.*, 22(6), 692–705, doi:10.1111/geb.12024,
845 2013.

846 Malhi, Y., Aragao, L. E. O. C., Galbraith, D., Huntingford, C., Fisher, R., Zelazowski, P., Sitch, S., McSweeney, C. and
847 Meir, P.: Exploring the likelihood and mechanism of a climate-change-induced dieback of the Amazon rainforest, *Proc. Natl.*
848 *Acad. Sci.*, 106(49), 20610–20615, doi:10.1073/pnas.0804619106, 2009.

849 Markewitz, D., Devine, S., Davidson, E. A., Brando, P. and Nepstad, D. C.: Soil moisture depletion under simulated drought
850 in the Amazon: Impacts on deep root uptake, *New Phytol.*, 187(3), 592–607, doi:10.1111/j.1469-8137.2010.03391.x, 2010.

851 Martens, B., Miralles, D. G., Lievens, H., Van Der Schalie, R., De Jeu, R. A. M., Fernández-Prieto, D., Beck, H. E., Dorigo,
852 W. A. and Verhoest, N. E. C.: GLEAM v3: Satellite-based land evaporation and root-zone soil moisture, *Geosci. Model*
853 *Dev.*, 10(5), 1903–1925, doi:10.5194/gmd-10-1903-2017, 2017.

854 Masson, V., Champeaux, J. L., Chauvin, F., Meriguet, C. and Lacaze, R.: A global database of land surface parameters at 1-
855 km resolution in meteorological and climate models, *J. Clim.*, 16(9), 1261–1282, doi:10.1175/1520-0442-16.9.1261, 2003.

856 Miralles, D. G., Holmes, T. R. H., De Jeu, R. A. M., Gash, J. H., Meesters, A. G. C. A. and Dolman, A. J.: Global land-
857 surface evaporation estimated from satellite-based observations, *Hydrol. Earth Syst. Sci.*, 15(2), 453–469, doi:10.5194/hess-
858 15-453-2011, 2011.

859 Mokany, K., Raison, R. J. and Prokushkin, A. S.: Critical analysis of root: Shoot ratios in terrestrial biomes, *Glob. Chang.*
860 *Biol.*, 12(1), 84–96, doi:10.1111/j.1365-2486.2005.001043.x, 2006.

861 Nachtergaele, F. van, Velthuizen, H., Verelst, L., Batjes, N., Dijkshoorn, K. van Engelen, V., Fischer, G., Jones, A.,
862 Montanarella, L. and Petri, M.: Harmonized world soil database, Food and Agriculture Organization of the United Nations,
863 [online] Available from: [http://www.fao.org/soils-portal/soil-survey/soil-maps-and-databases/harmonized-world-soil-](http://www.fao.org/soils-portal/soil-survey/soil-maps-and-databases/harmonized-world-soil-database-v12/en/)
864 [database-v12/en/](http://www.fao.org/soils-portal/soil-survey/soil-maps-and-databases/harmonized-world-soil-database-v12/en/), 2009.

865 Nemani, R. R., Keeling, C. D., Hashimoto, H., Jolly, W. M., Piper, S. C., Tucker, C. J., Myneni, R. B. and Running, S. W.:
866 Climate-driven increases in global terrestrial net primary production from 1982 to 1999, *Science* (80-.), 300(5625), 1560–
867 1563, doi:10.1126/science.1082750, 2003.

868 Nepstad, D. C., de Carvalho, C. R., Davidson, E. A., Jipp, P. H., Lefebvre, P. A., Negreiros, G. H., da Silva, E. D., Stone, T.
869 A., Trumbore, S. E. and Vieira, S.: The role of deep roots in the hydrological and carbon cycles of Amazonian forests and
870 pastures, *Nature*, 372(6507), 666–669, doi:10.1038/372666a0, 1994.

871 New, M., Hulme, M. and Jones, P.: Representing twentieth century space-time climate variability. Part II: development of a
872 1901-1996 monthly grids of terrestrial surface climate, *J. Clim.*, 13, 2217–2238, 2000.

873 Nikolova, P. S., Zang, C. and Pretzsch, H.: Combining tree-ring analyses on stems and coarse roots to study the growth
874 dynamics of forest trees: A case study on Norway spruce (*Picea abies* [L.] H. Karst), *Trees - Struct. Funct.*, 25(5), 859–872,
875 doi:10.1007/s00468-011-0561-y, 2011.

876 Ostle, N. J., Smith, P., Fisher, R., Ian Woodward, F., Fisher, J. B., Smith, J. U., Galbraith, D., Levy, P., Meir, P., McNamara,
877 N. P. and Bardgett, R. D.: Integrating plant-soil interactions into global carbon cycle models, *J. Ecol.*, 97(5), 851–863,
878 doi:10.1111/j.1365-2745.2009.01547.x, 2009.

879 Pelletier, J. D., Broxton, P. D., Hazenberg, P., Zeng, X., Troch, P. A., Niu, G.-Y., Williams, Z., Brunke, M. A. and Gochis,
880 D.: A gridded global data set of soil, intact regolith, and sedimentary deposit thicknesses for regional and global land surface
881 modeling, *J. Adv. Model. Earth Syst.*, 8, 41–65, doi:10.1002/2017MS001065, 2016.

882 Poorter, H., Niklas, K. J., Reich, P. B., Oleksyn, J., Poot, P. and Mommer, L.: Biomass allocation to leaves, stems and roots:
883 meta-analyses of interspecific variation and environmental control, *New Phytol.*, 193(1), 30–50, 2012.

884 Prentice, I. C., Sykes, M. T. and Cramer, W.: A simulation model for the transient effects of climate change on forest
885 landscapes, *Ecol. Modell.*, 65(1–2), 51–70, 1993.

886 R Core Team: R: A language and environment for statistical computing. R Foundatoin for Statistical Computing, [online]
887 Available from: <https://www.r-project.org/>, 2019.

888 Restrepo-Coupe, N., Levine, N. M., Christoffersen, B. O., Albert, L. P., Wu, J., Costa, M. H., Galbraith, D., Imbuzeiro, H.,
889 Martins, G., da Araujo, A. C., Malhi, Y. S., Zeng, X., Moorcroft, P. and Saleska, S. R.: Do dynamic global vegetation
890 models capture the seasonality of carbon fluxes in the Amazon basin? A data-model intercomparison, *Glob. Chang. Biol.*,
891 23(1), 191–208, doi:10.1111/gcb.13442, 2017.

892 Rodell, M., Houser, P. R., Jambor, U., Gottschalck, J., Mitchell, K., Meng, C.-J., Arsenault, K., Cosgrove, B., Radakovich,
893 J., Bosilovich, M., Entin, J. K., Walker, J. P., Lohmann, D. and Toll, D.: The Global Land Data Assimilation System, *Bull.*
894 *Am. Meteorol. Soc.*, 85(March), 381–394, 2004.

895 Saatchi, S. S., Harris, N. L., Brown, S., Lefsky, M., Mitchard, E. T. A., Salas, W., Zutta, B. R., Buermann, W., Lewis, S. L.,
896 Hagen, S., Petrova, S., White, L., Silman, M. and Morel, A.: Benchmark map of forest carbon stocks in tropical regions
897 across three continents, *Proc. Natl. Acad. Sci.*, 108(24), 9899–9904, doi:10.1073/pnas.1019576108, 2011.

898 Saleska, S. R., Da Rocha, H. R., Huete, A. R., Nobre, A. D., Artaxo, P. E. and Shimabukuro, Y. E.: LBA-ECO CD-32 Flux

899 Tower Network Data Compilation, Brazilian Amazon: 1999-2006, , doi:10.3334/ORNLDAAC/1174, 2013.

900 Schaphoff, S., von Bloh, W., Rammig, A., Thonicke, K., Biemans, H., Forkel, M., Gerten, D., Heinke, J., Jägermeyr, J.,
901 Knauer, J., Langerwisch, F., Lucht, W., Müller, C., Rolinski, S. and Waha, K.: LPJmL4 – a dynamic global vegetation
902 model with managed land – Part 1: Model description, *Geosci. Model Dev.*, 11(4), 1343–1375, doi:10.5194/gmd-11-1343-
903 2018, 2018.

904 Schymanski, S. J., Sivapalan, M., Roderick, M. L., Beringer, J. and Hutley, L. B.: An optimality-based model of the coupled
905 soil moisture and root dynamics, *Hydrol. Earth Syst. Sci.*, 12(3), 913–932, doi:10.5194/hess-12-913-2008, 2008.

906 Sheffield, J., Goteti, G. and Wood, E. F.: Development of a 50-year high-resolution global dataset of meteorological forcings
907 for land surface modeling, *J. Clim.*, 19(13), 3088–3111, doi:10.1175/JCLI3790.1, 2006.

908 Shinozaki, K., Yoda, K. and Kira, T.: A quantitative analysis of plant form - The pipe model theory, *Japanese J. Ecol.*, 14(3),
909 1964.

910 Smith, B., Wärlind, D., Arneth, A., Hickler, T., Leadley, P., Siltberg, J. and Zaehle, S.: Implications of incorporating N
911 cycling and N limitations on primary production in an individual-based dynamic vegetation model, *Biogeosciences*, 11(7),
912 2027–2054, doi:10.5194/bg-11-2027-2014, 2014.

913 Sörensson, A. A. and Ruscica, R. C.: Intercomparison and Uncertainty Assessment of Nine Evapotranspiration Estimates
914 Over South America, *Water Resour. Res.*, 54(4), 2891–2908, doi:10.1002/2017WR021682, 2018.

915 Staal, A., Tuinenburg, O. A., Bosmans, J. H. C., Holmgren, M., Van Nes, E. H., Scheffer, M., Zemp, D. C. and Dekker, S.
916 C.: Forest-rainfall cascades buffer against drought across the Amazon, *Nat. Clim. Chang.*, 8(6), 539–543,
917 doi:10.1038/s41558-018-0177-y, 2018.

918 Stahl, C., Hérault, B., Rossi, V., Burban, B., Bréchet, C. and Bonal, D.: Depth of soil water uptake by tropical rainforest
919 trees during dry periods: Does tree dimension matter?, *Oecologia*, 173(4), 1191–1201, doi:10.1007/s00442-013-2724-6,
920 2013.

921 Staver, A. C., Archibald, S. and Levin, S. A.: The global extent and determinants of savanna and forest as alternative biome
922 states, *Science (80-.)*, 334(6053), 230–232, doi:10.1126/science.1210465, 2011.

923 Tans, P. and Keeling, R.: Trends in Atmospheric Carbon Dioxide, *Natl. Ocean. Atmos. Adm. Earth Syst. Res. Lab.* [online]
924 Available from: <http://www.esrl.noaa.gov/gmd/ccgg/trends>, 2015.

925 Thonicke, K., Venevsky, S., Sitch, S. and Cramer, W.: The role of fire disturbance for global vegetation dynamics: Coupling
926 fire into a dynamic global vegetation model, *Glob. Ecol. Biogeogr.*, 10(6), 661–677, doi:10.1046/j.1466-822X.2001.00175.x,
927 2001.

928 Waring, R. H., Schroeder, P. E. and Oren, R.: Application of the pipe model theory to predict canopy leaf area, *Can. J. For.*
929 *Res.*, 12(3), 556–560, doi:https://doi.org/10.1139/x82-086, 1982.

930 Warren, J. M., Hanson, P. J., Iversen, C. M., Kumar, J., Walker, A. P. and Wullschleger, S. D.: Root structural and
931 functional dynamics in terrestrial biosphere models - evaluation and recommendations, *New Phytol.*, 205(1), 59–78,
932 doi:10.1111/nph.13034, 2015a.

933 Warren, J. M., Hanson, P. J., Iversen, C. M., Kumar, J., Walker, A. P. and Wullschleger, S. D.: Root structural and
934 functional dynamics in terrestrial biosphere models - evaluation and recommendations, *New Phytol.*, 205(1), 59–78,
935 doi:10.1111/nph.13034, 2015b.

936 Weber, U., Jung, M., Reichstein, M., Beer, C., Braakhekke, M. C., Lehsten, V., Ghent, D., Kaduk, J., Viogy, N., Ciais, P.,
937 Gobron, N. and Rödenbeck, C.: The interannual variability of Africa’s ecosystem productivity: A multi-model analysis,
938 *Biogeosciences*, 6(2), 285–295, doi:10.5194/bg-6-285-2009, 2009.

939 Weedon, G. P., Gomes, S., Viterbo, P., Shuttleworth, W. J., Blyth, E., Österle, H., Adam, J. C., Bellouin, N., Boucher, O.
940 and Best, M.: Creation of the WATCH Forcing Data and Its Use to Assess Global and Regional Reference Crop Evaporation
941 over Land during the Twentieth Century, *J. Hydrometeorol.*, 12(5), 823–848, doi:10.1175/2011jhm1369.1, 2011.

942 Weedon, G. P., Balsamo, G., Bellouin, N., Gomes, S., Best, M. J. and Viterbo, P.: Data methodology applied to ERA-
 943 Interim reanalysis data, *Water Resour. Res.*, 50, 7505–7514, doi:10.1002/2014WR015638. Received, 2014.

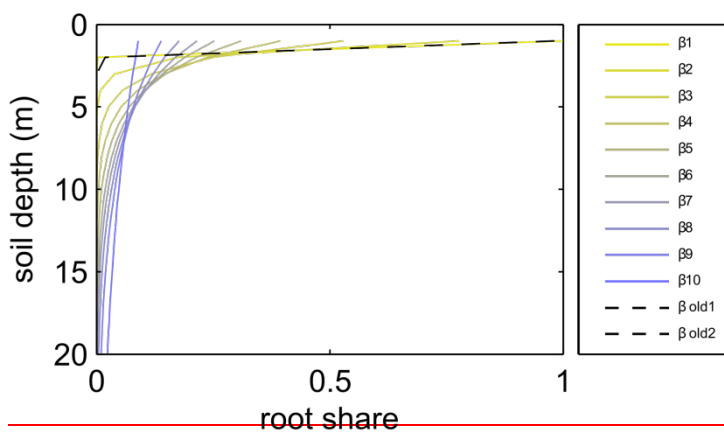
944 Wu, J., Albert, L. P., Lopes, A. P., Restrepo-Coupe, N., Hayek, M., Wiedemann, K. T., Guan, K., Stark, S. C.,
 945 Christoffersen, B., Prohaska, N., Tavares, J. V., Marostica, S., Kobayashi, H., Ferreira, M. L., Campos, K. S., Dda Silva, R.,
 946 Brando, P. M., Dye, D. G., Huxman, T. E., Huete, A. R., Nelson, B. W. and Saleska, S. R.: Leaf development and
 947 demography explain photosynthetic seasonality in Amazon evergreen forests, *Science* (80-.), 351(6276), 972–976,
 948 doi:10.1126/science.aad5068, 2016.

949 Wuyts, B., Champneys, A. R. and House, J. I.: Amazonian forest-savanna bistability and human impact, *Nat. Commun.*,
 950 8(May), 1–11, doi:10.1038/ncomms15519, 2017.

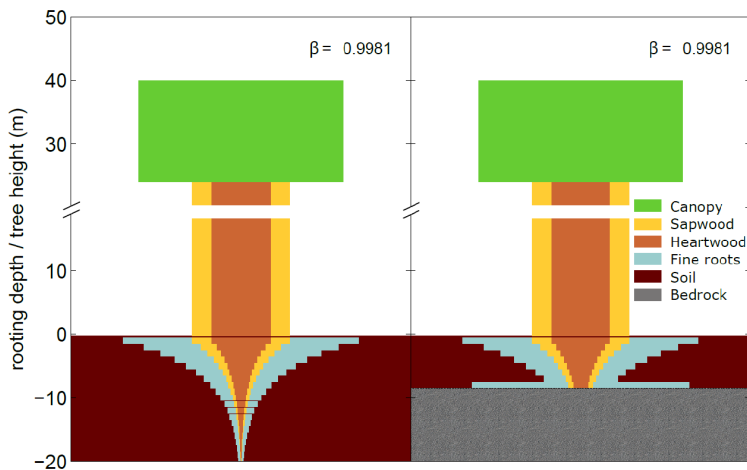
951 Xiao, C. W., Yuste, J. C., Janssens, I. A., Roskams, P., Nachtergale, L., Carrara, A., Sanchez, B. Y. and Ceulemans, R.:
 952 Above- and belowground biomass and net primary production in a 73-year-old Scots pine forest, *Tree Physiol.*, 23(8), 505–
 953 516, doi:10.1093/treephys/23.8.505, 2003.

954 Xiao, X., Hagen, S., Zhang, Q., Keller, M. and Moore, B.: Detecting leaf phenology of seasonally moist tropical forests in
 955 South America with multi-temporal MODIS images, *Remote Sens. Environ.*, 103(4), 465–473,
 956 doi:10.1016/j.rse.2006.04.013, 2006.

957 Zemp, D. C., Schleussner, C. F., Barbosa, H. M. J., Hirota, M., Montade, V., Sampaio, G., Staal, A., Wang-Erlandsson, L.
 958 and Rammig, A.: Self-amplified Amazon forest loss due to vegetation-atmosphere feedbacks, *Nat. Commun.*, 8, 1–10,
 959 doi:10.1038/ncomms14681, 2017.



960 **Figure 1: Relative amount of fine roots in each soil layer for different β -values in LPJmL4.0 and LPJmL4.0-VR. In the legend “ β**
 961 **old1-2” correspond to the β values of the 2 tropical tree PFTs (deciduous and evergreen) simulated in LPJmL4.0. The**
 962 **corresponding graphs lie on top of each other due to marginal differences in their β -values. “ β 1-10” correspond to the 10 β -values**
 963 **used in LPJmL4.0-VR (Table 1) used to create the 10 sub-PFTs of the tropical evergreen and deciduous tree PFTs (Sect. 2.2.3).**
 964 **For LPJmL4.0-VR the fine root distribution at maximum rooting depth is shown. Please note, the first 3 soil layer (as described in**
 965 **2.2.1) in this visualization are treated as 1 layer of 1 m thickness for reasons of visual clarity.**



967

968

969

970

971

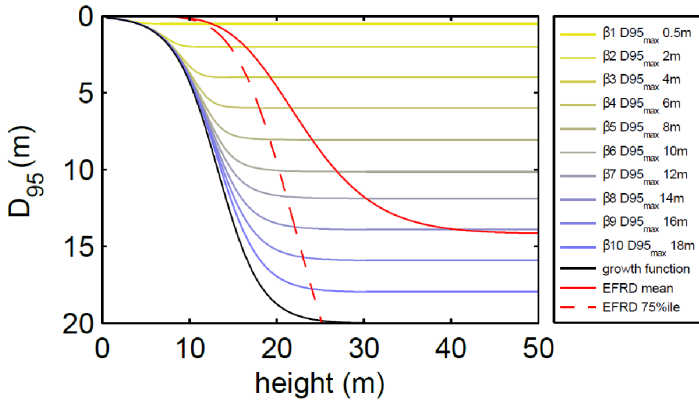
972

973

974

975

Figure 2: Visualization of belowground carbon allocation to different carbon pools of a tree PFT in LPJmL4.0-VR with a height of 40m and a D_{95_max} of 14m (sub-PFT no. 8 in Table 4A2) growing in a grid cell with a soil depth of 20m (left panel) and a soil depth of 7m (right panel). As for stem sapwood, also root sapwood needs to satisfy the pipe model. In the first soil layer root sapwood cross-sectional area is equal to stem sapwood cross-sectional area, as all water taken up by fine roots needs to pass this layer. In each following soil layer the root sapwood cross-sectional area is reduced by the sum of the relative amount of fine roots of all soil layers above, thus adjusting the amount of sapwood needed to satisfy the pipe model. Please also see Supplementary Video 1 for a visualization of root growth and development of belowground carbon pools over time under http://www.pik-potsdam.de/~borissa/LPJmL4_VR/Supplementary_Video_1.pptx.



976

977

978

979

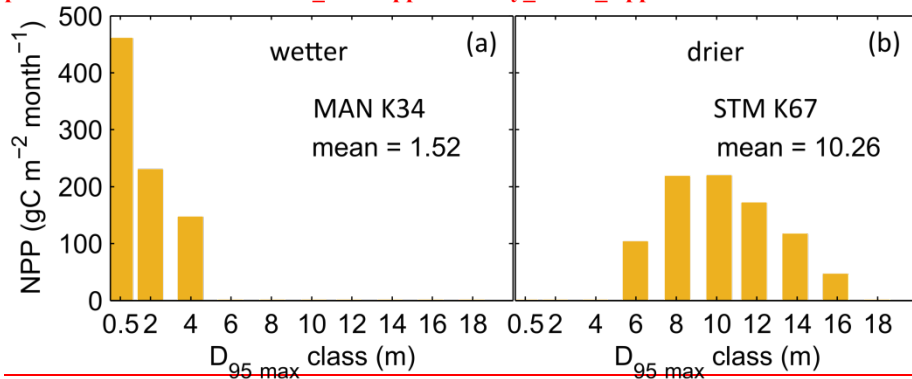
980

981

982

983

Figure 3: Relation between tree height and rooting depth in LPJmL4.0-VR. Black line: Implemented general growth function of rooting depth (Eq. 5). Lines with colour scale from yellow to blue: Growth functions of rooting depth for each of the 10 sub-PFTs (Sect. 2.2.3). Here temporal rooting depth is expressed as D_{95} and eventually reaches D_{95_max} (Eq. 3). Red solid line: Mean effective functional rooting depth over tree height (EFRD) adapted from Brum *et al.* (2019) using Eq. 5. Red dashed line: Respective 75%ile EFRD over tree height adapted from Brum *et al.* (2019). Please also see Supplementary Video 1 for a visualization of root growth and development of belowground carbon pools over time under http://www.pik-potsdam.de/~borissa/LPJmL4_VR/Supplementary_Video_1.pptx.



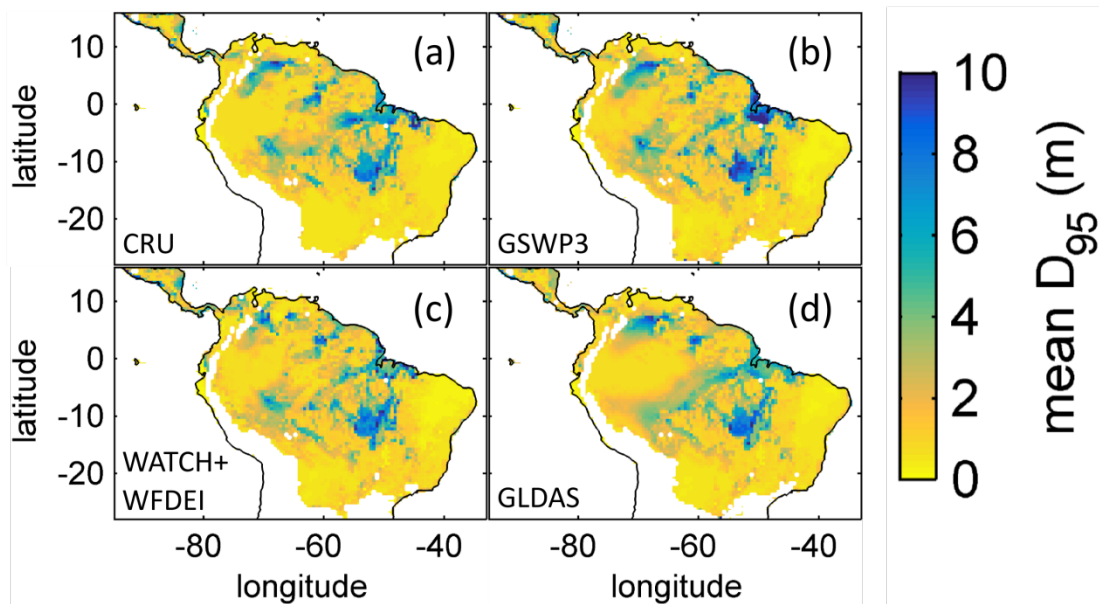
984

985

986

987

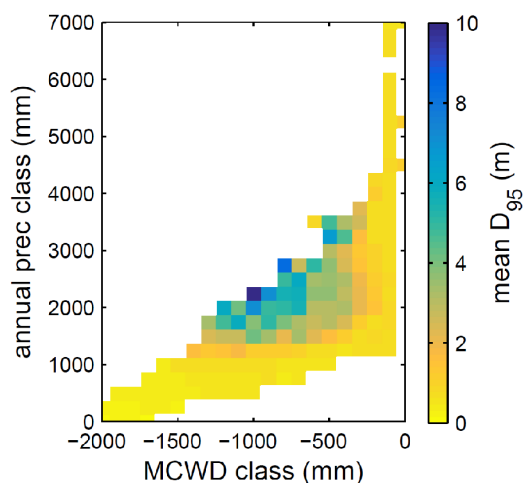
Figure 4: Distributions of simulated mean monthly NPP for each D_{95_max} class for 2001-2010 under CRU climate input at two FluxNet sites. a) Site MAN K34 near the city of Manaus. b) Site STM K67 near the city of Santarem. For more site information see Table A2 and Fig. 7a.



988

989
990
991

Figure 52: Regional NPP-weighted mean rooting depth ($\overline{D_{95}}$) of all sub-PFTs (evergreen and deciduous PFTs combined) for 2001-2010 and different climate inputs simulated with LPJmL4.0-VR. a) CRU climate input. b) GSWP3 climate input. c) WATCH+WFDEI climate input. d) GLDAS climate input. The color scale maximum is set to 10 m.



992
993
994
995
996
997

Figure 6: Mean rooting depth depicted as mean $\overline{D_{95}}$ over classes of MCWD and annual precipitation sums. Class step size for precipitation was set to 250 mm and class size for MCWD was set to 50 mm. Regions with high amounts of annual rainfall and lower seasonality exclusively favour shallow rooted forests (low $\overline{D_{95}}$). $\overline{D_{95}}$ increases with decreasing MCWD (increasing seasonal drought stress) and decreasing sums of annual precipitation. Below 1200 mm of annual rainfall or 1100 mm of MCWD $\overline{D_{95}}$ sharply decreases again. Note this figure does not consider soil depth. The color scale maximum is set to 10 m.

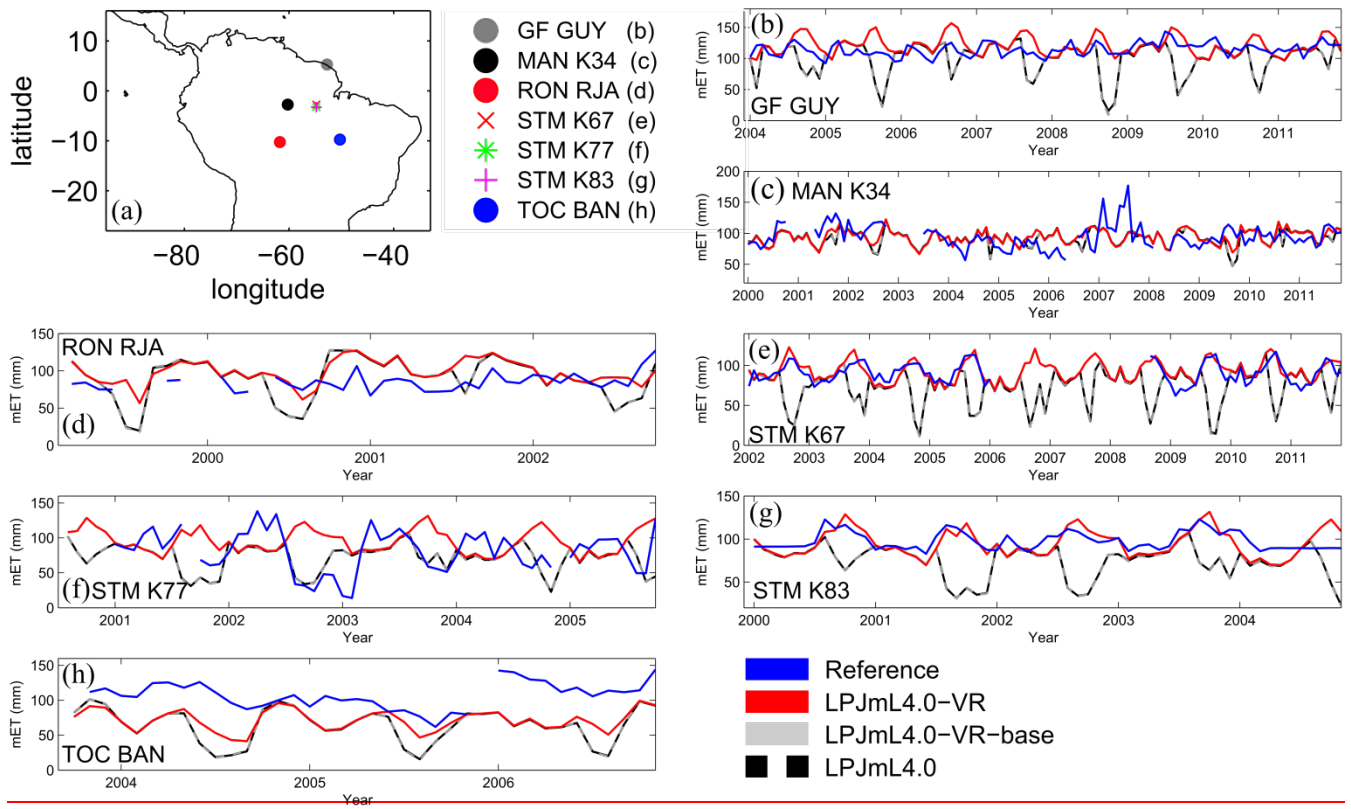


Figure 7: Comparisons of monthly ET between different Fluxnet sites and respective simulation output of the different LPJmL model versions used in this study forced with CRU climate. a) Geographical location of different Fluxnet sites (see also Table A2). For statistical measures of the individual comparison see Table A3.

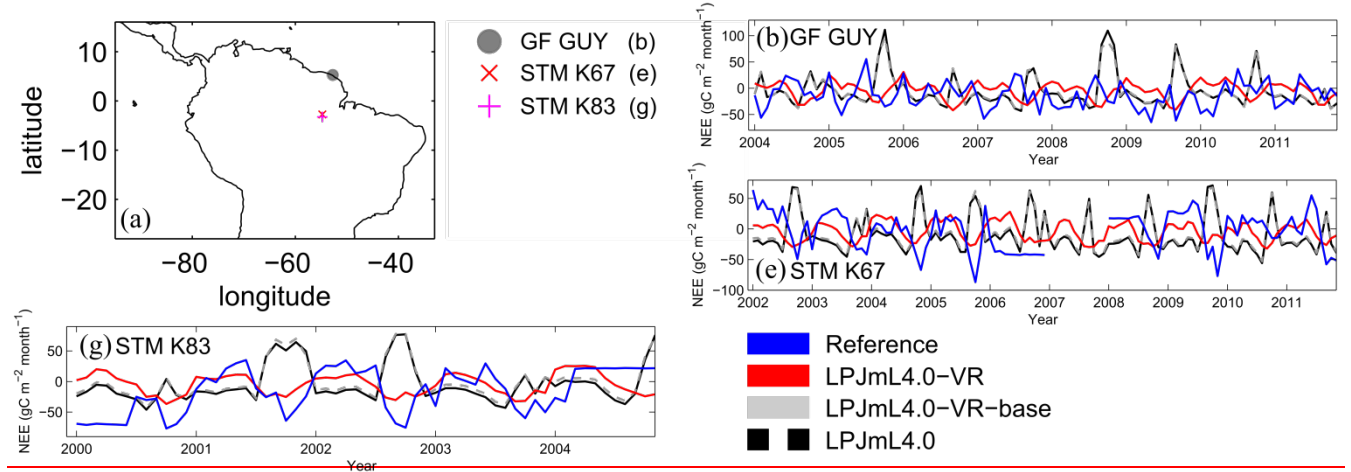
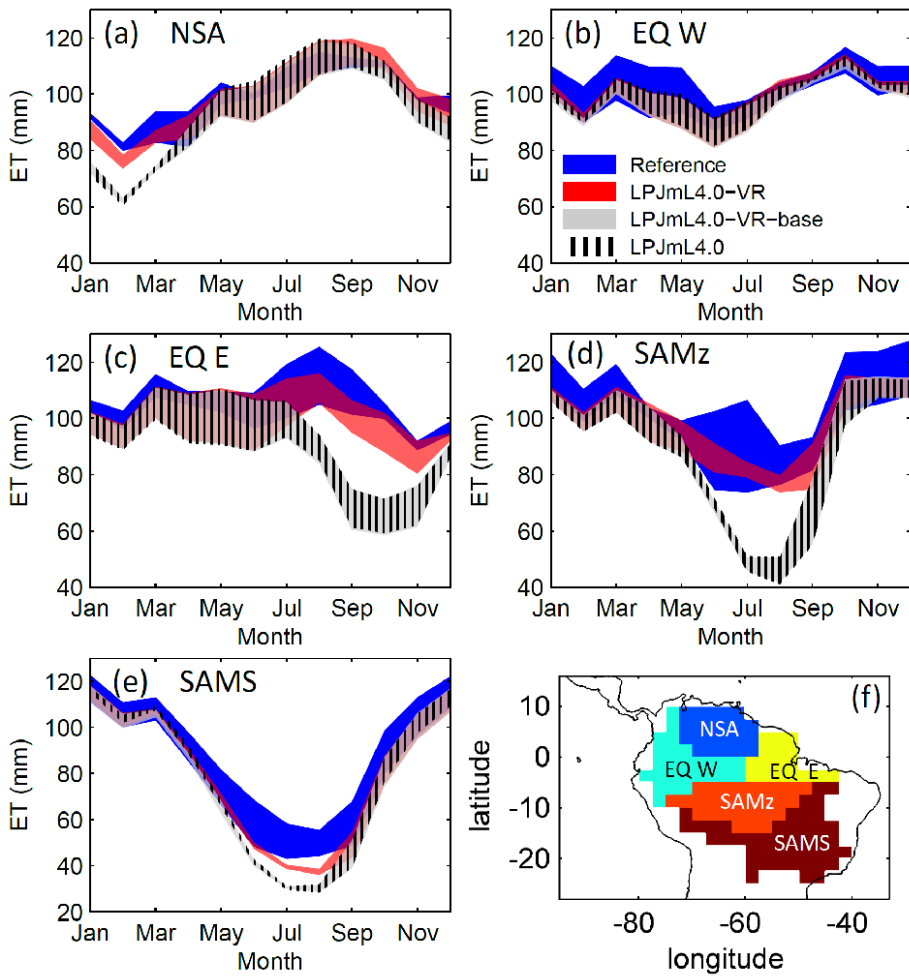


Figure 8: Comparisons of monthly NEE between different Fluxnet sites and respective simulation output of the different LPJmL model versions used in this study forced with CRU climate. a) Geographical location of different Fluxnet sites (see also Table A2). For statistical measures of the individual comparison see Table A4. Note due to data scarcity only 3 Fluxnet sites are shown. Plots of all sites are shown in Fig. A5. We kept panel labelling as in Fig. 7 to ensure easy comparability.



1007

1008

1009

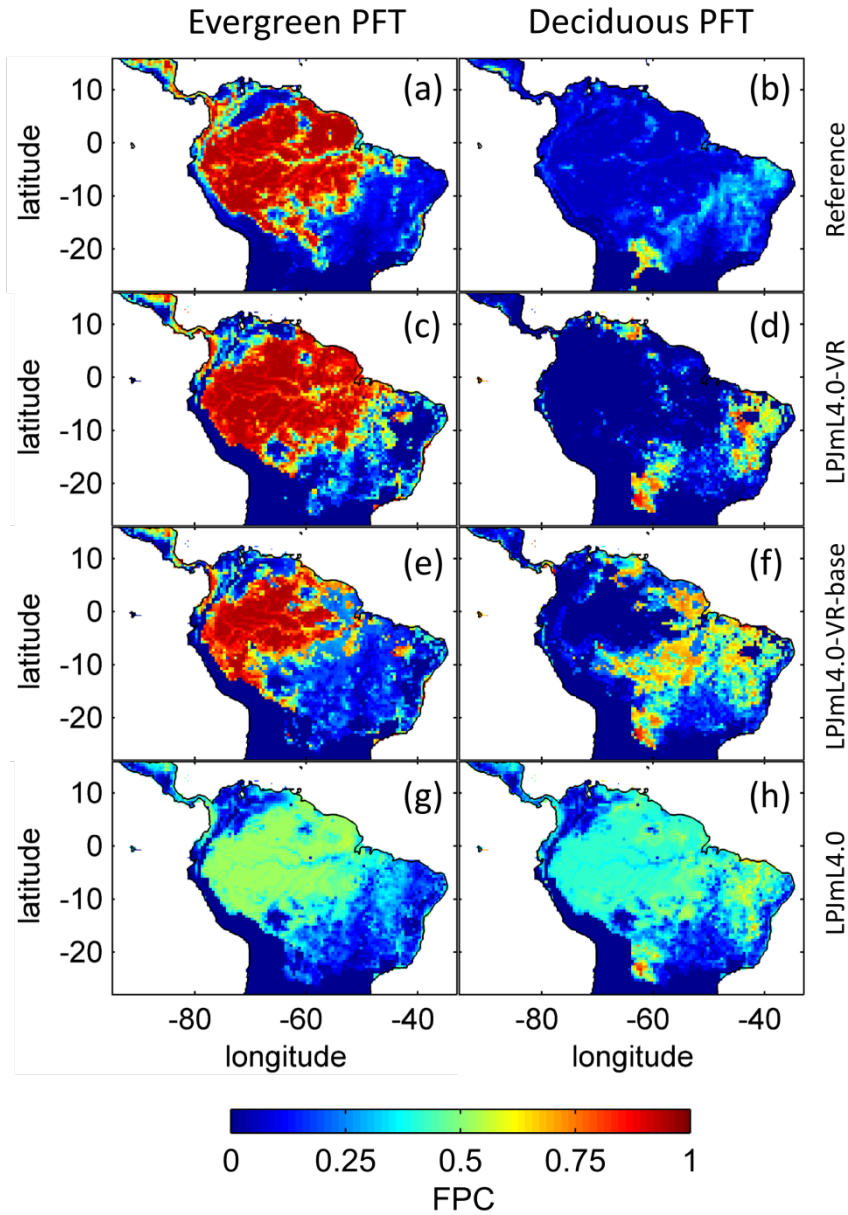
1010

1011

1012

1013

Figure 93: Comparisons of continental scale gridded ET products against simulated ET within 5 regional climatological clusters (a-e) as defined in Sect. 2.5.1. Shown is the mean annual cycle of 1981-2010 and the mean for the whole cluster area. Corridors denote the minimum-maximum range between either the “Reference” ET products (Sect. 2.5.1 Validation data) or the model outputs under the different climate forcings used in this study. f) Geographical extent of climatological clusters (adapted from Sörensson and Ruscica, 2018). Statistical measures of the individual comparisons can be found in Table A5-B3 (comparisons of corridor means).



1014
1015
1016
1017
1018
1019
1020
1021
1022

Fig. 104: Foliage projected cover (FPC) of evergreen (a, c, e, g) and deciduous (b, d, f, h) PFTs over the study region. a)-b) Satellite-derived vegetation composition from ESA Land cover CCI V2.0.7 (Li et al., 2018) reclassified to the PFTs of LPJmL as in (Forkel et al., 2014). b)-c) LPJmL4.0-VR. d)-e) LPJmL4.0-VR-base. f)-g) LPJmL4.0. All LPJmL model versions were forced with CRU climate input. The shown FPC for all models refers to 2001-2010. For statistical measures of individual comparisons between model versions (c-h) and satellite derived vegetation composition (a-b) see Table [A6B4](#).

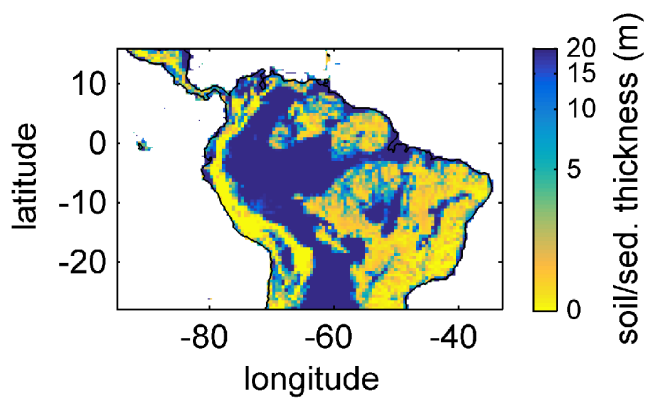
Table 1: ~~β values assigned to the 10 sub-PFTs of each tropical PFT (evergreen and deciduous) in LPJmL4.0 VR and the corresponding maximum rooting depth reached by 95% of the roots (D_{95_max}).~~

| sub-PFT number | β value | D_{95_max} (m) |
|----------------|---------------|-------------------|
| 1 | 0.9418 | 0.5 |
| 2 | 0.9851 | 2 |
| 3 | 0.9925 | 4 |
| 4 | 0.995 | 6 |
| 5 | 0.9963 | 8 |
| 6 | 0.9971 | 10 |
| 7 | 0.9976 | 12 |
| 8 | 0.9981 | 14 |
| 9 | 0.9986 | 16 |

1023

1024

12 Appendix

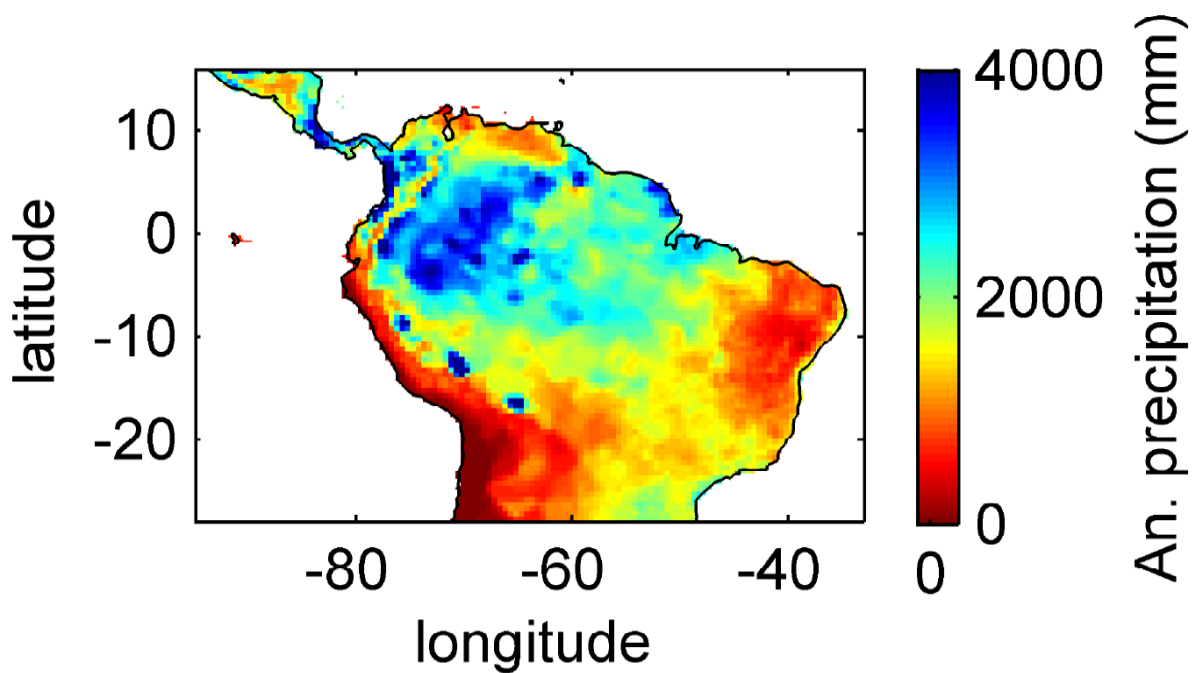


1025

1026

1027

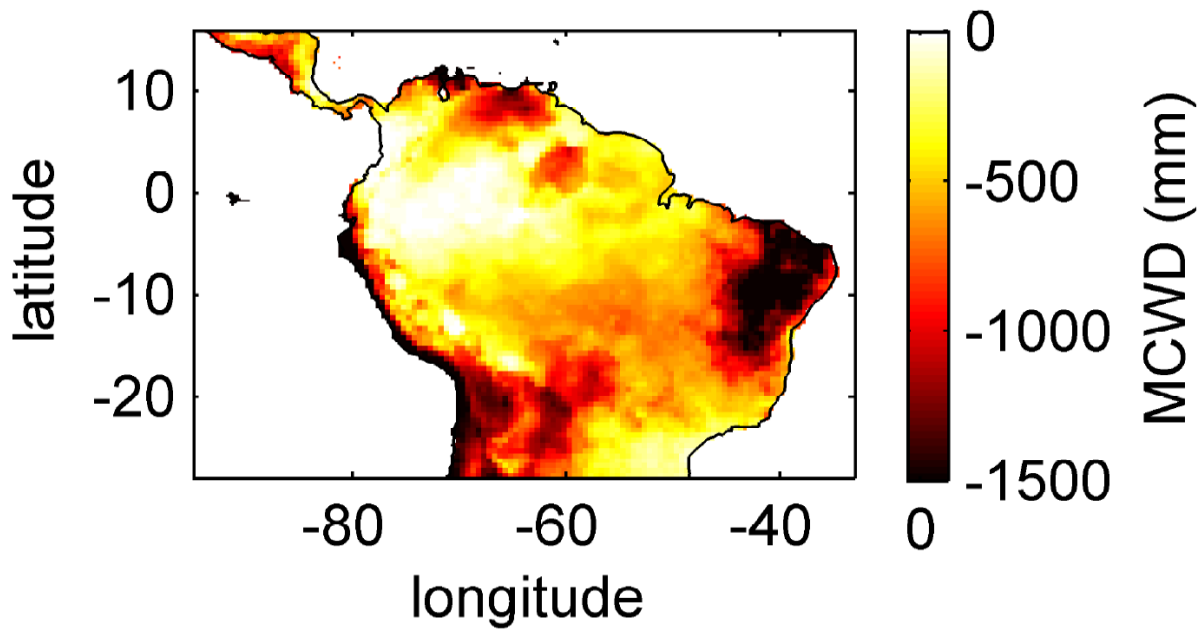
Figure A1: Soil/sediment thickness from regrided to the $0.5^\circ \times 0.5^\circ$ longitude-latitude grid of LPJmL4.0 VR and restricted to a maximum of 20 m. Colorbar in decadic logarithm.



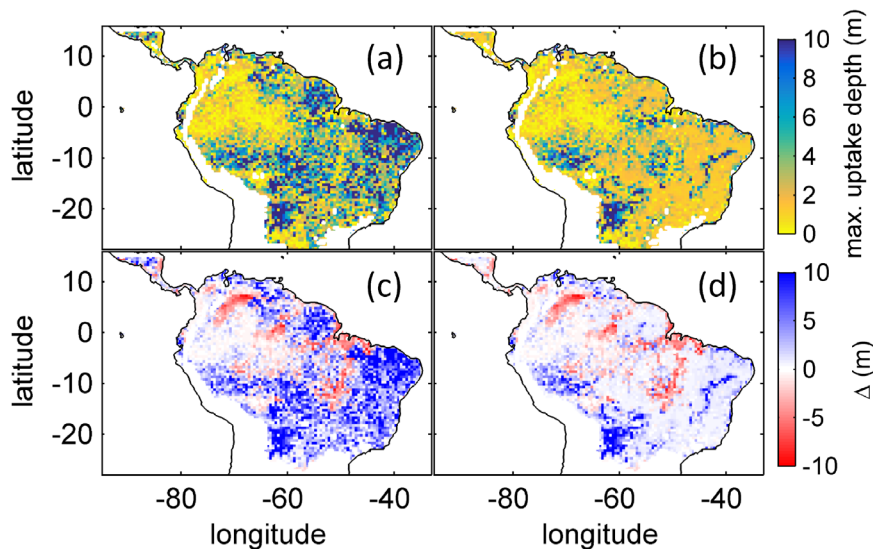
1028

1029

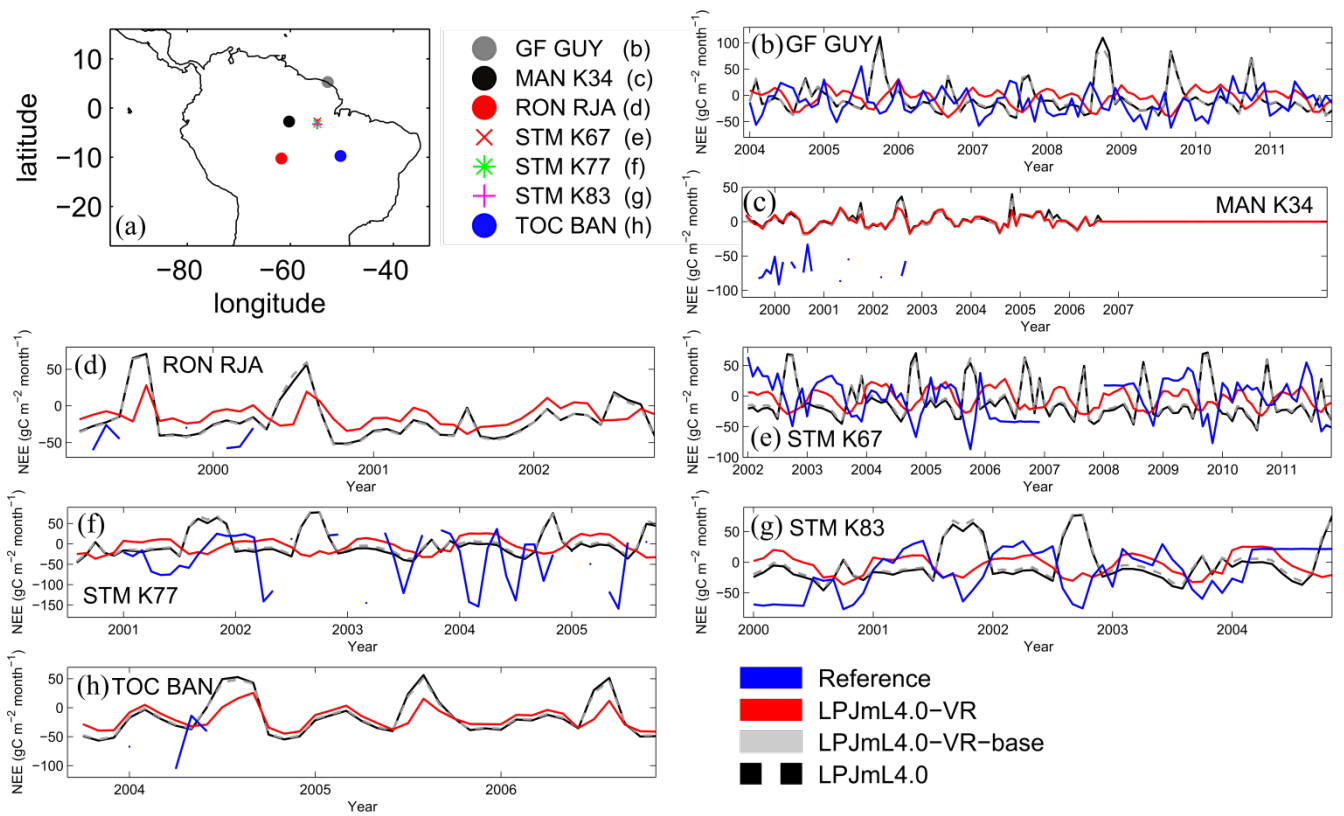
Figure A2: Mean annual precipitation for 2001-2010 under CRU climate input.



1030
1031 **Figure A3: Mean annual MCWD for 2001-2010 under CRU climate input.**



1032
1033 **Figure A4: Comparison of simulated to product of maximum tree root water uptake depth (MDRU). a) Original (Fan et al., 2017)**
1034 **MDRU regridded to 0.5°x0.5° resolution of LPJmL4.0 VR. b) Same as a) but adjusted to soil depth input used in this study (see**
1035 **2.3.2), in cases where values of (Fan et al., 2017) exceeded this soil depth. The color scale maximum for a) and b) is set to 10 m. c)**
1036 **Difference between a) and simulated with LPJmL4.0 VR under CRU climate forcing (Fig. 6a). d) Difference between b) and**
1037 **simulated with LPJmL4.0 VR under CRU climate forcing (Fig. 5a). Red/blue colors denote higher/lower rooting depths in**
1038 **LPJmL4.0 VR.**
1039



1040
1041
1042

Fig. A5: Comparisons of monthly NEE between different Fluxnet sites and respective simulation output of the different LPJmL model versions used in this study forced with CRU climate. a) Geographical location of different Fluxnet sites (see also Table A2).

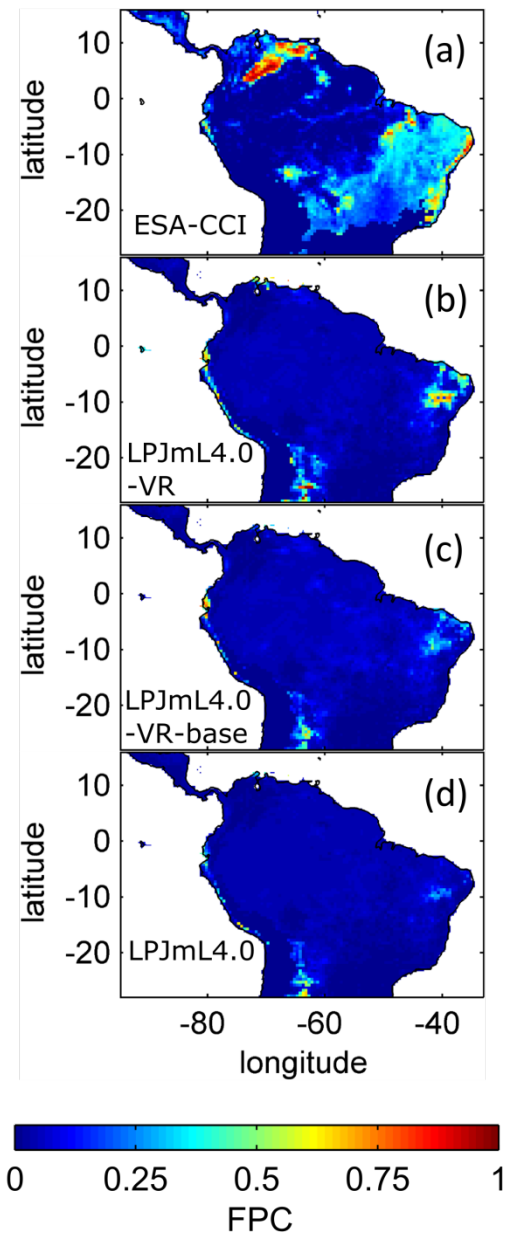


Figure A6: Foliage projected cover (FPC) of the tropical herbaceous PFT over the study region. a) Satellite derived vegetation composition from ESA Land cover CCI V2.0.7 (Li et al., 2018) reclassified to the PFTs of LPJmL as in (Forkel et al., 2014). b) LPJmL4.0-VR. c) LPJmL4.0-VR-base. d) LPJmL4.0. All LPJmL model versions were forced with CRU climate input. The shown FPC for all models refers to 2001-2010.

Regional pattern of simulated above- and belowground biomass

The simulated mean AGB pattern (2001-2010) of LPJmL4.0-VR (Fig. A7) shows that variable tree rooting strategies lead to a contiguous high biomass over the Amazon region. Especially towards the borders of the South Eastern Amazon region in the climatological clusters EQ-E and SAMz, AGB values appear rather homogenous in contrast to constant shallow tree rooting strategies simulated in the other 2 model versions (Fig. A7d-e). In connection with the significantly improved underlying vegetation composition (Fig. 10e-f) it is clear that LPJmL4.0-VR is the only model version capable of simulating high AGB evergreen rainforests across the climatic gradient of the Amazon region (Fig. A2-A3). This pattern is also found by one satellite derived AGB product chosen for evaluation of our model results (Saatchi et al., 2011; Fig. A7b) which yields a corresponding NME close to 0 (Table A7). However, compared to this product low NME values are found for all model versions. Surprisingly, in comparison to the other AGB validation product (Avitabile et al., 2016a; Fig. A7a) LPJmL4.0-VR-base yields a smaller NME than LPJmL4.0-VR. Considering the significantly less accurate underlying vegetation composition of LPJmL4.0-VR-base as well as LPJmL4.0 (Fig. 10) we regard such comparisons as critical in this context. Simulating diverse tree rooting strategies in connection with investment into coarse root structures in LPJmL4.0-VR allows analysing carbon investment into the newly implemented root carbon pools (Sect. 2.2.4). As expected, belowground biomass (BGB; Fig. A8) follows the simulated pattern (Fig. 5). Highest BGB is found at maximum values of and vice versa. It is important to note that LPJmL4.0-VR appears to underestimate BGB compared to empirical findings in the Amazon region. While LPJmL4.0-VR shows BGB making up a range of 3.6-16.2% of total biomass across the Amazon region, different site specific empirical studies found mean values at the upper end or significantly exceeding this range (Fearnside, 2016). The most plausible explanation for underestimating BGB is that LPJmL4.0-VR does not account for root structures needed for tree statures. Acknowledging tree statures would increase below ground carbon investment and therefore BGB.

1068
 1069
 1070
 1071
 1072
 1073
 1074
 1075
 1076
 1077
 1078
 1079
 1080
 1081

Nevertheless, below-ground carbon investment for tree species would apply for all sub-PFTs simultaneously and would therefore most likely not significantly change competition dynamics and resulting distributions of tree rooting strategies found in this study.

Comparisons of AGB pattern between all model versions of this study and different biomass products are difficult, since only LPJmL4.0 VR shows a reasonable geographical distribution of underlying PFTs across the study area (Fig. 10, Table A6). Therefore, differences in biomass are not solely the consequence of different productivities directly related to diversity in tree rooting strategies, but also the consequence of simulated PFT dominance, i.e. rather an indirect effect of diversity in tree rooting strategies. Concentrating on LPJmL4.0 VR only, the model matches substantially better with the gridded biomass product of Saatchi et al. (2011; Table A7), since this product shows generally higher biomass values across the Amazon region which are more similar to LPJmL4.0 VR. Therefore, the higher NME found in the comparison to the biomass product of Avitabile et al. (2016) is mainly caused by divergence of mean biomass values of the evergreen PFT across the whole study area rather than pattern divergence. Thus, we argue lowering overall biomass values in LPJmL4.0 VR would improve its match with Avitabile et al. (2016) which is a matter of adjusting overall maximum tree mortality rates (Sect. 2.2.7).

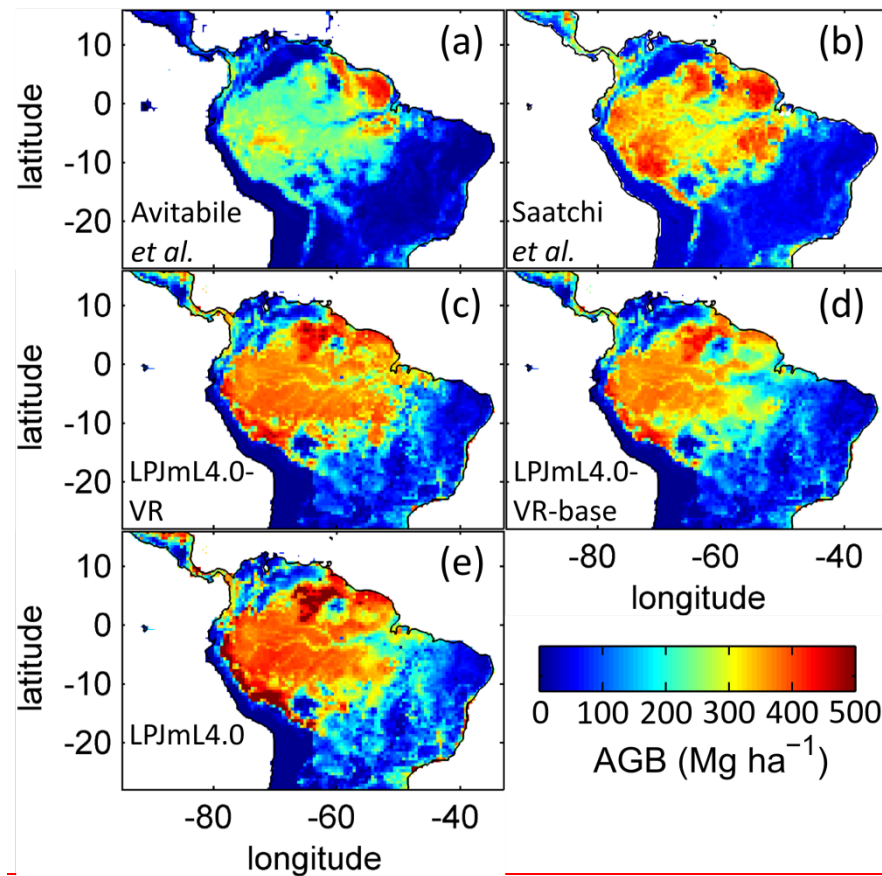
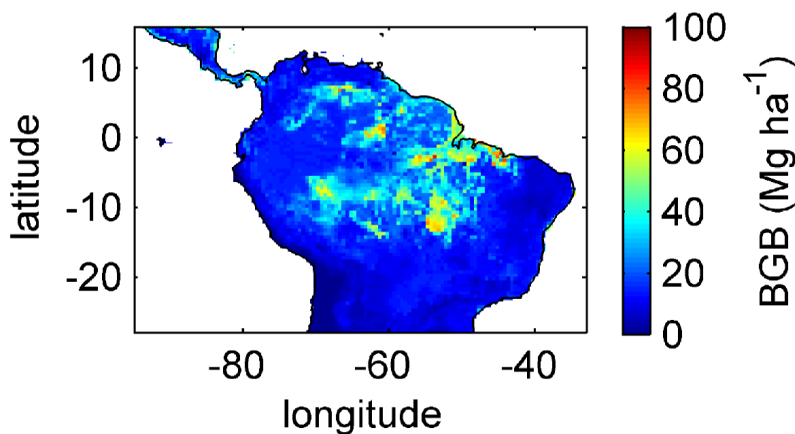


Fig. A7: Comparison of simulated AGB and satellite derived AGB validation products regridded to the spatial resolution of LPJmL models. a) Biomass validation product from Avitabile et al. (2016b). b) AGB validation product from Saatchi et al., (2011). c) Mean AGB simulated for the time span 2001-2010 with c) LPJmL4.0 VR. d) LPJmL4.0 VR base and e) LPJmL4.0. For statistical measures of individual comparisons between model versions (e-e) and satellite derived AGB evaluation products (a-b) see Table A7.

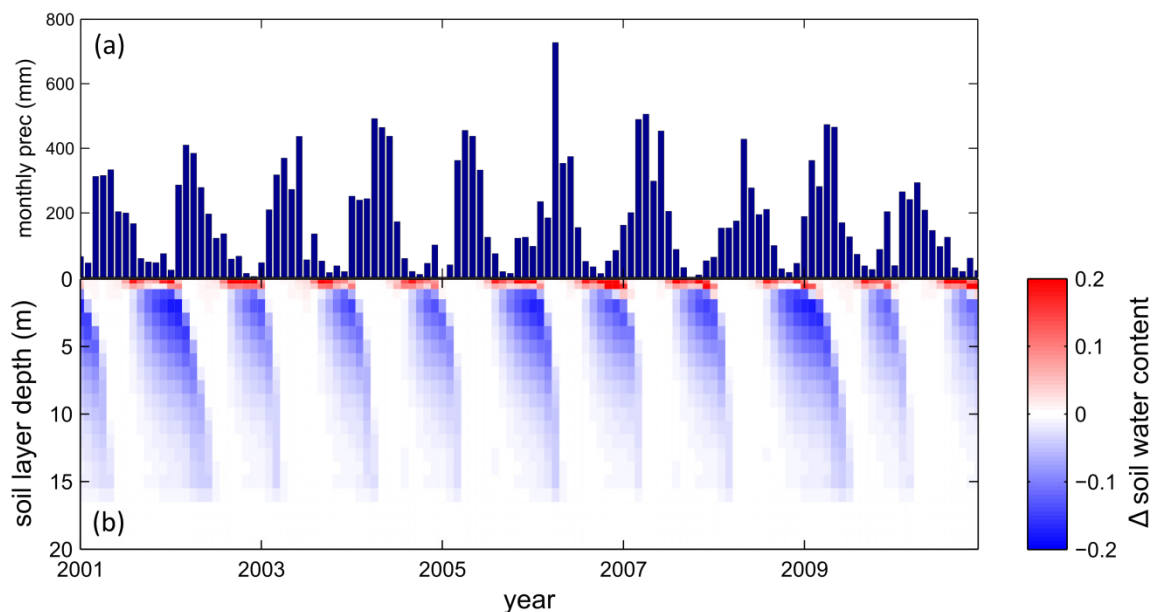
1082
 1083
 1084
 1085
 1086
 1087



1088

1089
1090
1091

Fig. A8: Mean sum (2001-2010) of belowground biomass (BGB; sum of tree coarse and fine roots) of evergreen and deciduous tree PFTs simulated with LPJmL4.0 VR under CRU climate forcing.



1092
1093
1094
1095
1096
1097
1098
1099
1100
1101

Figure A9: Difference in soil water reaction to seasonal precipitation between LPJmL4.0 VR base and LPJmL4.0 VR at Fluxnet site STM_KM67 a) Mean monthly precipitation input from CRU for 2001-2010. b) Difference in monthly relative soil water content between LPJmL4.0 VR base and LPJmL4.0 VR forced with CRU climate for 2001-2010. The underlying model output variable “soil water content” of each model version is a number between 0 and 1 depicting the relative water saturation of the soil. Blue colors denote lower soil water content in LPJmL4.0 VR and red colors a lower soil water content in LPJmL4.0 VR base.

Table A1: Soil layer partitioning scheme used in LPJmL4.0 VR. The first meter of the soil column is split into 3 soil layers and after 1m of soil depth each following soil layer is assigned a thickness of 1 m as in LPJmL4.0. Whereas LPJmL4.0’s last soil layer reaches 3 m, LPJmL4.0 VR’s last soil layer reaches 20 m.

| Soil layer number | Soil layer boundary (m) | Soil layer thickness (m) |
|-------------------|-------------------------|--------------------------|
| 1 | 0.2 | 0.2 |
| 2 | 0.5 | 0.3 |
| 3 | 1 | 0.5 |
| 4 | 2 | 1 |
| ... | ... | ... |
| 23 | 20 | 1 |

1102
1103

Table A2: Description of Fluxnet sites used for the evaluation of simulated ET.

| Site name | Short name | Country | LPJmL coordinate latitude | longitude |
|-------------------------------------|------------|---------|---------------------------|-----------|
| Eotone-Banana | TOC_BAN | Brazil | -9.75 | -50.25 |
| Manaus-ZF2 | MAN_K34 | Brazil | -2.75 | -60.25 |
| Santarem-Km67-Primary-Forest/BR-Sa1 | STM_K67 | Brazil | -2.75 | -54.75 |
| Santarem-Km77-Pasture/BR-Sa2 | STM_K77 | Brazil | -3.25 | -54.75 |
| Santarem-Km83-Logged-Forest/BR-Sa1 | STM_K83 | Brazil | -3.25 | -54.75 |

Rond. Rebio Jaru Ji
Parana Tower B/BR-
Ji3

| | | | |
|---------|--------|--------|--------|
| RON_RJA | Brazil | -10.25 | -61.75 |
| | French | | |
| GF_GUY | Guiana | 5.25 | -52.75 |

Table A3: Normalized mean error (NME), coefficient of determination (r^2) and p-value of F-statistic piecewise calculated for simulated ET of the different LPJmL model versions used in this study forced with CRU climate input and Fluxnet data of ET at 7 Fluxnet sites (in accordance with Fig. 7).

| Statistic | Model | TOC_BA N | MAN_K3 4 | STM_K6 7 | STM_K7 7 | STM_K8 3 | RON_RJ A | GF_GU Y |
|-----------|--------------|-------------|-------------|-------------|-------------|-------------|-------------|------------|
| NME | LPJmL4.0-VR | 2.41 | 1.11 | 0.75 | 1.38 | 1.10 | 2.28 | 1.57 |
| | LPJmL4.0-VR- | | | | | | | |
| | base | 2.92 | 1.22 | 2.29 | 0.98 | 2.74 | 2.73 | 2.38 |
| - | LPJmL4.0 | 2.93 | 1.23 | 2.27 | 0.98 | 2.74 | 2.70 | 2.36 |
| r^2 | LPJmL4.0-VR | 0.09 | 0.03 | 0.53 | 0.17 | 0.43 | 0.01 | 0.08 |
| | LPJmL4.0-VR- | | | | | | | |
| | base | 0.10 | 0.00 | 0.33 | 0.14 | 0.03 | 0.01 | 0.01 |
| - | LPJmL4.0 | 0.09 | 0.00 | 0.33 | 0.14 | 0.03 | 0.01 | 0.01 |
| p-value | LPJmL4.0-VR | 0.075 | 0.041 | <0.001 | 0.002 | <0.001 | 0.575 | 0.005 |
| | LPJmL4.0-VR- | | | | | | | |
| | base | 0.067 | 0.585 | <0.001 | 0.005 | 0.221 | 0.517 | 0.277 |
| | LPJmL4.0 | 0.068 | 0.672 | <0.001 | 0.005 | 0.221 | 0.514 | 0.274 |

Table A4: Normalized mean error (NME), coefficient of determination (r^2) and p-value of F-statistic piecewise calculated for simulated NEE of the different LPJmL model versions used in this study forced with CRU climate input and Fluxnet data of NEE at 3 Fluxnet sites (in accordance with Fig. 8).

| Statistic | Model | STM_K67 | STM_K83 | GF_GUY |
|-----------|--------------|---------|---------|--------|
| NME | LPJmL4.0-VR | 0.90 | 0.84 | 1.30 |
| | LPJmL4.0-VR- | | | |
| | base | 1.62 | 1.36 | 1.52 |
| - | LPJmL4.0 | 1.68 | 1.39 | 1.52 |
| r^2 | LPJmL4.0-VR | 0.16 | 0.14 | 0.00 |
| | LPJmL4.0-VR- | | | |
| | base | 0.32 | 0.06 | 0.03 |
| - | LPJmL4.0 | 0.33 | 0.07 | 0.03 |
| p-value | LPJmL4.0-VR | <0.001 | 0.003 | 0.515 |
| | LPJmL4.0-VR- | | | |
| | base | <0.001 | 0.055 | 0.046 |
| | LPJmL4.0 | <0.001 | 0.047 | 0.059 |

Table A5: Normalized mean error (NME), coefficient of determination (r^2) and p-value of F-statistic piecewise calculated for the simulated ET of the different LPJmL model versions used in this study and continental scale gridded ET products within 5 regional climatological clusters. With respect to Fig. 9 comparisons are based on the monthly mean of corridors shown, i.e. 1) the monthly mean of all outputs produced by one LPJmL model version but forced with different climate inputs and 2) the monthly mean of all continental scale gridded ET data products.

| Statistic | Model | NSA | EQ_W | EQ_E | SAmz | SAMS |
|-----------|--------------|------|------|------|------|------|
| NME | LPJmL4.0-VR | 0.08 | 0.26 | 0.62 | 0.20 | 0.06 |
| | LPJmL4.0-VR- | | | | | |
| | base | 0.37 | 0.42 | 1.95 | 0.58 | 0.13 |
| - | LPJmL4.0 | 0.34 | 0.26 | 1.92 | 0.58 | 0.11 |
| r^2 | LPJmL4.0-VR | 0.98 | 0.94 | 0.91 | 0.98 | 1.00 |

| | | | | | | |
|---------|-------------------------|-------|-------|-------|-------|-------|
| | LPJmL4.0-VR- | | | | | |
| | base | 0.94 | 0.96 | 0.20 | 0.91 | 0.99 |
| - | LPJmL4.0 | 0.93 | 0.96 | 0.21 | 0.90 | 0.99 |
| | | < | < | < | < | < |
| p-value | LPJmL4.0-VR | 0.001 | 0.001 | 0.001 | 0.001 | 0.001 |
| | LPJmL4.0-VR- | < | < | | < | < |
| | base | 0.001 | 0.001 | 0.143 | 0.001 | 0.001 |
| | | < | < | | < | < |
| | LPJmL4.0 | 0.001 | 0.001 | 0.135 | 0.001 | 0.001 |

~~Table A6: Normalized mean error (NME) of FPC comparison piecewise calculated between 1) the satellite derived vegetation composition from ESA Land cover CCI V2.0.7 (Li et al., 2018) reclassified to the PFTs of LPJmL as in Forkel et al. (2014) and 2) all LPJmL model versions used in this study forced with CRU climate data (in accordance with Fig. 10).~~

| Statistic | Model | FPC | |
|-----------|-------------------------|-----------|-----------|
| | | Evergreen | Deciduous |
| NME | LPJmL4.0-VR | 0.31 | 1.01 |
| | LPJmL4.0-VR- | | |
| | base | 0.38 | 1.5 |
| | LPJmL4.0 | 0.47 | 1.76 |

~~Table A7: Normalized mean error (NME) of AGB comparison piecewise calculated between 1) the satellite derived AGB validation products and 2) all LPJmL model versions used in this study forced with CRU climate data (in accordance with Fig. A7).~~

| Statistic | Model | Avitabile <i>et al.</i> | Saatchi <i>et al.</i> |
|-----------|-----------------------------|-------------------------|-----------------------|
| NME | LPJmL4.0-VR | 0.78 | 0.12 |
| | LPJmL4.0-VR-base | 0.69 | 0.11 |
| | LPJmL4.0 | 1.09 | 0.14 |

Appendix A

1 Methods

A new tree rooting scheme for LPJmL4.0

In this section we describe the new basic scheme for soil layer partitioning, the new tree rooting scheme, the simulation of belowground carbon investment, and how different tree rooting strategies (implemented in the new scheme) compete.

1.1 Scheme for soil layer partitioning

LPJmL4.0 employs a globally universal soil depth of 3 m. For LPJmL4.0-VR we extended the general maximum soil depth to 20 m (but restrict it to local soil depth information at spatial model resolution; Manuscript Sect. 2.3.2). We applied the same basic scheme for soil layer partitioning from LPJmL4.0 (Schaphoff et al., 2018), in order to keep model differences small (Table A1). We chose a maximum of 20 m soil depth to considerably increase the maximum soil depth compared to constant 3 m in LPJmL4.0, while keeping the increment of computational demand connected to adding more soil layers within an acceptable range. Equal to LPJmL4.0 (Schaphoff et al., 2018), we use a grid cell specific soil texture information which is applied to the whole soil column.

1.2 Water balance, infiltration and percolation

We here provide a very brief description of LPJmL's water balance and soil hydrology. A detailed description can be found in Schaphoff et al. (2018).

Hydraulic conductivity and water holding capacity (water content at permanent wilting point, at field capacity, and at saturation) for each grid cell are derived from information on soil texture from the Harmonized World Soil Database (HWSD) version 1 (Nachtergaele et al., 2009) and relationships between texture and hydraulic properties from Cosby et al. (1984). Each soil layer's (Appendix A Sect. 1.1) water content can be altered by infiltrating rainfall and percolation. The soil water content of the first soil layer determines the infiltration rate of rain and irrigation water. The excess water that does not infiltrate generates surface water runoff. Water percolation through the soil layers is calculated by the storage routine technique (Arnold et al., 1990) as used in regional hydrological models such as SWIM (Krysanova et al., 1998). Water percolation thus depends on the hydraulic conductivity of each soil layer and the soil water content between field capacity and saturation at the beginning and the end of the day for all soil layers. Similar to water infiltration into the first soil layer, percolation in each soil layer is limited by the soil moisture of the following lower layer. Excess water over the saturation levels forms lateral runoff in each layer and contributes to subsurface runoff. Surface and subsurface runoff accumulate to river discharge. The routines for water balance, infiltration and percolation were not changed for LPJmL4.0-VR. Thus the routines now apply for soil columns of up to 20 m depth (Appendix A Sect. 1.1).

1.3 Diversifying general tree rooting strategies

In LPJmL4.0 the tree rooting strategy of a PFT is reflected by a certain prescribed vertical distribution of fine roots throughout the soil column. Each soil layer l is assigned a PFT specific relative amount of fine roots $rootdist_l$:

$$rootdist_l = rootdist(z_l) - rootdist(z_{l-1}) \quad \text{Eq. (A1)}$$

where z_l is the soil layer boundary depth in cm of each soil layer l and $rootdist(z_l)$ is the relative amount of fine roots between the forest floor and the boundary of soil layer l . The function $rootdist(z)$ is defined following Jackson et al. (1996):

$$rootdist(z) = \frac{1 - \beta^z}{1 - \beta^{z_{bottom}}} \quad \text{Eq. (A2)}$$

where β is a constant parameter shaping the vertical distribution of fine roots and therefore determining the tree rooting strategy and z_{bottom} is the maximum soil depth in cm. In LPJmL4.0 each PFT is assigned a different β -value reflecting the average tree rooting strategy on this broad PFT scale (Schaphoff et al., 2018).

To quantify the maximum rooting depth of PFTs that actually results from this approach (Eq. A1&A2) we here calculate the depth at which the cumulated fine root biomass from the soil surface downwards is 95% (D_{95_max}) as follows:

$$D_{95_max} = \frac{\log(1 - 0.95 \cdot (1 - \beta^{z_{bottom}}))}{\log(\beta)} \quad \text{Eq. (A3)}$$

In LPJmL4.0 the β -values of tropical tree PFTs are set to 0.962 for the tropical broadleaved evergreen tree and to 0.961 for the tropical broadleaved deciduous tree following Jackson et al. (1996). According to Eq. A3 both PFTs have a D_{95_max} smaller than 1 m. For LPJmL4.0-VR we extended this representation of tree rooting strategies by splitting both tropical tree PFTs into 10 sub-PFTs and assigned each with a different β -value. These values were chosen to cover a range of different D_{95_max} values between 0.5 and 18m (Table A2). We chose 18 m as the largest D_{95_max} value in order to avoid that roots of the respective sub-PFT significantly exceed the maximum soil depth of 20 m (see also Appendix A Sect. 1.5). Fig. A1 shows the new maximum distribution of fine roots throughout the soil column for the different β -values chosen (Table A2).

1.4 Belowground carbon investment

Tropical trees can avoid water stress under seasonally dry climate by growing relatively deep roots (Brum et al., 2019; Fan et al., 2017) which goes along with increased below-ground carbon investment. Thus, the need for deep water access creates a trade-off between below-ground and above-ground carbon investment. Therefore, a new carbon allocation scheme for

LPJmL4.0-VR was necessary to account for this trade-off in order to reproduce observed local to regional patterns and distributions of tree rooting strategies instead of prescribing them. In LPJmL4.0-VR we introduced two new carbon pools, namely root sapwood and root heartwood. Like stem sapwood in LPJmL4.0, also root sapwood in LPJmL4.0-VR needs to satisfy the assumptions of the pipe model (Shinozaki et al., 1964; Waring et al., 1982). The pipe model describes, that for a certain amount of leaf area a certain amount of water conducting tissue must be available. In LPJmL4.0 the cross-sectional area of stem sapwood needs to be proportional to the leaf area LA_{ind} as follows:

$$LA_{ind} = k_{la:sa} \cdot SA_{ind} \quad \text{Eq. (A4)}$$

where $k_{la:sa}$ is a constant describing the ratio of leaf area and stem sapwood cross-sectional area (SA_{ind}). In LPJmL4.0-VR we also apply the pipe model to root sapwood. Root sapwood cross-sectional area in the first soil layer is equal to stem sapwood cross-sectional area, as all water must be transported through the root sapwood within this soil layer. In the following soil layers downwards, root sapwood cross-sectional area decreases by the relative amount of fine roots in all soil layers above (Fig. 1). Root sapwood is turned into root heartwood at an equal rate as stem sapwood is turned into stem heartwood, i.e. 5% per year as implemented in LPJmL4.0 (see Schaphoff et al., 2018).

1.5 Root growth

In LPJmL4.0 (Schaphoff et al., 2018) no vertical root growth is simulated, thus the relative distribution of fine roots over the soil column is constant over space and time. It means that PFTs starting from bare ground in a sapling stage display the same relative distribution of fine roots throughout the soil column as a full-grown forest which contradicts the principles of dynamic root growth over a tree's lifetime. Applied to LPJmL4.0-VR, the belowground biomass of an initialized deep rooting-strategy sub-PFT would exceed its aboveground biomass (AGB) by order of magnitudes when considering coarse roots. Consequently, deep rooting strategies would always be disadvantageous, calling for modelling gradual root growth in LPJmL4.0-VR. Unfortunately, little is known about how roots of tropical trees grow over time, given the fact that this research field is strongly time and resource demanding, and at the same time the variety of tree species, rooting strategies and environmental conditions are large (Jenik, 2010). A recent promising study by Brum et al. (2019) was able to capture the effective functional rooting depth (EFRD) of different size classes of 12 dominant tree species in a seasonal Amazon forest where tree roots grow considerably deep with maximum values reaching below 30 m. To our knowledge this is the only study capturing the relation between the size of tropical trees and their maximum rooting depth in a high spatial resolution covering sufficient tree-height classes in order to derive a functional relation between tree height and rooting depth. Following the findings of Brum et al. (2019), we here implemented a logistic root growth function, which calculates a general maximum conceivable tree rooting depth D depending on tree height:

$$D = \frac{S}{1 + e^{-kSh} \cdot \left(\frac{S}{D_0} - 1\right)} \quad \text{Eq. (A5)}$$

where S is the maximum soil depth in the model (20 m), k is a dimensionless constant defining the growth rate of the standard logistic growth function (set to 0.02), h is the average tree height of a PFT in m and D_0 is the initial rooting depth of tree PFT saplings (set to 0.1 m; tree saplings in LPJmL4.0-VR are initialized with a height of 0.45 m as in LPJmL4.0). The distribution of fine root biomass of each sub-PFT in the soil column is then adjusted according to D at each time step, by restricting z_{bottom} in Eq. A2. Every time D crosses a specific soil layer boundary (Appendix A Sect. 1.1) z_{bottom} is assigned the value of the next soil layer boundary. Thus, z_{bottom} increases in discrete steps. Consequently, each tree rooting strategy allowed for in this study (Appendix A Sect. 1.3) shows a logistic growth of rooting depth which is dependent on the sub-PFT height and which saturates towards its specific maximum rooting depth (Fig. A2). Therefore, limitations of aboveground sub-PFT growth due to below-ground carbon investment of different tree rooting strategies (Appendix A Sect. 1.4) are equal in the sapling phase of all sub-PFTs (starting from bare ground) and start to diverge with increasing sub-PFT height. In the case D exceeds the grid cell specific local soil depth (as prescribed by the soil thickness input, see Manuscript Sect. 2.3.2) all

the respective fine root biomass exceeding this soil depth is transferred to the last soil layer matching this soil depth (see also Fig. 1 right panel and Supplementary Video 1 for a visualization of root growth under http://www.pik-potsdam.de/~borissa/LPJmL4_VR/Supplementary_Video_1.pptx).

The parameter k in Eq. A5 was chosen to preserve the slope of the 75%ile function describing the relation between tree height and EFRD as found in Brum *et al.* (2019). We could not implement any of the original functions as suggested in Brum *et al.* (2019) since they deliver unrealistic low values of rooting depth (between 0 and 10cm) for trees ≤ 10 m, which results in a strong competitive disadvantage against herbaceous PFTs in LPJmL4.0-VR. We decided for the slope of the 75%ile function to allow for root growth rates close to the maximum which also allows for the largest $D_{95\ max}$ values in this study (Appendix A Sect. 1.3) to be reached. Note that Brum *et al.* (2019) originally propose a relation between tree diameter at breast height (DBH) and EFRD. For our purposes we related rooting depth to tree height (h), which is calculated from DBH in in LPJmL4.0 according to Huang *et al.* (1992):

$$h = k_{allom2} \cdot DBH^{k_{allom3}} \quad \text{Eq. (A6)}$$

where k_{allom2} and k_{allom3} are constants set to 40 and 0.67, respectively (Schaphoff *et al.*, 2018).

1.6 Competition of rooting strategies

In each grid-cell all sub-PFTs of the evergreen and deciduous tree PFTs compete for light and water following LPJmL4.0's approach to simulate plant competition. In LPJmL4.0, the number of new PFT saplings per unit area (est_{PFT} in $\text{ind m}^{-2} \text{a}^{-1}$) which are established each year is proportional to a maximum establishment rate k_{est} and to the sum of foliage projected cover (FPC; a relative number between 0 and 1) of all tree PFTs present in a grid cell (FPC_{TREE}). It declines in proportion to canopy light attenuation when the sum of woody FPCs exceeds 0.95, thus simulating a decline in establishment success with canopy closure (Prentice *et al.*, 1993):

$$est_{PFT} = k_{est} \cdot (1 - e^{-(1-FPC_{TREE})}) \cdot \frac{1-FPC_{TREE}}{n_{estTREE}} \quad \text{Eq. (A7)}$$

where $n_{estTREE}$ is the number of established tree individuals ($\text{ind m}^{-2} \text{a}^{-1}$). It is important to note that LPJmL4.0 does not simulate individual trees. As a common method of DGVM's, tree saplings enter the average individual of a PFT as described in Schaphoff *et al.* (2018).

To allow for environmental filtering of tree rooting strategies which are best adapted to local environmental conditions, we changed the standard tree establishment scheme in LPJmL4.0-VR. Now, the establishment rates of sub-PFTs (est_{sub_PFT}) are additionally weighted by the local dominance of each sub-PFT as follows:

$$est_{sub_PFT} = k_{est} \cdot (1 - e^{-5 \cdot (1-FPC_{TREE})}) \cdot \frac{1-FPC_{TREE}}{n_{estTREE}} \cdot \frac{FPC_{sub_PFT}}{FPC_{TREE}} \cdot n_{estTREE} \quad \text{Eq. (A8)}$$

where FPC_{sub_PFT} is the FPC of each sub-PFT. The new term leads to a higher establishment rate for productive sub-PFTs relative to their spatial dominance and vice versa, without changing the overall establishment rate as set by Prentice *et al.* (1993). This function has the effect that non-viable sub-PFTs are outcompeted over time.

1.7 Background mortality

In LPJmL4.0 background mortality is modelled by a fractional reduction of PFT biomass, which depends on growth efficiency (Schaphoff *et al.*, 2018). This annual rate of mortality is limited by a constant maximum mortality rate of 3% of tree individuals per year which is applied to all tree PFTs. In other words, the fastest total biomass loss of a tree PFT due to low growth efficiency can happen within about 33 simulation years. In general, this maximum mortality rate can be regarded as a global tuning parameter of biomass accumulation as it caps the maximum biomass loss. Since many mechanisms influencing tree mortality in the real world, e.g. hydraulic failure (Johnson *et al.*, 2018), are not yet implemented in most DGVMs including LPJmL4.0 (Allen *et al.*, 2015), the parameterization of a background tree mortality remains a challenging topic. Under the current model status of LPJmL4.0 maximum mortality rates are a necessary feature, while future model

development must overcome the concept of applying a maximum mortality rate by refining and implementing most important mechanisms that influence tree mortality.

In LPJmL4.0-VR tree PFTs can access water in soil depths which were formerly inaccessible. This enhances the general growth efficiencies of tree PFTs and consequently decreases their overall background mortality. Since global biomass pattern simulated with LPJmL4.0 were already in acceptable range, the maximum background mortality in LPJmL4.0-VR was calibrated and is now increased to 7% in order to counter-balance increased survival rates and therefore biomass accumulation.

1.8 Figures

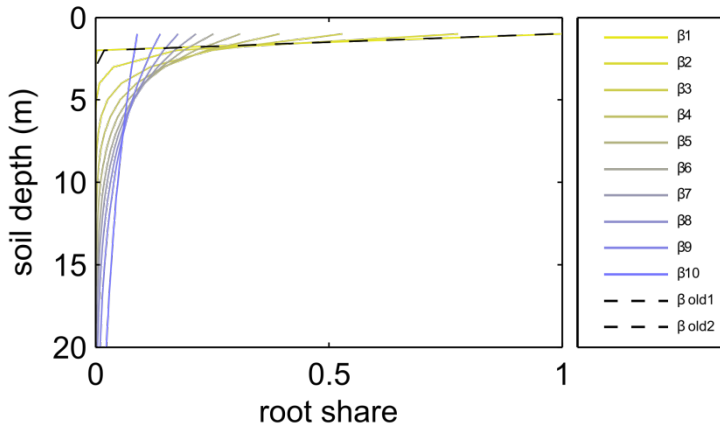


Figure A1: Relative amount of fine roots in each soil layer for different β -values in LPJmL4.0 and LPJmL4.0-VR. In the legend “ β old1-2” correspond to the β -values of the 2 tropical tree PFTs (deciduous and evergreen) simulated in LPJmL4.0. The corresponding graphs lie on top of each other due to marginal differences in their β -values. “ β 1-10” correspond to the 10 β -values used in LPJmL4.0-VR (Table A2) used to create the 10 sub-PFTs of the tropical evergreen and deciduous tree PFTs (Appendix A Sect. 1.3). For LPJmL4.0-VR the fine root distribution at maximum rooting depth is shown. Please note, the first 3 soil layer (as described in Appendix A Sect. 1.1) in this visualization are treated as 1 layer of 1 m thickness for reasons of visual clarity.

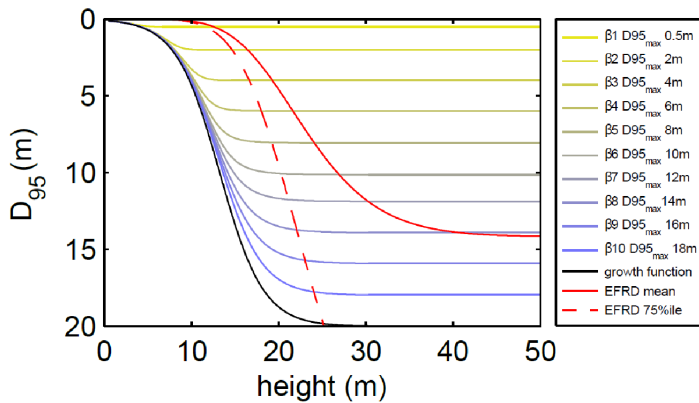


Figure A2: Relation between tree height and rooting depth in LPJmL4.0-VR. Black line: Implemented general growth function of rooting depth (Eq. A5). Lines with colour scale from yellow to blue: Growth functions of rooting depth for each of the 10 sub-PFTs (Sect. 2.2.3). Here temporal rooting depth is expressed as D_{95} and eventually reaches $D_{95\ max}$ (Eq. A3). Red solid line: Mean effective functional rooting depth over tree height (EFRD) adapted from Brum *et al.* (2019) using Eq. A5. Red dashed line: Respective 75%ile EFRD over tree height adapted from Brum *et al.* (2019). Please also see Supplementary Video 1 for a visualization of root growth and development of belowground carbon pools over time under http://www.pik-potsdam.de/~borissa/LPJmL4_VR/Supplementary_Video_1.pptx.

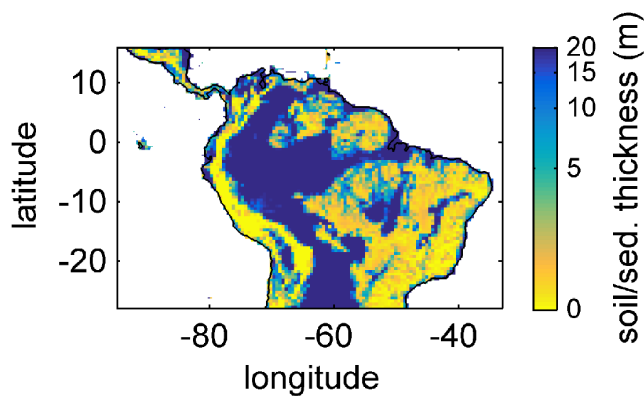


Figure A3: Soil/sediment thickness from (Pelletier et al., 2016) regridded to the 0.5° x 0.5° longitude-latitude grid of LPJmL4.0-VR and restricted to a maximum of 20 m. Colorbar in decadic logarithm.

1.9 Tables

Table A1: Soil layer partitioning scheme used in LPJmL4.0-VR. The first meter of the soil column is split into 3 soil layers and after 1m of soil depth each following soil layer is assigned a thickness of 1 m as in LPJmL4.0. Whereas LPJmL4.0's last soil layer reaches 3 m, LPJmL4.0-VR's last soil layer reaches 20 m.

| <u>Soil layer number</u> | <u>Soil layer boundary (m)</u> | <u>Soil layer thickness (m)</u> |
|--------------------------|--------------------------------|---------------------------------|
| <u>1</u> | <u>0.2</u> | <u>0.2</u> |
| <u>2</u> | <u>0.5</u> | <u>0.3</u> |
| <u>3</u> | <u>1</u> | <u>0.5</u> |
| <u>4</u> | <u>2</u> | <u>1</u> |
| <u>...</u> | <u>...</u> | <u>...</u> |
| <u>23</u> | <u>20</u> | <u>1</u> |

Table A2: β -values assigned to the 10 sub-PFTs of each tropical PFT (evergreen and deciduous) in LPJmL4.0-VR and the corresponding maximum rooting depth reached by 95% of the roots (D_{95_max}).

| <u>sub-PFT number</u> | <u>β-value</u> | <u>D_{95_max} (m)</u> |
|-----------------------|---------------------------------|-------------------------------------|
| <u>1</u> | <u>0.9418</u> | <u>0.5</u> |
| <u>2</u> | <u>0.9851</u> | <u>2</u> |
| <u>3</u> | <u>0.9925</u> | <u>4</u> |
| <u>4</u> | <u>0.995</u> | <u>6</u> |
| <u>5</u> | <u>0.9963</u> | <u>8</u> |
| <u>6</u> | <u>0.9971</u> | <u>10</u> |
| <u>7</u> | <u>0.9976</u> | <u>12</u> |
| <u>8</u> | <u>0.9981</u> | <u>14</u> |
| <u>9</u> | <u>0.9986</u> | <u>16</u> |
| <u>10</u> | <u>0.9993</u> | <u>18</u> |

Table A3: Description of Fluxnet sites used for the evaluation of simulated ET.

| <u>Site name</u> | <u>Short name</u> | <u>Country</u> | <u>LPJmL coordinate</u> | |
|--|-------------------|----------------|-------------------------|------------------|
| | | | <u>latitude</u> | <u>longitude</u> |
| <u>Ecotone Bananal Island/BR-Ban</u> | <u>TOC_BAN</u> | <u>Brazil</u> | <u>-9.75</u> | <u>-50.25</u> |
| <u>Manaus-ZF2 K34/BR-Ma2</u> | <u>MAN_K34</u> | <u>Brazil</u> | <u>-2.75</u> | <u>-60.25</u> |
| <u>Santarem-Km67-Primary Forest/BR-Sa1</u> | <u>STM_K67</u> | <u>Brazil</u> | <u>-2.75</u> | <u>-54.75</u> |
| <u>Santarem-Km77-Pasture/BR-Sa2</u> | <u>STM_K77</u> | <u>Brazil</u> | <u>-3.25</u> | <u>-54.75</u> |
| <u>Santarem-Km83-Logged Forest/BR-Sa3</u> | <u>STM_K83</u> | <u>Brazil</u> | <u>-3.25</u> | <u>-54.75</u> |

| | | | | |
|--|----------------|----------------------|---------------|---------------|
| <u>Rond.- Rebio Jaru Ji Parana- Tower B/BR-Ji3</u> | <u>RON_RJA</u> | <u>Brazil</u> | <u>-10.25</u> | <u>-61.75</u> |
| <u>Guyaflux</u> | <u>GF_GUY</u> | <u>French Guiana</u> | <u>5.25</u> | <u>-52.75</u> |

Appendix B

1 Results

1.1 Local evapotranspiration

Differences of intra-annual rates of ET and NEE between the 3 LPJmL model versions are most pronounced at Fluxnet sites with high seasonality of rainfall (Fig. B6b, e, g and Fig. B7b, e, g). Here, variable tree rooting strategies (LPJmL4.0-VR) lead to a major improvement in reproducing measured Fluxnet NEE and ET, also expressed in reduced NME and increased r^2 -values (Table B1-B2). Whereas, constant tree rooting strategies (LPJmL4.0-VR-base and LPJmL4.0) simulate decreasing ET and increasing NEE during dry seasons at these sites, which is anticorrelated to Fluxnet measurements, variable tree rooting strategies (LPJmL4.0-VR) follow the intra-annual Fluxnet signals. Most pronounced improvements are found at STM K67 and STM K83, where the NME of ET and NEE drop below or close to 1, and where r^2 -values considerably increase compared to the other 2 model versions (Table B1-B2). For STM K67, the r^2 of NEE is higher under LPJmL4.0 and LPJmL4.0-VR-base, but this refers to a significant negative correlation.

At STM K77 (Fig. B6f) local circumstances show the influence of variable rooting strategies on ET in a different way. This former rainforest site was converted to pasture before Eddy covariance measurements began. This local land-use at STM K77 is not representative for the respective 0.5° grid cell, and thus all 3 LPJmL model versions simulate mainly natural vegetation instead of pasture. Therefore, the shallow rooting systems of LPJmL4.0 and LPJmL4.0-VR-base show a better match to ET measurements at STM K77. The site STM K83 (Fig. B6g) is a selectively logged primary forest site which shares the same model grid cell as STM K77 due to their geographical proximity. Again, here only simulations with variable tree rooting strategies (LPJmL4.0-VR) reproduce increased ET and decreased NEE during the dry season. At sites with weaker to no dry season (Fig. B6c, d, h) differences between model versions become less pronounced, as water availability is more stable throughout the year leading to less variable ET.

1.2 Regional pattern of simulated above- and belowground biomass

The simulated mean AGB pattern (2001-2010) of LPJmL4.0-VR (Fig. B10) shows that variable tree rooting strategies lead to a contiguous high biomass over the Amazon region. Especially towards the borders of the South-Eastern Amazon region in the climatological clusters EQ E and SAMz, AGB values appear rather homogenous in contrast to constant shallow tree rooting strategies simulated in the other 2 model versions (Fig. B10d-e). In connection with the significantly improved underlying vegetation composition (Fig. 4e-f) it is clear that LPJmL4.0-VR is the only model version capable of simulating high AGB evergreen rainforests across the climatic gradient of the Amazon region (Fig. B1-B2). This pattern is also found by one satellite derived AGB product chosen for evaluation of our model results (Saatchi *et al.*, 2011; Fig B10b) which yields a corresponding NME close to 0 (Table B6). However, compared to this product low NME values are found for all model versions. Surprisingly, in comparison to the other AGB validation product (Avitabile *et al.*, 2016a; Fig. B9a) LPJmL4.0-VR-base yields a smaller NME than LPJmL4.0-VR. Considering the significantly less accurate underlying vegetation composition of LPJmL4.0-VR-base as well as LPJmL4.0 (Fig. 4) we regard such comparisons as critical in this context.

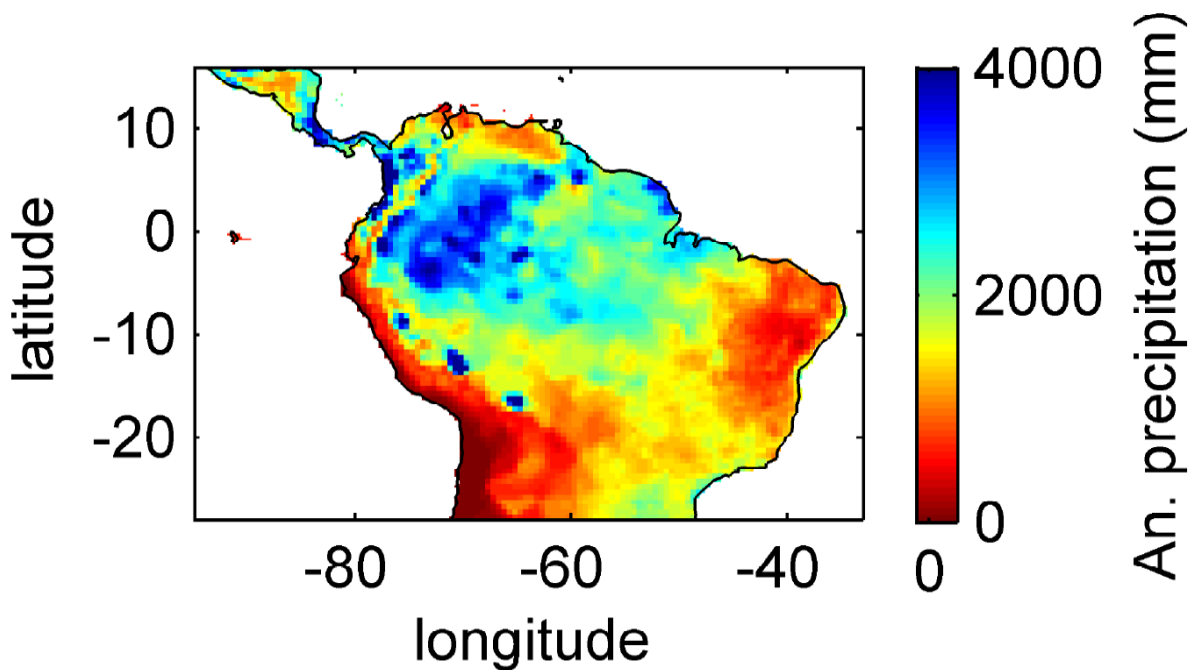
Comparisons of AGB pattern between all model versions of this study and different biomass products are difficult, since only LPJmL4.0-VR shows a reasonable geographical distribution of underlying PFTs across the study area (Fig. 4, Table B4). Therefore, differences in biomass are not solely the consequence of different productivities directly related to diversity

1333 in tree rooting strategies, but also the consequence of simulated PFT dominance, i.e. rather an indirect effect of diversity in
1334 tree rooting strategies. Concentrating on LPJmL4.0-VR only, the model matches substantially better with the gridded
1335 biomass product of Saatchi et al. (2011; Table B5), since this product shows generally higher biomass values across the
1336 Amazon region which are more similar to LPJmL4.0-VR. Therefore, the higher NME found in the comparison to the
1337 biomass product of Avitabile et al. (2016) is mainly caused by divergence of mean biomass values of the evergreen PFT
1338 across the whole study area rather than pattern divergence. Thus, we argue lowering overall biomass values in LPJmL4.0-
1339 VR would improve its match with Avitabile et al. (2016) which is a matter of adjusting overall maximum tree mortality rates
1340 (Appendix A Sect. 1.7).

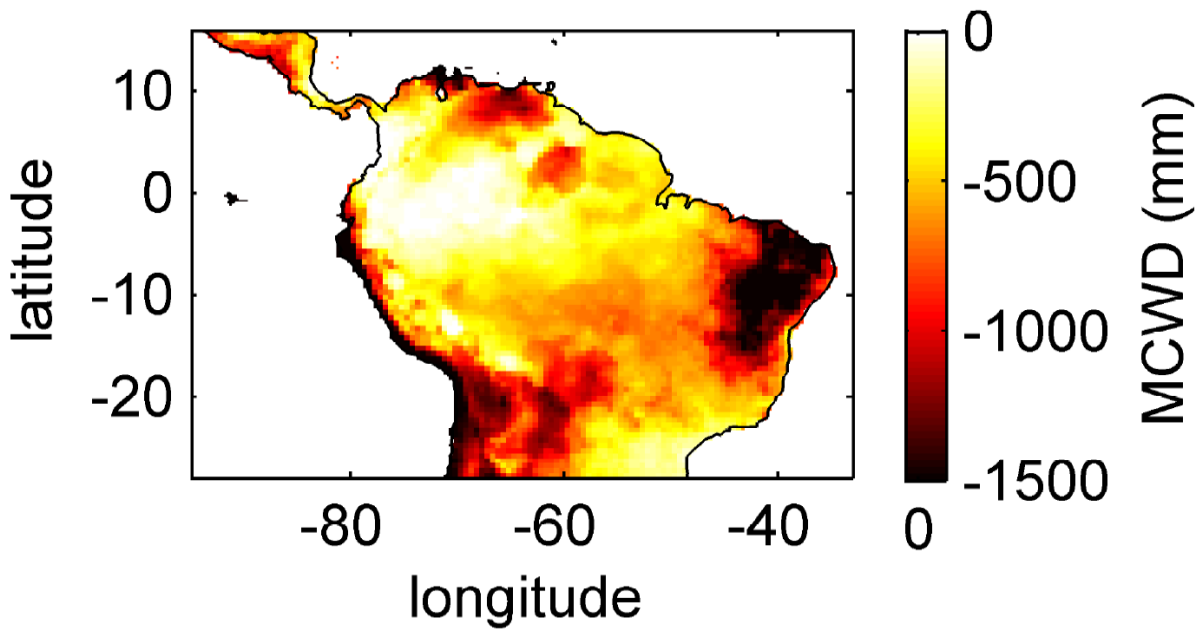
1341 Simulating diverse tree rooting strategies in connection with investment into coarse root structures in LPJmL4.0-VR allows
1342 analysing carbon investment into the newly implemented root carbon pools (Appendix A Sect. 1.4 & Sect. 2.2). As expected,
1343 belowground biomass (BGB; Fig. B9) follows the simulated pattern $\overline{D_{95}}$ (Fig. 2). Highest BGB is found at maximum values
1344 of $\overline{D_{95}}$ and vice versa.

1345 It is important to note that LPJmL4.0-VR appears to underestimate BGB compared to empirical findings in the Amazon
1346 region. While LPJmL4.0-VR shows BGB making up a range of 3.6-16.2% of total biomass across the Amazon region,
1347 different site specific empirical studies found mean values at the upper end or significantly exceeding this range (Fearnside,
1348 2016). The most plausible explanation for underestimating BGB is that LPJmL4.0-VR does not account for root structures
1349 needed for tree statics. Acknowledging tree statics would increase below ground carbon investment and therefore BGB.
1350 Nevertheless, below-ground carbon investment for tree statics would apply for all sub-PFTs simultaneously and would
1351 therefore most likely not significantly change competition dynamics and resulting distributions of tree rooting strategies
1352 found in this study.

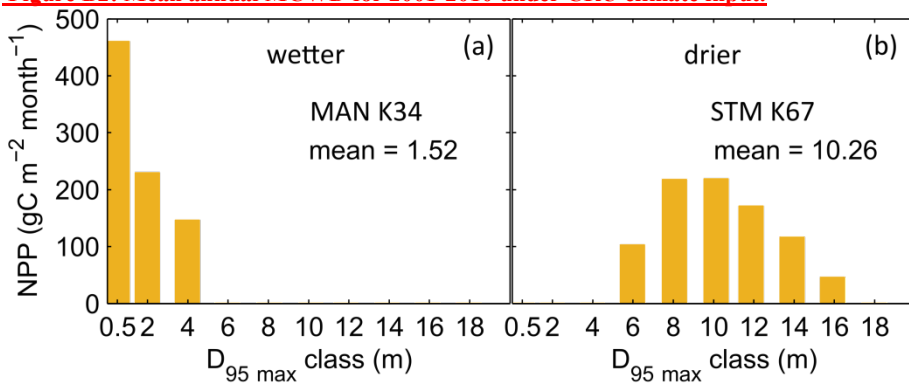
1353 1.3 Figures



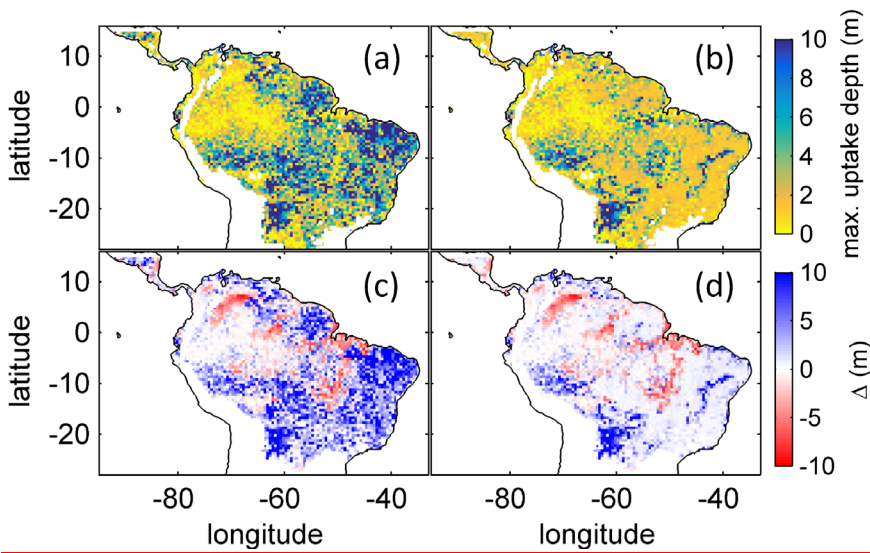
1355
1356 **Figure B1: Mean annual precipitation for 2001-2010 under CRU climate input.**



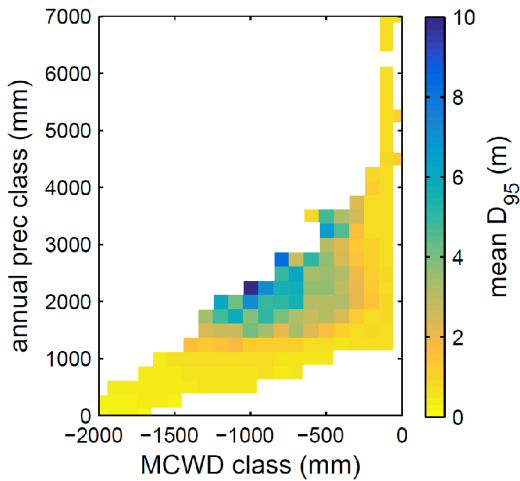
1357
1358 **Figure B2: Mean annual MCWD for 2001-2010 under CRU climate input.**



1359
1360 **Figure B3: Distributions of simulated mean monthly NPP for each D_{95_max} -class for 2001-2010 under CRU climate input at two**
1361 **FluxNet sites. a) Site MAN K34 near the city of Manaus. b) Site STM K67 near the city of Santarem. For more site information see**
1362 **Table A3 and Fig. B6a. At the Fluxnet site MAN K34 (a), which exhibits a mean annual precipitation (MAP) of 2609 mm and a**
1363 **mean MCWD of -222 mm under CRU climate input (2001-2010), the sub-PFT with a maximum rooting depth (D_{95_max}) of 0.5 m**
1364 **contributes most to overall NPP and the whole distribution of NPP weighted D_{95_max} classes shows a mean of 1.52 m. At the**
1365 **Fluxnet site STM K67 (b), which exhibits a lower MAP of 2144 mm and a stronger dry season reflected in a mean MCWD of -465**
1366 **mm, the NPP weighted distribution of D_{95_max} shows a peak at 10 m and a corresponding mean of 10.26 m. Since both sites have**
1367 **a soil depth of 20 m (according to the soil depth input; Sect. 2.3.2, Fig. A3) differences in rooting strategy compositions must**
1368 **emerge from the climatic differences of those sites. It is important to note that D_{95_max} values (i.e. the bins on the x-axes) do not**
1369 **necessarily reflect the true achieved rooting depth of each sub-PFT, but their maximum value. For reasons of visual clarity for this**
1370 **figure we kept the bins of the x-axes as chosen in Table A2.**
1371



1372
 1373 **Figure B4: Comparison of simulated $\overline{D_{95}}$ to product of maximum tree root water uptake depth (MDRU). a) Original (Fan et al.,**
 1374 **2017) MDRU regridded to $0.5^\circ \times 0.5^\circ$ resolution of LPJmL4.0-VR. b) Same as a) but adjusted to soil depth input used in this study**
 1375 **(see 2.3.2), in cases where values of (Fan et al., 2017) exceeded this soil depth. The color scale maximum for a) and b) is set to 10 m.**
 1376 **c) Difference between a) and $\overline{D_{95}}$ simulated with LPJmL4.0-VR under CRU climate forcing (Fig. 2a). d) Difference between b)**
 1377 **and $\overline{D_{95}}$ simulated with LPJmL4.0-VR under CRU climate forcing (Fig. 2a). Red/blue colors denote higher/lower rooting depths**
 1378 **in LPJmL4.0-VR.**



1379
 1380 **Figure B5: Mean rooting depth depicted as mean $\overline{D_{95}}$ over classes of MCWD and annual precipitation sums. Class step size for**
 1381 **precipitation was set to 250 mm and class size for MCWD was set to 50 mm. Regions with high amounts of annual rainfall and**
 1382 **lower seasonality exclusively favour shallow rooted forests (low $\overline{D_{95}}$). $\overline{D_{95}}$ increases with decreasing MCWD (increasing seasonal**
 1383 **drought stress) and decreasing sums of annual precipitation. Below 1200 mm of annual rainfall or -1100 mm of MCWD $\overline{D_{95}}$**
 1384 **sharply decreases again. Note this figure does not consider soil depth. The color scale maximum is set to 10 m.**

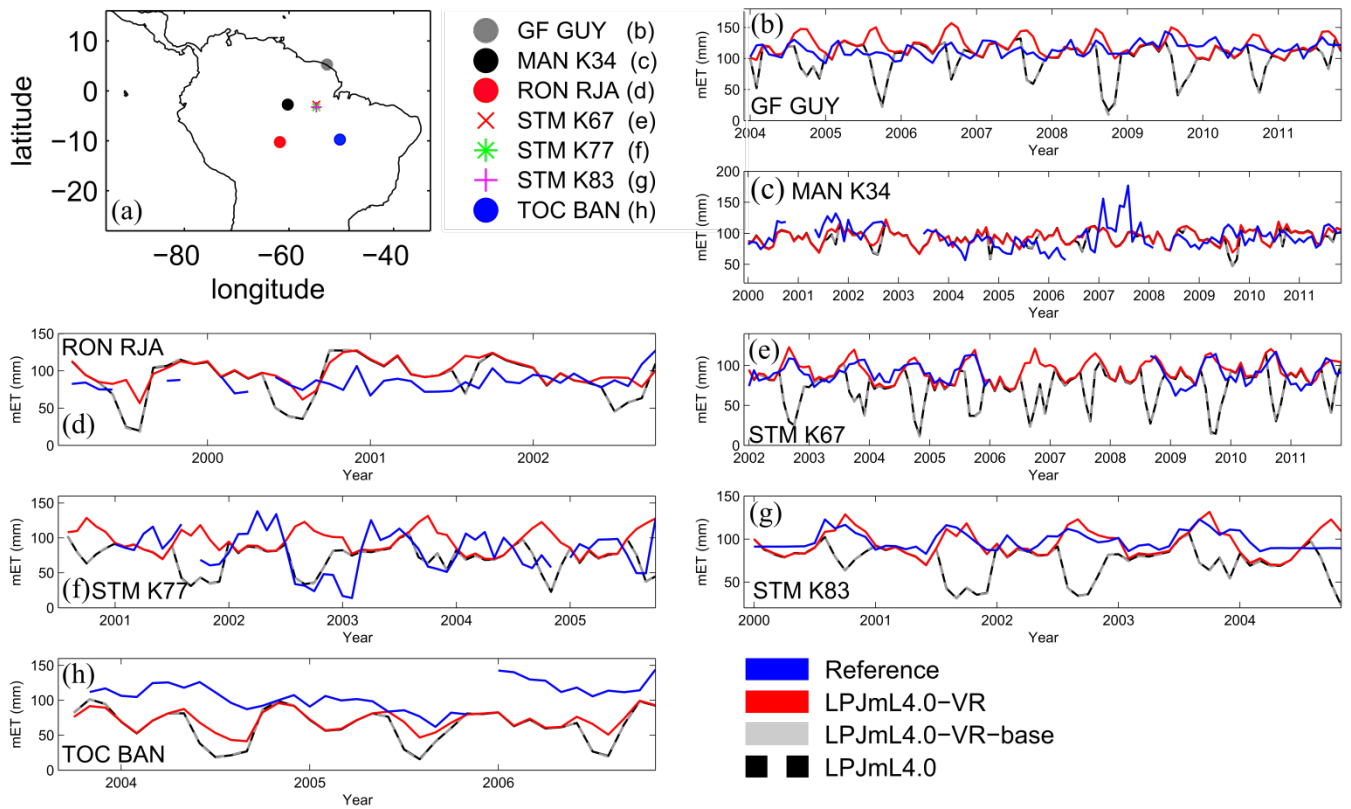


Figure B6: Comparisons of monthly ET between different Fluxnet sites (“Reference”; see also Sect. 2.5.1) and respective simulation output of the different LPJmL model versions used in this study forced with CRU climate. a) Geographical location of different Fluxnet sites (see also Table A3). For statistical measures of the individual comparison see Table B1.

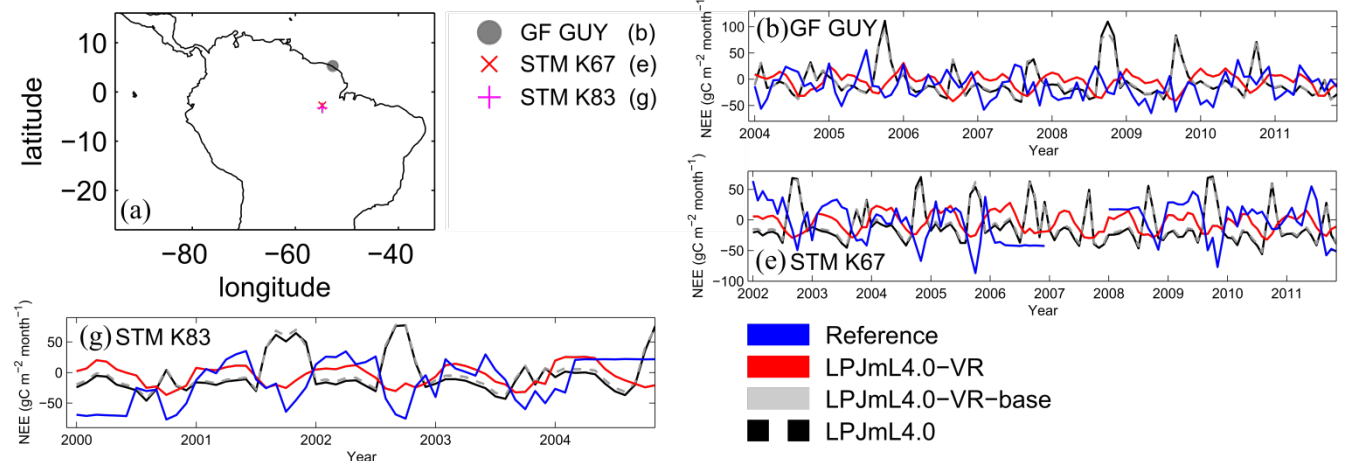
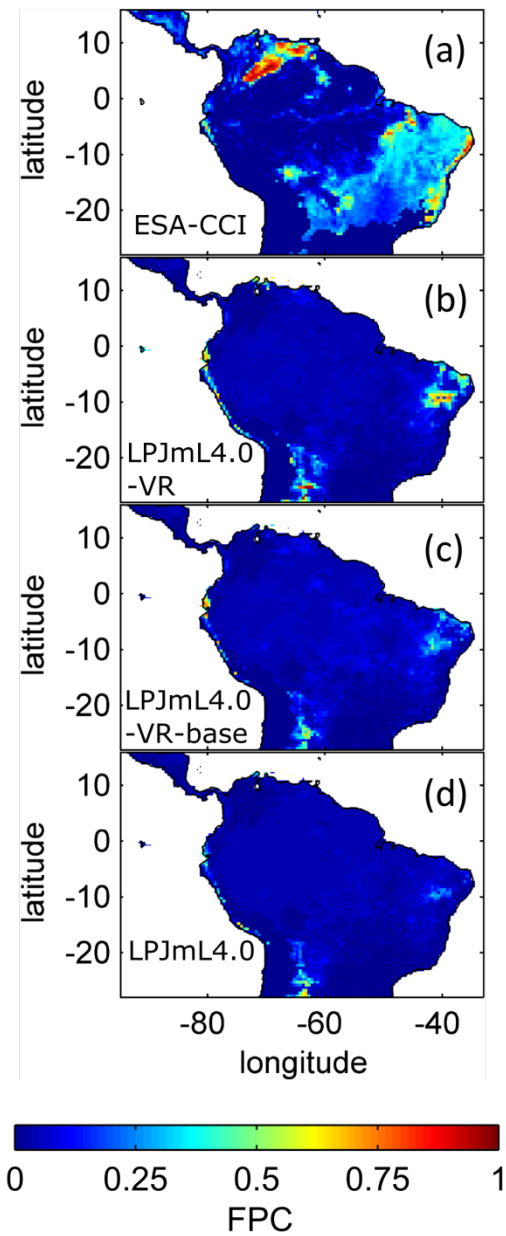
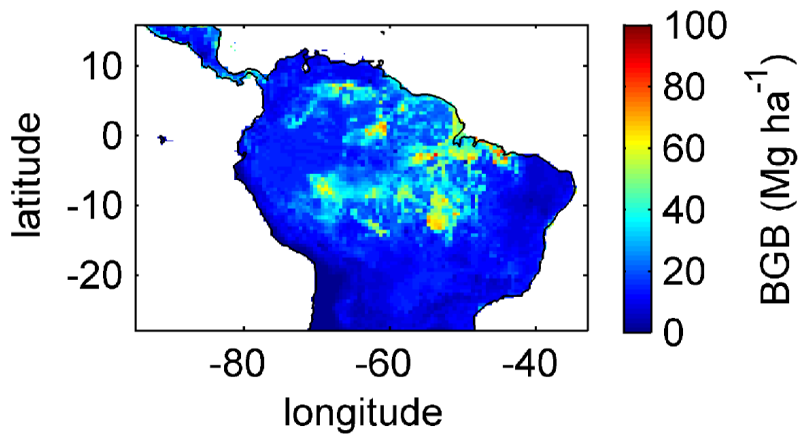


Figure B7: Comparisons of monthly NEE between different Fluxnet sites (“Reference”; see also Sect. 2.5.1) and respective simulation output of the different LPJmL model versions used in this study forced with CRU climate. a) Geographical location of different Fluxnet sites (see also Table A3). For statistical measures of the individual comparison see Table B2. Note due to data scarcity only 3 Fluxnet sites are shown. Plots of all sites are shown in Fig. B12. We kept panel labelling as in Fig. B6 to ensure easy comparability.



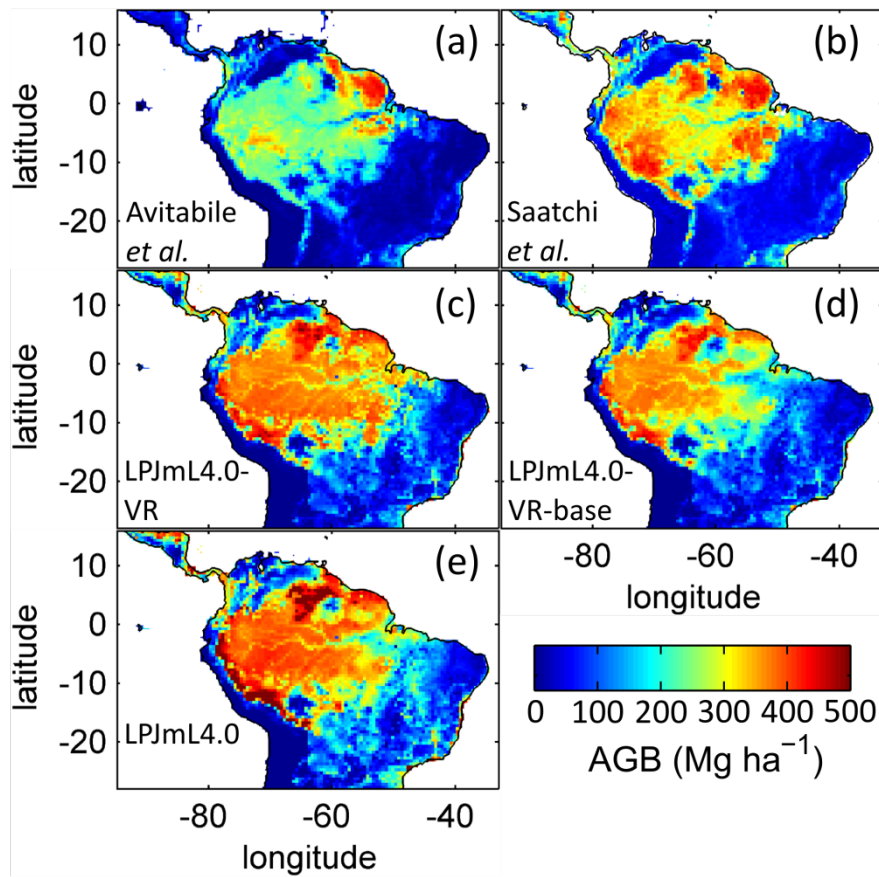
1395
1396
1397
1398
1399

Figure B8: Foliage projected cover (FPC) of the tropical herbaceous PFT over the study region. a) Satellite-derived vegetation composition from ESA Land cover CCI V2.0.7 (Li et al., 2018) reclassified to the PFTs of LPJmL as in (Forkel et al., 2014). b) LPJmL4.0-VR. c) LPJmL4.0-VR-base. d) LPJmL4.0. All LPJmL model versions were forced with CRU climate input. The shown FPC for all models refers to 2001-2010.



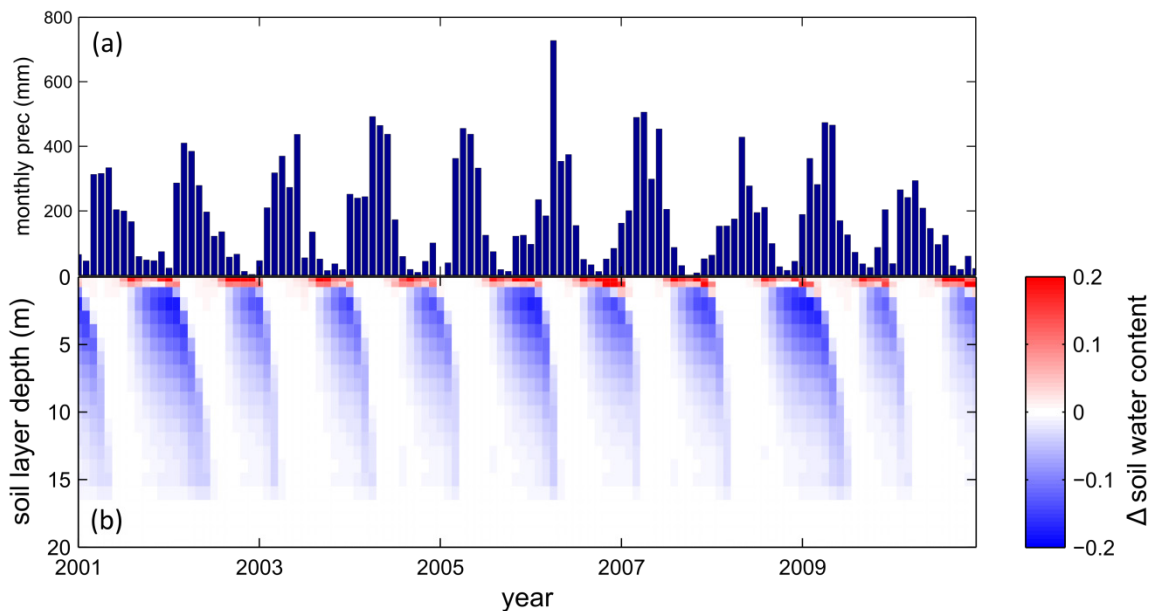
1400
1401
1402

Fig. B9: Mean sum (2001-2010) of belowground biomass (BGB; sum of tree coarse and fine roots) of evergreen and deciduous tree PFTs simulated with LPJmL4.0-VR under CRU climate forcing.



1403
1404
1405
1406
1407
1408

Fig. B10: Comparison of simulated AGB and satellite derived AGB validation products regrided to the spatial resolution of LPJmL models. a) Biomass validation product from Avitabile et al. (2016b). b) AGB validation product from Saatchi et al., (2011). c-e) Mean AGB simulated for the time span 2001-2010 with c) LPJmL4.0-VR. d) LPJmL4.0-VR-base and e) LPJmL4.0. For statistical measures of individual comparisons between model versions (c-e) and satellite derived AGB evaluation products (a-b) see Table A7.



1409
1410
1411
1412
1413
1414

Figure B11: Difference in soil water reaction to seasonal precipitation between LPJmL4.0-VR-base and LPJmL4.0-VR at Fluxnet site STM KM67 a) Mean monthly precipitation input from CRU for 2001-2010. b) Difference in monthly relative soil water content between LPJmL4.0-VR-base and LPJmL4.0-VR forced with CRU climate for 2001-2010. The underlying model output variable “soil water content” of each model version is a number between 0 and 1 depicting the relative water saturation of the soil. Blue colors denote lower soil water content in LPJmL4.0-VR and red colors a lower soil water content in LPJmL4.0-VR-base.

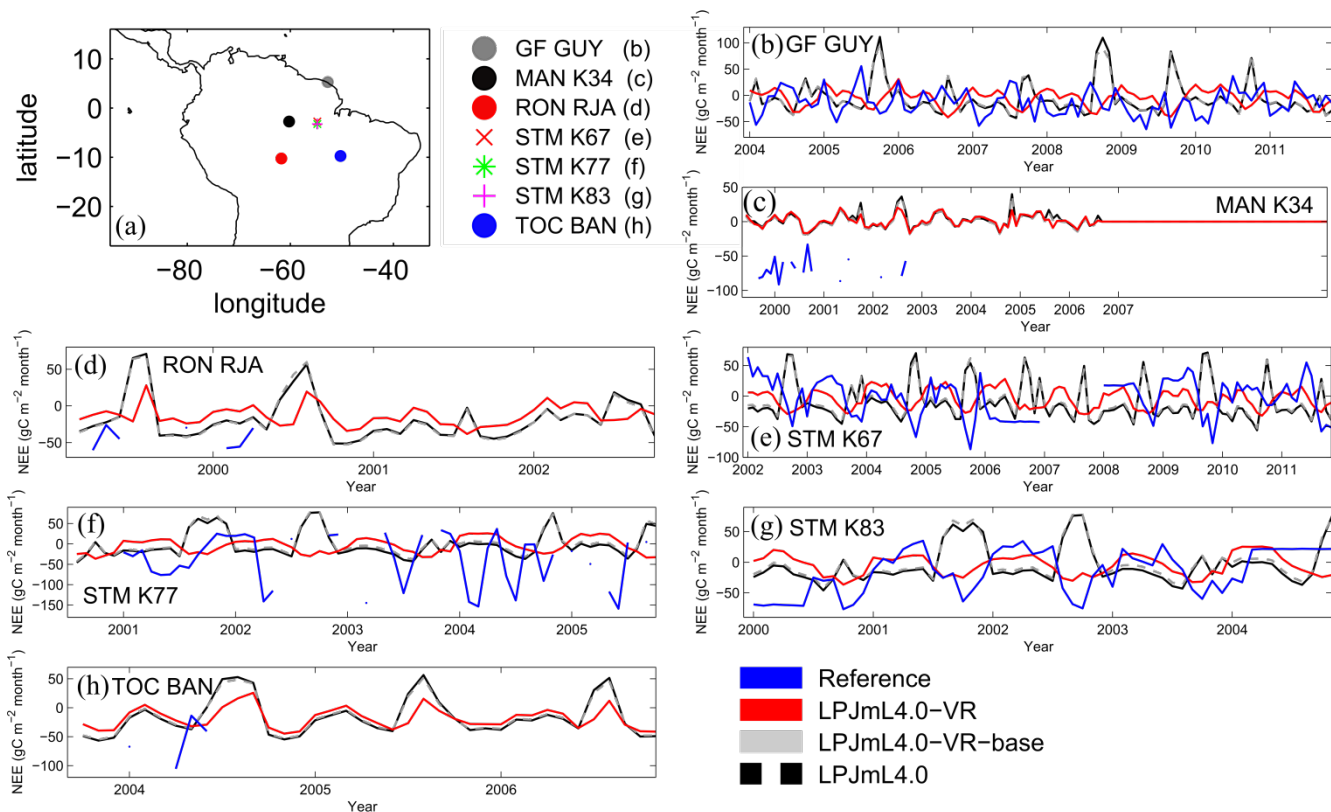


Fig. B12: Comparisons of monthly NEE between different Fluxnet sites (“Reference”; see also Sect. 2.5.1) and respective simulation output of the different LPJmL model versions used in this study forced with CRU climate. a) Geographical location of different Fluxnet sites (see also Table A2).

1.4 Tables

Table B1: Normalized mean error (NME), coefficient of determination (r^2) and p-value of F-statistic piecewise calculated for simulated ET of the different LPJmL model versions used in this study forced with CRU climate input and Fluxnet data of ET at 7 Fluxnet sites (in accordance with Fig. B6).

| Statistic | Model | TOC BAN | MAN_K34 | STM_K67 | STM_K77 | STM_K83 | RON_RJA | GF_GUY |
|-----------|------------------|---------|---------|---------|---------|---------|---------|--------|
| NME | LPJmL4.0-VR | 2.41 | 1.11 | 0.75 | 1.38 | 1.10 | 2.28 | 1.57 |
| | LPJmL4.0-VR-base | 2.92 | 1.22 | 2.29 | 0.98 | 2.74 | 2.73 | 2.38 |
| | LPJmL4.0 | 2.93 | 1.23 | 2.27 | 0.98 | 2.74 | 2.70 | 2.36 |
| r^2 | LPJmL4.0-VR | 0.09 | 0.03 | 0.53 | 0.17 | 0.43 | 0.01 | 0.08 |
| | LPJmL4.0-VR-base | 0.10 | 0.00 | 0.33 | 0.14 | 0.03 | 0.01 | 0.01 |
| | LPJmL4.0 | 0.09 | 0.00 | 0.33 | 0.14 | 0.03 | 0.01 | 0.01 |
| p-value | LPJmL4.0-VR | 0.075 | 0.041 | < 0.001 | 0.002 | < 0.001 | 0.575 | 0.005 |
| | LPJmL4.0-VR-base | 0.067 | 0.585 | < 0.001 | 0.005 | 0.221 | 0.517 | 0.277 |
| | LPJmL4.0 | 0.068 | 0.672 | < 0.001 | 0.005 | 0.221 | 0.514 | 0.274 |

Table B2: Normalized mean error (NME), coefficient of determination (r^2) and p-value of F-statistic piecewise calculated for simulated NEE of the different LPJmL model versions used in this study forced with CRU climate input and Fluxnet data of NEE at 3 Fluxnet sites (in accordance with Fig. B7).

| Statistic | Model | STM_K67 | STM_K83 | GF_GUY |
|-----------|------------------|---------|---------|--------|
| NME | LPJmL4.0-VR | 0.90 | 0.84 | 1.30 |
| | LPJmL4.0-VR-base | 1.62 | 1.36 | 1.52 |
| | LPJmL4.0 | 1.68 | 1.39 | 1.52 |
| r^2 | LPJmL4.0-VR | 0.16 | 0.14 | 0.00 |
| | LPJmL4.0-VR-base | 0.32 | 0.06 | 0.03 |
| | LPJmL4.0 | 0.33 | 0.07 | 0.03 |
| p-value | LPJmL4.0-VR | < 0.001 | 0.003 | 0.515 |
| | LPJmL4.0-VR-base | < 0.001 | 0.055 | 0.046 |
| | LPJmL4.0 | < 0.001 | 0.047 | 0.059 |

1427
1428
1429
1430
1431
1432

Table B3: Normalized mean error (NME), coefficient of determination (r^2) and p-value of F-statistic piecewise calculated for the simulated ET of the different LPJmL model versions used in this study and continental scale gridded ET products within 5 regional climatological clusters. With respect to Fig. 3 comparisons are based on the monthly mean of corridors shown, i.e. 1) the monthly mean of all outputs produced by one LPJmL model version but forced with different climate inputs and 2) the monthly mean of all continental scale gridded ET data products.

| Statistic | Model | NSA | EQ W | EQ E | SAmz | SAMS |
|-----------|------------------|---------|---------|---------|---------|---------|
| NME | LPJmL4.0-VR | 0.08 | 0.26 | 0.62 | 0.20 | 0.06 |
| | LPJmL4.0-VR-base | 0.37 | 0.42 | 1.95 | 0.58 | 0.13 |
| | LPJmL4.0 | 0.34 | 0.26 | 1.92 | 0.58 | 0.11 |
| r^2 | LPJmL4.0-VR | 0.98 | 0.94 | 0.91 | 0.98 | 1.00 |
| | LPJmL4.0-VR-base | 0.94 | 0.96 | 0.20 | 0.91 | 0.99 |
| | LPJmL4.0 | 0.93 | 0.96 | 0.21 | 0.90 | 0.99 |
| p-value | LPJmL4.0-VR | < 0.001 | < 0.001 | < 0.001 | < 0.001 | < 0.001 |
| | LPJmL4.0-VR-base | < 0.001 | < 0.001 | 0.143 | < 0.001 | < 0.001 |
| | LPJmL4.0 | < 0.001 | < 0.001 | 0.135 | < 0.001 | < 0.001 |

1433
1434
1435
1436

Table B4: Normalized mean error (NME) of FPC comparison piecewise calculated between 1) the satellite-derived vegetation composition from ESA Land cover CCI V2.0.7 (Li et al., 2018) reclassified to the PFTs of LPJmL as in Forkel et al. (2014) and 2) all LPJmL model versions used in this study forced with CRU climate data (in accordance with Fig. 4).

| Statistic | Model | FPC Evergreen | FPC Deciduous |
|-----------|------------------|---------------|---------------|
| NME | LPJmL4.0-VR | 0.31 | 1.01 |
| | LPJmL4.0-VR-base | 0.38 | 1.5 |
| | LPJmL4.0 | 0.47 | 1.76 |

1437

1438
1439
1440

Table B5: Normalized mean error (NME) of AGB comparison piecewise calculated between 1) the satellite-derived AGB validation products and 2) all LPJmL model versions used in this study forced with CRU climate data (in accordance with Fig. B10).

| Statistic | Model | Avitabile et al. | Saatchi et al. |
|-----------|------------------|------------------|----------------|
| NME | LPJmL4.0-VR | 0.78 | 0.12 |
| | LPJmL4.0-VR-base | 0.69 | 0.11 |
| | LPJmL4.0 | 1.09 | 0.14 |

1441